

Evolutionary Algorithms Applied to Antennas and Propagation: Emerging Trends and Applications 2017

Special Issue Editor in Chief: Sotirios K. Goudos

Guest Editors: Dimitris E. Anagnostou, Christos Kalialakis, and Symeon Nikolaou





**Evolutionary Algorithms Applied to
Antennas and Propagation: Emerging
Trends and Applications 2017**

International Journal of Antennas and Propagation

**Evolutionary Algorithms Applied to
Antennas and Propagation: Emerging
Trends and Applications 2017**

Special Issue Editor in Chief: Sotirios K. Goudos

Guest Editors: Dimitris E. Anagnostou, Christos Kalialakis,
and Symeon Nikolaou



Copyright © 2018 Hindawi. All rights reserved.

This is a special issue published in “International Journal of Antennas and Propagation.” All articles are open access articles distributed under the Creative Commons Attribution License, which permits unrestricted use, distribution, and reproduction in any medium, provided the original work is properly cited.

Editorial Board

Ana Alejos, Spain
Mohammad Ali, USA
Jaume Anguera, Spain
Rodolfo Araneo, Italy
Alexei Ashikhmin, USA
Herve Aubert, France
Paolo Baccarelli, Italy
Xiulong Bao, Ireland
Toni Björninen, Finland
Stefania Bonafoni, Italy
Paolo Burghignoli, Italy
Shah Nawaz Burokur, France
Giuseppe Castaldi, Italy
Luca Catarinucci, Italy
Felipe Catedra, Spain
Marta Cavagnaro, Italy
Shih Yuan Chen, Taiwan
Yu Jian Cheng, China
Renato Cicchetti, Italy
Riccardo Colella, Italy
Laura Corchia, Italy
Lorenzo Crocco, Italy
Claudio Curcio, Italy
Francesco D'Agostino, Italy
María Elena de Cos Gómez, Spain
Tayeb A. Denidni, Canada
Giuseppe Di Massa, Italy

Michele D'Urso, Italy
Francisco Falcone, Spain
Miguel Ferrando Bataller, Spain
Flaminio Ferrara, Italy
Vincenzo Galdi, Italy
Claudio Gennarelli, Italy
Farid Ghanem, Algeria
Sotirios K. Goudos, Greece
Rocco Guerriero, Italy
Kerim Guney, Turkey
Song Guo, Japan
Tamer S. Ibrahim, USA
M. Ramlee Kamarudin, UK
Slawomir Koziel, Iceland
Luis Landesa, Spain
Ding-Bing Lin, Taiwan
Angelo Liseno, Italy
Pierfrancesco Lombardo, Italy
Lorenzo Luini, Italy
Atsushi Mase, Japan
Diego Masotti, Italy
Ch. F. Mecklenbräuker, Austria
Ahmed Toaha Mobashsher, Australia
Ananda S. Mohan, Australia
J.-M. Molina-Garcia-Pardo, Spain
Giuseppina Monti, Italy
Giorgio Montisci, Italy

Andrea Francesco Morabito, Italy
N. Nasimuddin, Singapore
Mourad Nedil, Canada
Symeon Nikolaou, Cyprus
Giacomo Oliveri, Italy
Mauro Parise, Italy
Ikmo Park, Republic of Korea
Josep Parrón, Spain
Matteo Pastorino, Italy
Xianming Qing, Singapore
Ahmad Safaai-Jazi, USA
Safieddin Safavi-Naeini, Canada
Magdalena Salazar-Palma, Spain
Stefano Selleri, Italy
Raffaele Solimene, Italy
Gino Sorbello, Italy
Seong-Youp Suh, USA
Sheng Sun, Hong Kong
Larbi Talbi, Canada
Luciano Tarricone, Italy
Parveen Wahid, USA
Chien-Jen Wang, Taiwan
Wen-Qin Wang, China
Mustapha C E Yagoub, Canada
Shiwen Yang, China
Yuan Yao, China

Contents

Evolutionary Algorithms Applied to Antennas and Propagation: Emerging Trends and Applications 2017

Sotirios K. Goudos , Dimitris E. Anagnostou, Christos Kalialakis , and Symeon Nikolaou 
Editorial (2 pages), Article ID 2945405, Volume 2018 (2018)

Hybrid Robust Optimization for the Design of a Smartphone Metal Frame Antenna

Sungwoo Lee, Jong Min Lee, Keum Cheol Hwang , Sanguk Park, and Soonyong Lee
Research Article (8 pages), Article ID 6325806, Volume 2018 (2018)

An Antenna Array Sidelobe Level Reduction Approach through Invasive Weed Optimization

Geng Sun , Yanheng Liu, Han Li, Shuang Liang, Aimin Wang , and Boyu Li
Research Article (16 pages), Article ID 4867851, Volume 2018 (2018)

Combination of the Improved Diffraction Nonlocal Boundary Condition and Three-Dimensional Wide-Angle Parabolic Equation Decomposition Model for Predicting Radio Wave Propagation

Ruidong Wang, Guizhen Lu, Rongshu Zhang, and Weizhang Xu
Research Article (10 pages), Article ID 2728380, Volume 2017 (2018)

Application of Genetic Algorithm to Estimation of Function Parameters in Lightning Currents Approximations

V. Javor, K. Lundengård, M. Rančić, and S. Silvestrov
Research Article (11 pages), Article ID 4937943, Volume 2017 (2018)

Design, Simulation, and Optimization of an Irregularly Shaped Microstrip Patch Antenna for Air-to-Ground Communications

L. A. R. Ramirez and J. C. A. Santos
Research Article (9 pages), Article ID 5156263, Volume 2017 (2018)

Editorial

Evolutionary Algorithms Applied to Antennas and Propagation: Emerging Trends and Applications 2017

Sotirios K. Goudos ¹, **Dimitris E. Anagnostou**,² **Christos Kalialakis** ³,
and Symeon Nikolaou ⁴

¹*Department of Physics, Radiocommunications Laboratory, Aristotle University of Thessaloniki, 54124 Thessaloniki, Greece*

²*Institute of Sensors, Signals and Systems, Heriot-Watt University, Edinburgh EH14 4AS, UK*

³*Centre Tecnològic de Telecomunicacions de Catalunya (CTTC/CERCA), Barcelona, Spain*

⁴*Frederick University, Nicosia, Cyprus*

Correspondence should be addressed to Sotirios K. Goudos; sgoudo@physics.auth.gr

Received 28 January 2018; Accepted 28 January 2018; Published 19 April 2018

Copyright © 2018 Sotirios K. Goudos et al. This is an open access article distributed under the Creative Commons Attribution License, which permits unrestricted use, distribution, and reproduction in any medium, provided the original work is properly cited.

This is the second special issue [1] devoted to evolutionary algorithms (EAs) applied to antennas and propagation problems.

A multitude of evolutionary algorithms (EAs) have been developed over the last years that imitate the evolution of biological entities. EAs are applied for the numerical solution of optimization problems with single and multiple objectives. Of particular interest here is EAs that have been adapted to solve problems related to design of antennas and propagation of electromagnetic waves in challenging environments. These techniques, among others, include genetic algorithms (GAs), evolution strategies (ES), particle swarm optimization (PSO), differential evolution (DE), and ant colony optimization (ACO). EAs combined in various instances with numerical methods in electromagnetics have increased their impact on antenna design and propagation problems. Moreover, hybrid combinations of EAs with other algorithms inspired by physics or chemistry are also emerging.

The papers of the special issue demonstrate a continuous interest for application of new EAs to an ever increasing range of problems in the antennas and propagation areas.

The special issue consists of five research papers, two for propagation and three for antenna problems. The algorithms used by the authors are genetic algorithms (two papers), swarm optimization (one paper), invasive weed optimization

(one paper), and a hybrid technique (one paper). Below, a short description of the papers is given.

R. Wang et al. present a hybrid method suitable for the predictions of radio wave propagation in small areas found in urban environments in the paper “Combination of the Improved Diffraction Nonlocal Boundary Condition and Three-Dimensional Wide-Angle Parabolic Equation Decomposition Model for Predicting Radio Wave Propagation”. The method enhances the finite-difference parabolic equation by introducing the recursive convolution with vector fitting to improve the computation speed. The new method, termed WA-3DPE, is also verified by measurement results.

L. A. R. Ramirez and J. C. A. dos Santos in the paper “Design, Simulation, and Optimization of an Irregularly Shaped Microstrip Patch Antenna for Air-to-Ground Communications” combine the finite difference time-domain method (FDTD) in conjunction with a genetic algorithm (GA). The hybrid technique is used to design an efficient patch antenna at 14.25 GHz with 35 dB return loss with a 10 dB bandwidth of 3.7 GHz.

The application of a generic algorithm (GA) to lightnings is given by V. Javor et al. In the paper “Application of Genetic Algorithm to Estimation of Function Parameters in Lightning Currents Approximations,” the genetic algorithm is applied for the estimation of the parameters of two-peaked

analytically extended function (2P-AEF) which are used for approximation of measured and typical lightning discharge currents. Good agreement with experimentally measured waveshapes is achieved.

S. Lee et al. present a method that is based on a genetical swarm optimization (GSO) which is combined with an orthogonal array (OA). Their paper “Hybrid Robust Optimization for the Design of a Smartphone Metal Frame Antenna” presents an inverted-F antenna design implemented in a metal frame. The antenna design is robust to the tolerances resulting from the fabrication process by over 60%, compared to that of a conventional antenna.

G. Sun et al. apply the invasive weed optimization (IWO) algorithm in the classic problem of maximum sidelobe level (SLL). The paper “An Antenna Array Sidelobe Level Reduction Approach through Invasive Weed Optimization” addresses both the linear antenna array and the circular antenna arrays. The IWO algorithm for this problem is compared favourably with other EAs such as the cuckoo search, firefly algorithm, and biogeography-based optimization.

Acknowledgments

We would like to thank the authors who submitted their work for consideration to this special issue as well as the reviewers for their efforts and constructive criticism.

*Sotirios K. Goudos
Dimitris E. Anagnostou
Christos Kalialakis
Symeon Nikolaou*

References

- [1] S. K. Goudos, D. E. Anagnostou, C. Kalialakis, P. Vasant, and S. Nikolaou, “Evolutionary algorithms applied to antennas and propagation: emerging trends and applications,” *International Journal of Antennas and Propagation*, vol. 2016, Article ID 5279647, 2 pages, 2016.

Research Article

Hybrid Robust Optimization for the Design of a Smartphone Metal Frame Antenna

Sungwoo Lee,¹ Jong Min Lee,¹ Keum Cheol Hwang ,¹ Sanguk Park,² and Soonyong Lee²

¹*School of Electronic and Electrical Engineering, Sungkyunkwan University, Suwon 440-746, Republic of Korea*

²*Global Technology Center, Samsung Electronics Co. Ltd., Suwon, Republic of Korea*

Correspondence should be addressed to Keum Cheol Hwang; khwang@skku.edu

Received 3 August 2017; Revised 27 November 2017; Accepted 26 December 2017; Published 18 February 2018

Academic Editor: Sotirios K. Goudos

Copyright © 2018 Sungwoo Lee et al. This is an open access article distributed under the Creative Commons Attribution License, which permits unrestricted use, distribution, and reproduction in any medium, provided the original work is properly cited.

Hybrid robust optimization that combines a genetical swarm optimization (GSO) scheme with an orthogonal array (OA) is proposed to design an antenna robust to the tolerances arising during the fabrication process of the antenna in this paper. An inverted-F antenna with a metal frame serves as an example to explain the procedure of the proposed method. GSO is adapted to determine the design variables of the antenna, which operates on the GSM850 band (824–894 MHz). The robustness of the antenna is evaluated through a noise test using the OA. The robustness of the optimized antenna is improved by approximately 61.3% relative to that of a conventional antenna. Conventional and optimized antennas are fabricated and measured to validate the experimental results.

1. Introduction

Recently, as the interest in smartphones has increased in the mobile communication market, metal frames are becoming widely used to provide the consumer with a stylish and luxurious exterior for their devices. However, when the metal frame is near the antenna in a smartphone, it causes undesired coupling effects which degrade the antenna performance [1]. The performance can also be deteriorated due to the tolerances arising during the manufacturing process of an antenna. Therefore, noise factors such as tolerance levels should be considered in the design of an antenna. Taguchi's method (TM) is a well-known technique which can be used to find a robustly optimized condition against such noise factors [2]. Moreover, a method which is realized on the basis of an orthogonal array (OA) can dramatically reduce the time required to design the antenna [3]. However, it is very difficult to find a global optimum using only TM because an OA consists of a limited number and limited level sizes of design variables [4]. In order to resolve the drawbacks of TM, hybrid methods have been introduced [5–7]. In one study [5], a hybrid method which combined TM with an evolution strategy (ES) was proposed. The ES is used to

determine the geometry of the antenna, which operates at around 920 MHz. Subsequently, based on the result acquired from the ES, a robust antenna configuration is obtained by TM. TM with a genetic algorithm (GA) or particle swarm optimization (PSO) was also investigated in schemes where robust genes or particles were selected and utilized [6, 7].

In the present paper, a hybrid robust optimization (HRO) which combines genetical swarm optimization (GSO) with an OA is proposed. The standard TM is inefficient when used with an extensive search boundary because it considers only limited cases. To overcome this drawback, the GSO algorithm is used instead of OA to obtain a new combination of design parameters in the proposed method. GSO as used here is developed based on PSO, and randomly chosen parts of the population evolve with a GA during each iteration. Accordingly, GSO is less likely to fall to the local optimum and its convergence speed is also faster than those of the GA and PSO methods [8]. Besides, the total number of experiments is reduced because an OA is used for noise testing. An inverted-F antenna (IFA) with a metal frame [9–11] is employed as an example to explain the procedure of the proposed method. The geometry of the IFA is illustrated in Section 2. The procedure of the HRO is described

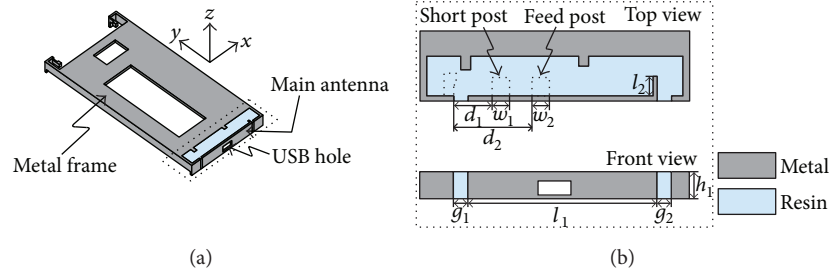


FIGURE 1: The geometry of a smartphone body and main antenna: (a) 3D view of the smartphone body and (b) expanded view of the main antenna.

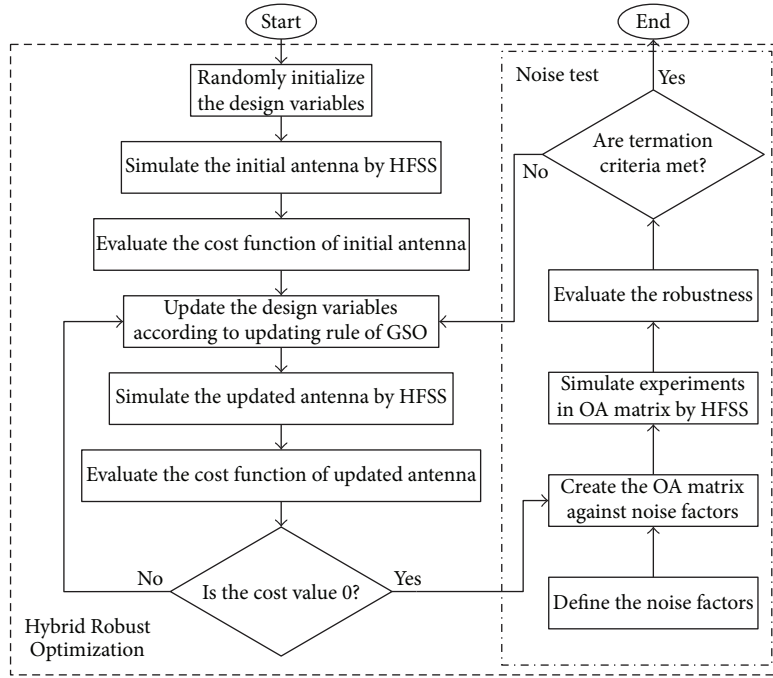


FIGURE 2: Flow chart of the proposed hybrid robust optimization scheme.

in detail in Section 3. The robust optimization result is depicted in Section 4. The experimental results are demonstrated in Section 5.

2. Geometry

In general, the main antenna in a smartphone is positioned at the bottom, as shown in Figure 1(a). Figure 1(b) shows the detailed configuration of the main antenna in this case, which operates as an IFA. The antenna is aligned with the protruding L-shaped and inverted L-shaped metal frame. A rectangular hole in the antenna exists for the universal serial bus connector. g_1 and g_2 denote the left and right gaps between the antenna and the metal frame, respectively. The length of the antenna is defined as l_1 , and that of the tail of the antenna is denoted by l_2 . w_1 and w_2 are widths of the short and feed posts, respectively. The distances from the edge of the protruding L-shaped metal frame to the left edge of the short post and to that of the feed post are correspondingly represented by d_1 and d_2 . h_1 is the height of the antenna. The dimensions of the conventional main antenna are as

TABLE 1: Optimization range of design variables.

	Design variable (mm)								
	g_1	g_2	l_1	l_2	w_1	w_2	d_1	d_2	h_1
Max	0.2	0.2	47.2	0	1.5	1.5	3.7	11.5	6.9
Min	3.5	3.5	49.2	10	3.5	3.5	5.7	13.5	7.9

follows: $g_1 = 1.7$ mm, $g_2 = 1.7$ mm, $l_1 = 48.2$ mm, $l_2 = 2$ mm, $w_1 = 2$ mm, $w_2 = 2$ mm, $d_1 = 4.4$ mm, $d_2 = 13.8$ mm, and $h_1 = 6.9$ mm.

3. Hybrid Robust Optimization

Figure 2 shows a flow chart of the proposed HRO. This method is conducted on the basis of GSO, and the robustness of the antenna is evaluated through the OA matrix. The detailed procedure for the HRO is given below:

- (1) Randomly initialize the design variables within the range given in Table 1.

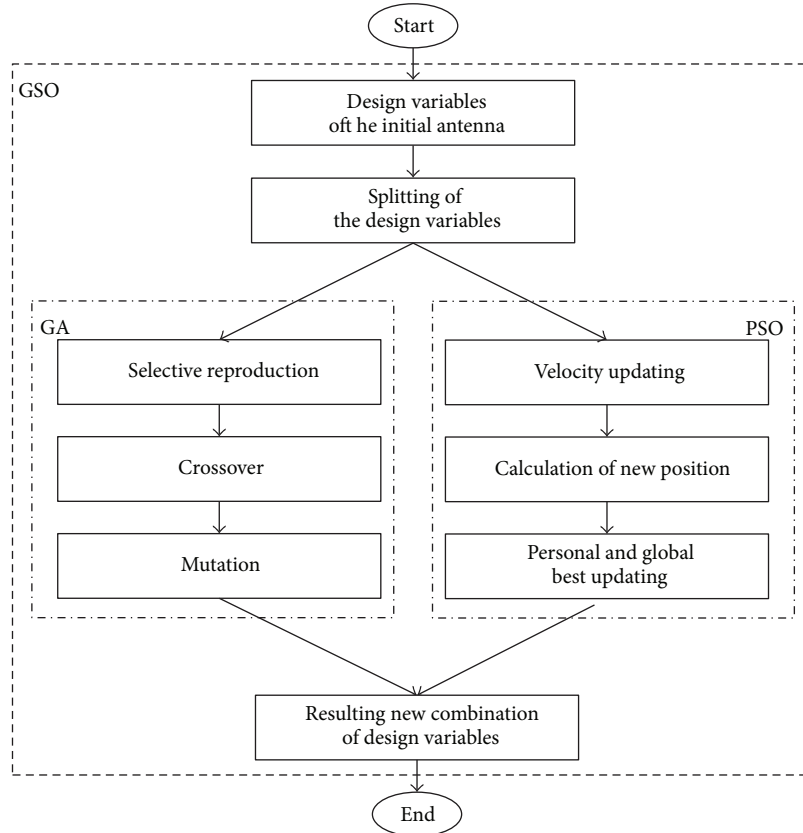


FIGURE 3: Flowchart of the updating rule of GSO.

- (2) Simulate the initial antenna using ANSYS high-frequency structure simulation (HFSS) software, and evaluate the cost function of the antenna. The cost function is defined such that the -6 dB reflection bandwidth of the antenna covers the GSM850 (824–894 MHz) band,

$$\text{cost} = \sum_{i=1}^n F(i), \quad (1)$$

where

$$F(i) = \begin{cases} 1, & \text{if } S_{11}(f_i) > -6 \text{ dB,} \\ 0, & \text{otherwise,} \end{cases} \quad (2)$$

where f_i is i th sampling frequency within the GSM850 band, $S_{11}(f_i)$ is reflection coefficient at each sampling frequency, and n is the number of sampling frequencies. In this paper, n is set to 71.

- (3) Update the design variables according to the updating rule of GSO. Figure 3 shows a flowchart of the updating rule of GSO. In this paper, GSO with a hybridization coefficient of 0.2 is realized. Specifically, 20% of the design variables are optimized by the GA while the others are optimized by the PSO. The optimization performance is usually dependent on the level of the hybridization coefficient. It was found that a hybridization coefficient

of 0.2 is optimum in this optimization problem. An analysis of the performance of the GSO algorithm is available in the literature [8]. The GSO converges more rapidly than the GA or PSO under any search condition.

- (4) Simulate the updated antenna, and evaluate the cost function of the antenna based on (1).
- (5) Steps 3 to 4 are repeated until the cost function is 0.
- (6) Define the noise factors, and create the OA matrix against the noise factors [12]. In this article, the noise factor is defined as the parameter that affects the resonant frequency of the conventional main antenna. Figure 4 shows the simulated resonant frequencies of the conventional antenna while changing the design variables by ± 0.2 mm. The variances of the resonant frequency of the antenna in accordance with the changes in each design variable are listed in Table 2. Among the nine design variables, the four parameters of g_2 , l_1 , l_2 , and h_1 that have resonant frequency variance of 4 MHz or more are used as the noise factors in this paper.
- (7) Create the OA (9, 4, 3, and 0.2) matrix against the noise factors, and implement the experiments in the matrix using HFSS.
- (8) Evaluate the robustness of the antenna as optimized by GSO. The robustness is defined as the variance

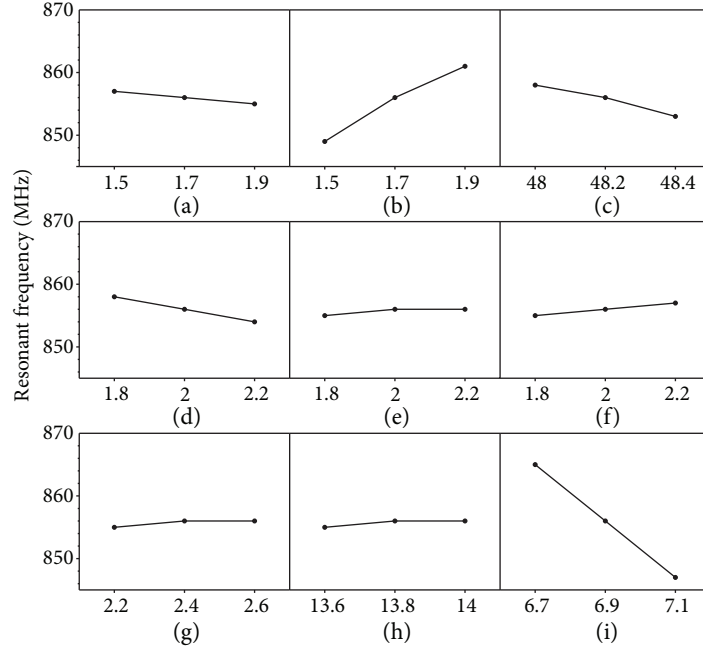


FIGURE 4: Simulated resonant frequencies of the conventional antenna according to the changes in (a) g_1 , (b) g_2 , (c) l_1 , (d) l_2 , (e) w_1 , (f) w_2 , (g) d_1 , (h) d_2 , and (i) h_1 .

TABLE 2: Variance of the resonant frequency of each design variable.

Design variable	Variance
g_1	2 MHz
l_1	5 MHz
w_1	1 MHz
d_1	1 MHz
h_1	18 MHz
g_2	12 MHz
l_2	4 MHz
w_2	2 MHz
d_2	1 MHz

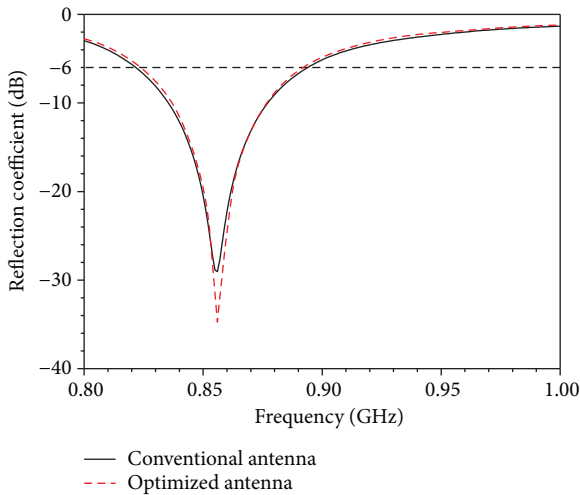


FIGURE 5: Simulated reflection coefficients of the conventional and optimized antennas.

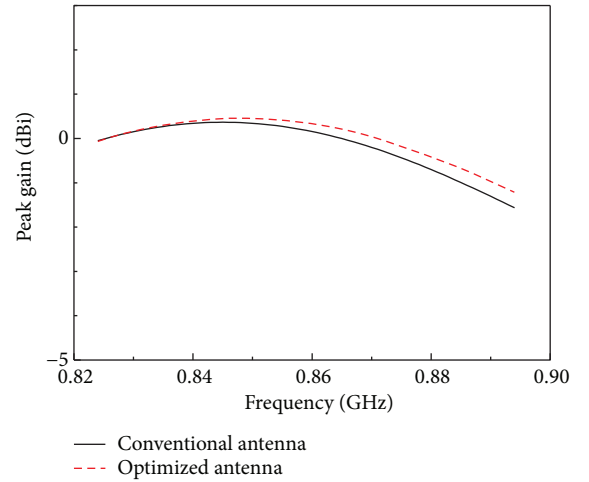


FIGURE 6: Simulated peak gains of the conventional and optimized antennas.

of the resonant frequency obtained from the experiments in the OA matrix:

$$\text{Robustness} = f_r(\text{max}) - f_r(\text{min}), \quad (3)$$

where $f_r(\text{max})$ and $f_r(\text{min})$ are the maximum and minimum resonant frequencies in the experiments, respectively.

- (9) When the robustness meets the termination criteria, the process of the proposed method is terminated. The termination criteria stipulate that the robustness of the optimized main antenna must be improved by more than 50% as compared to that of the conventional antenna.

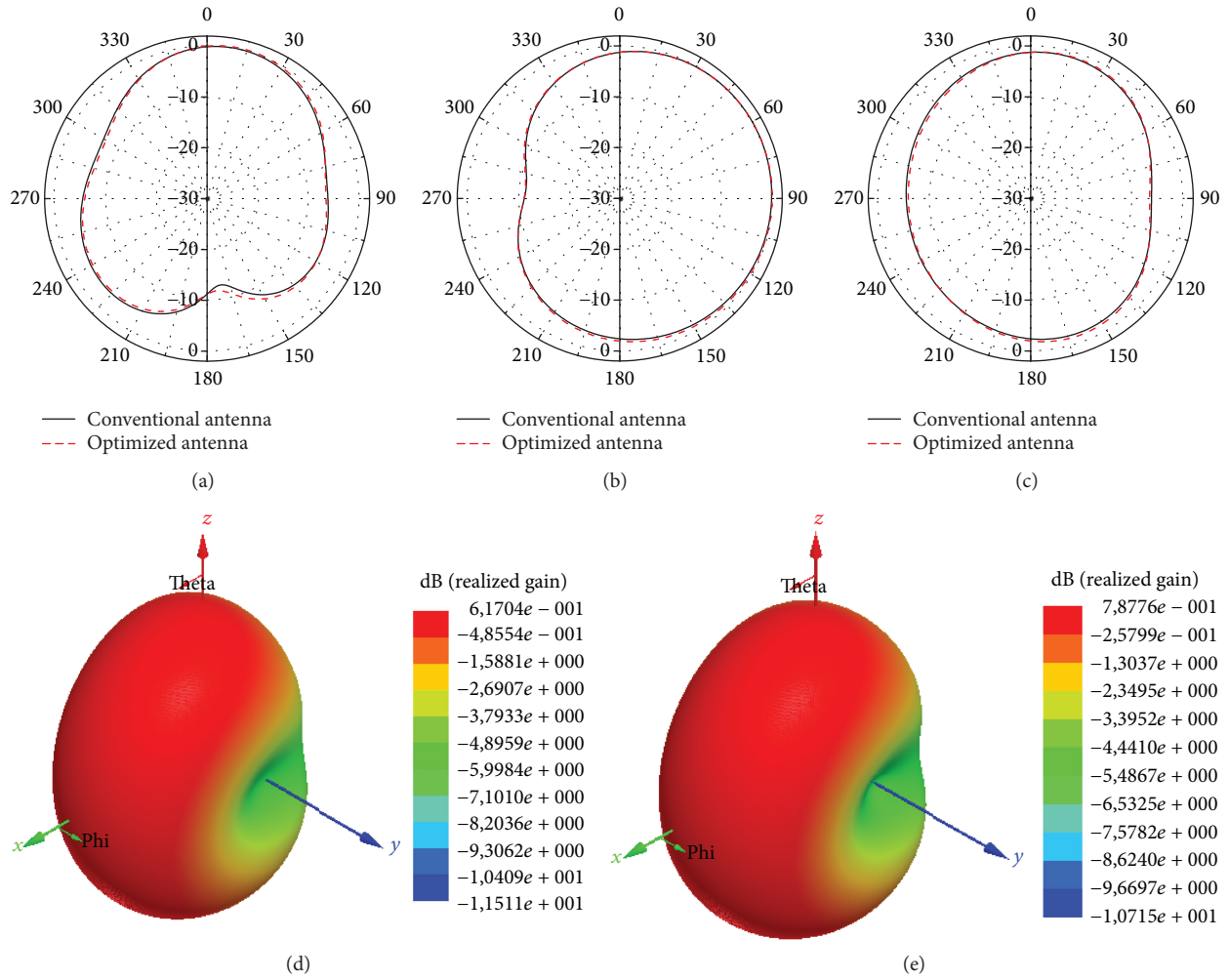


FIGURE 7: Simulated radiation patterns of the conventional and optimized antennas: (a) xy -plane, (b) xz -plane, (c) yz -plane, (d) 3D radiation pattern of the conventional antenna, and (e) 3D radiation pattern of the optimized antenna.

TABLE 3: OA (9, 4, 3, and 0.2) matrix for the conventional antenna.

Experiment	Design variable (mm)			
	g_2	l_1	l_2	h_1
1	1.5	48	1.8	6.7
2	1.5	48.2	2	6.9
3	1.5	48.4	2.2	7.1
4	1.7	48	2	7.1
5	1.7	48.2	2.2	6.7
6	1.7	48.4	1.8	6.9
7	1.9	48	2.2	6.9
8	1.9	48.2	1.8	7.1
9	1.9	48.4	2	6.7

TABLE 4: OA (9, 4, 3, and 0.2) matrix for the optimized antenna.

Experiment	Design variable (mm)			
	g_2	l_1	l_2	h_1
1	2.6	48	4	6.7
2	2.6	48.2	4.2	6.9
3	2.6	48.4	4.4	7.1
4	2.8	48	4.2	7.1
5	2.8	48.2	4.4	6.7
6	2.8	48.4	4	6.9
7	3	48	4.4	6.9
8	3	48.2	4	7.1
9	3	48.4	4.2	6.7

4. Robust Optimization Result

The simulated reflection coefficients of the conventional and optimized antennas are depicted in Figure 5. The -6 dB reflection bandwidths of the conventional and optimized antennas are 72 MHz (822–894 MHz) and 70 MHz (824–894 MHz), respectively. Therefore, the optimized

antenna covers the GSM850 band. The dimensions of the optimized antenna are as follows: $g_1 = 1.7$ mm, $g_2 = 2.8$ mm, $l_1 = 48.2$ mm, $l_2 = 4.2$ mm, $w_1 = 2$ mm, $w_2 = 2$ mm, $d_1 = 4.5$ mm, $d_2 = 13.5$ mm, and $h_1 = 6.9$ mm.

The simulated peak gains of the conventional and optimized antennas are shown in Figure 6. In the GSM850 band, the peak gains of the conventional and optimized antennas

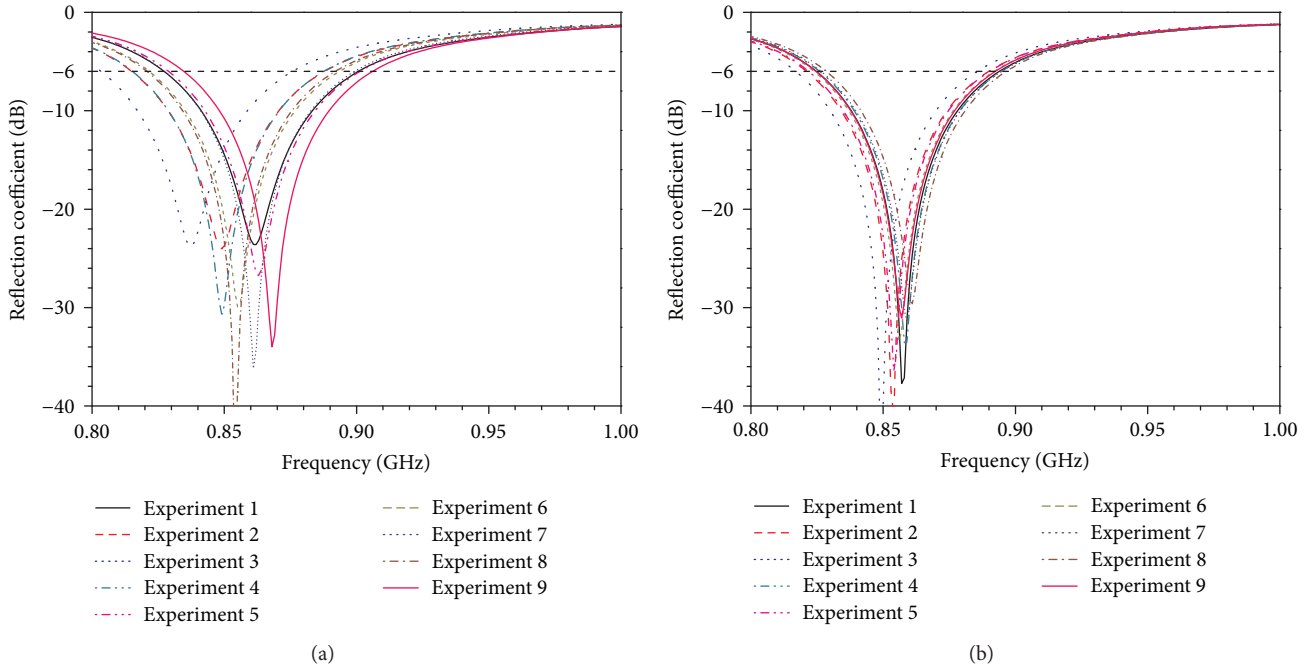


FIGURE 8: Simulated reflection coefficients of the antenna using the experimental parameters listed in (a) Table 3 and (b) Table 4.

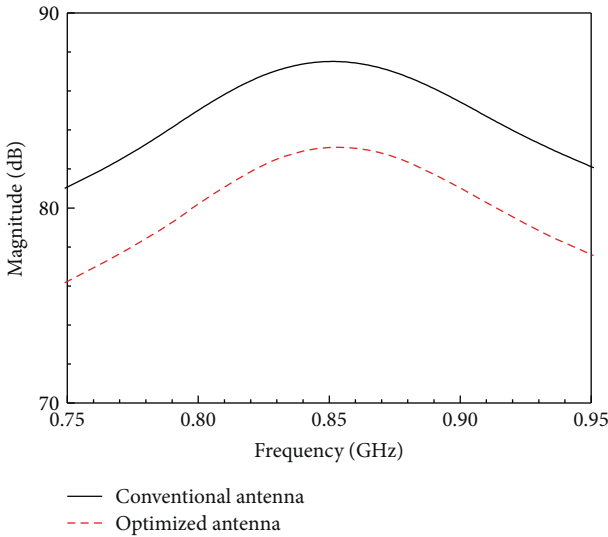


FIGURE 9: Simulated magnitudes of the electric fields at the center of g_2 in the conventional and optimized antennas.

vary from -1.56 to 0.62 dBi and from -1.21 to 0.79 dBi, respectively. The peak gain of the optimized antenna is slightly higher than that of the conventional antenna at higher frequencies. Figure 7 shows the simulated radiation patterns for the conventional and optimized antennas. The radiation patterns are simulated at the resonant frequency of each antenna and observed on three cutting planes (xy -, xz -, and yz -planes). The 3D radiation patterns of each antenna are also depicted. The simulation results provide evidence that the radiation patterns are similar to each other.

The OA matrices for the noise factors of the conventional and optimized antennas are listed in Tables 3 and 4,

respectively. Based on the design variables listed in Tables 3 and 4, the reflection coefficients of the antennas are simulated, as shown in Figure 8. In Figure 8(a), the minimum and maximum resonant frequencies among the nine results for the conventional antenna are 837 MHz and 868 MHz (variance: 31 MHz). For the optimized antenna, the minimum and maximum resonant frequencies arise at 849 MHz and 861 MHz (variance: 12 MHz; see Figure 8(b)). These results demonstrate that the robustness of the optimized antenna is improved by 61.3% as compared to that of the conventional antenna.

5. Experimental Result

In this work, the metal frame exists near the IFA, which can deteriorate the robustness of the antenna. Strong undesired coupling can be generated between the metal frame and the edge of the antenna because the antenna emits most of its radiation energy from its edge. In order to investigate the degree of coupling, the magnitudes of the electric fields at the center of g_2 are simulated. These results are presented in Figure 9. The magnitudes of the electric fields in the conventional and optimized antennas are 87.5 dB and 83.1 dB at 856 MHz, respectively. This outcome indicates that the coupling between the metal frame and the antenna can be decreased by increasing g_2 . For this reason, g_2 is the dominant parameter in the design of the robust antenna proposed in this paper.

To verify the experimental results, conventional and optimized antennas are fabricated and measured while varying g_2 . Figure 10 shows a photograph of the fabricated models and the test jig used for the measurement. In the test jig, short and feed pins are connected to the ground plane of the PCB and SMA connectors (port), respectively. In addition, the

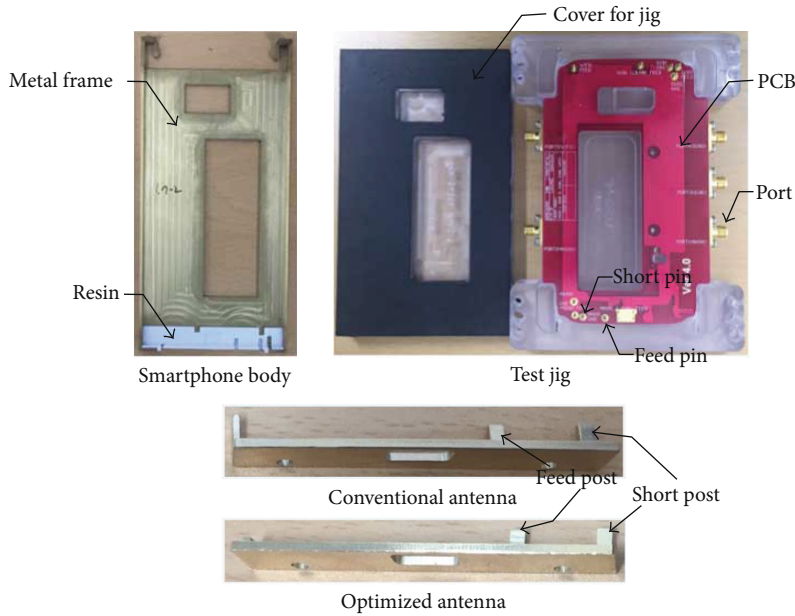


FIGURE 10: Photograph of the fabricated models and test jig.

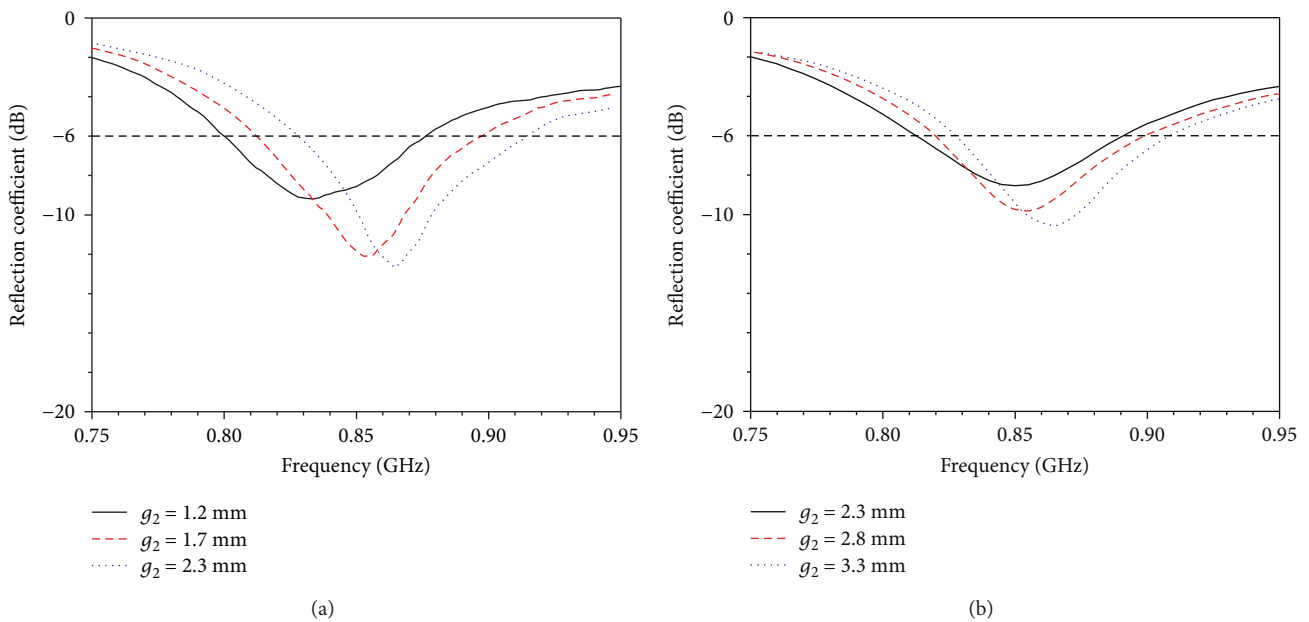


FIGURE 11: Measured reflection coefficients of the (a) conventional and (b) optimized antennas according to variation of the g_2 .

short and feed posts of the fabricated antennas correspondingly linked to the short and feed pins on the test jig to obtain the reflection coefficient, which is measured using an Agilent 8510C network analyzer. Figure 11 shows the measured reflection coefficients of the conventional and optimized antennas according to variations of g_2 . When g_2 for the conventional antenna is changed from 1.2 mm to 2.2 mm, the variance of the resonant frequency is 30 MHz (834–864 MHz). On the other hand, for the optimized antenna, the variance is 15 MHz (850–865 MHz) under identical conditions. These results indicate that the robustness of the optimized antenna is enhanced compared to that of the conventional antenna.

6. Conclusion

In this study, a hybrid robust optimization method developed on the basis of the GSO and OA was proposed. The proposed method was utilized to satisfy the -6 dB reflection bandwidth requirement of the metal frame antenna and to derive robust design parameters for antenna manufacturing tolerances. Conventional and optimized antennas were fabricated to verify the simulated results. The simulated and measured results indicated that the robustness of the optimized antenna is enhanced by 61.3% compared to that of the conventional antenna. Therefore, the proposed optimization scheme can be feasibly

applied to the robust design of various antennas for smart-phone applications.

Conflicts of Interest

The authors declare that they have no conflicts of interest.

Acknowledgments

This work was supported by the Technical Cooperation Project of Samsung Electronics.

References

- [1] H. Chen and A. Zhao, "LTE antenna design for mobile phone with metal frame," *IEEE Antennas and Wireless Propagation Letters*, vol. 15, pp. 1462–1465, 2016.
- [2] J.-H. Ko, J.-K. Byun, J.-S. Park, and H.-S. Kim, "Robust design of dual band/polarization patch antenna using sensitivity analysis and Taguchi's method," *IEEE Transactions on Magnetics*, vol. 47, no. 5, pp. 1258–1261, 2011.
- [3] W.-C. Weng and C. Choi, "Optimal design of CPW slot antennas using Taguchi's method," *IEEE Transactions on Magnetics*, vol. 45, no. 3, pp. 1542–1545, 2009.
- [4] J.-H. Ko, K.-T. Kim, D.-H. Kim, H.-B. Lee, and H.-S. Kim, "A practical approach to robust design of a RFID triple-band PIFA structure," *IEEE Transactions on Magnetics*, vol. 46, no. 8, pp. 3333–3336, 2010.
- [5] K.-T. Kim, J.-H. Ko, K. Choi, and H.-S. Kim, "Robust optimum design of PIFA for RFID mobile dongle applications," *IEEE Transactions on Magnetics*, vol. 47, no. 5, pp. 962–965, 2011.
- [6] J.-T. Tsai, J.-H. Chou, and T.-K. Liu, "Tuning the structure and parameters of a neural network by using hybrid Taguchi-genetic algorithm," *IEEE Transactions on Neural Networks*, vol. 17, no. 1, pp. 69–80, 2006.
- [7] M. Bachlaus, M. K. Pandey, C. Mahajan, R. Shankar, and M. K. Tiwari, "Designing an integrated multi-echelon agile supply chain network: a hybrid Taguchi-particle swarm optimization approach," *Journal of Intelligent Manufacturing*, vol. 19, no. 6, pp. 747–761, 2008.
- [8] A. Gandelli, F. Grimaccia, M. Mussetta, P. Pirinoli, and R. E. Zich, "Genetical swarm optimization: an evolutionary algorithm for antenna design," *Automatika*, vol. 47, no. 3-4, pp. 105–112, 2006.
- [9] J. Yun and J. Choi, "Low-profile planar inverted-F antenna for ultrawideband applications," *Journal of Electromagnetic Engineering and Science*, vol. 16, no. 4, pp. 235–240, 2016.
- [10] D. Kwon, S.-J. Lee, J.-W. Kim, B. Ahn, J.-W. Yu, and W.-S. Lee, "An eight-element compact low-profile planar MIMO antenna using LC resonance with high isolation," *Journal of Electromagnetic Engineering and Science*, vol. 16, no. 3, pp. 194–197, 2016.
- [11] J. Yousaf, H. Jung, K. Kim, and W. Nah, "Design, analysis, and equivalent circuit modeling of dual band PIFA using a stub for performance enhancement," *Journal of Electromagnetic Engineering and Science*, vol. 16, no. 3, pp. 169–181, 2016.
- [12] W.-C. Weng, F. Yang, and A. Z. Elsherbeni, "Linear antenna array synthesis using Taguchi's method: a novel optimization technique in electromagnetics," *IEEE Transactions on Antennas and Propagation*, vol. 55, no. 3, pp. 723–730, 2007.

Research Article

An Antenna Array Sidelobe Level Reduction Approach through Invasive Weed Optimization

Geng Sun ^{1,2,3} Yanheng Liu,^{1,2} Han Li,¹ Shuang Liang,^{1,4} Aimin Wang ^{1,2} and Boyu Li¹

¹College of Computer Science and Technology, Jilin University, Changchun, Jilin 130012, China

²Key Laboratory of Symbolic Computation and Knowledge Engineering of Ministry of Education, Jilin University, Changchun, Jilin 130012, China

³School of Electrical and Computer Engineering, Georgia Institute of Technology, Atlanta, GA 30302, USA

⁴Department of Information Technology, Changchun Vocational Institute of Technology, Changchun 130033, China

Correspondence should be addressed to Aimin Wang; wang_ai_min@126.com

Received 26 July 2017; Revised 10 November 2017; Accepted 11 December 2017; Published 13 February 2018

Academic Editor: Symeon Nikolaou

Copyright © 2018 Geng Sun et al. This is an open access article distributed under the Creative Commons Attribution License, which permits unrestricted use, distribution, and reproduction in any medium, provided the original work is properly cited.

The problems of synthesizing the beam patterns of the linear antenna array (LAA) and the circular antenna array (CAA) are addressed. First, an optimization problem is formulated for reducing the maximum sidelobe level (SLL) of the beam patterns. Then, the formulated problem is solved by using the invasive weed optimization (IWO) algorithm. Various simulations are performed to evaluate the effectiveness of the IWO algorithm for the synthesis of the beam patterns of the LAA and the CAA. The results show that IWO has a better performance in terms of the accuracy, the convergence rate, and the stability compared with other algorithms for the SLL reductions. Moreover, the electromagnetic simulation results also show that IWO achieves the best performance for the beam pattern synthesis of the antenna arrays in practical conditions.

1. Introduction

With the rapid development of the communication technologies and the explosive growth of the number of users, the capacity of a communication system has bottlenecks [1]. Usage of the antenna arrays can improve the capacity and the spectral efficiency of a wireless communication system [2, 3]. For example, the fifth generation (5G) communications adopt the millimeter wave (mm-wave) and beamforming technologies based on antenna arrays, to improve the spectral efficiency and communication rate of the system [4]. Moreover, the energy efficiency of a communication system can be enhanced by using the antenna arrays [5].

Beam pattern characteristic is one of the most important properties of an antenna array [6]. A directional mainlobe with the low sidelobe level (SLL) of the beam pattern will effectively enhance the communication quality and reduce the interferences [7, 8]. Thus, synthesizing the beam pattern

of an antenna array is very important. The classical synthesis methods for antenna arrays, such as the perturbation methods [9], are used to optimize the beam patterns, but it requires considerable work and rich debugging experiences. Thus, practicing this method is not reliable. Moreover, existing array-weighting optimization schemes, for example, the Dolph-Chebyshev [10] and the Taylor [11] approaches, have already been tested experimentally to be an effective method to solve the beam pattern optimization problems. However, these approaches are only suitable for synthesizing the antenna arrays with less numbers of antenna elements. In addition, there are strict restrictions for using such approaches.

Swarm intelligence and evolutionary algorithms are efficient methods for the beam pattern synthesis of the antenna arrays. These algorithms are suitable for solving large-scale antenna array synthesis problems since they do not require any restrictions on antenna arrays. Todnatee and Phongcharoenpanich [12] use a method based on genetic algorithm

(GA) to synthesize the radiation pattern of a nonuniform linear antenna array (LAA), and a maximum SLL of -20 dB can be achieved by the proposed method. Chakravarthy and Rao [13] propose to use a particle swarm optimization- (PSO-) based algorithm to synthesize the beam pattern of a circular antenna array (CAA). Reference [14] also uses PSO as the optimizer to synthesize the pencil beam pattern of the time-modulated concentric circular antenna array (CCAA). Sharaqa and Dib [15] optimize the beam patterns of the CAA and the CCAA by using the firefly algorithm (FA); the excitation currents and the spacing between the elements are jointly optimized for reducing the maximum SLL. Singh and Salgotra [16] use the flower pollination algorithm (FPA) to determine the excitation currents of a LAA for reducing the maximum SLL and controlling the nulls. Li et al. [7] utilize a biogeography-based optimization (BBO) algorithm to suppress the maximum SLL of the LAA and CAA. Reference [4] also uses a BBO-based method to reduce the maximum SLL as well as to achieve the deep nulls. Saxena and Kothari [17] optimize the beam pattern of the LAA by using the grey wolf optimization (GWO) algorithm. Sun et al. [18] adopt a strategy based on cuckoo search (CS) algorithm to suppress the maximum SLL of the CCAA. The authors in [19] also use a CS-based algorithm to synthesize the beam patterns of a large-scale planar antenna array (PAA). Reference [20] utilizes the social network optimization (SNO) algorithm to design the PAA, and the results are compared with the stud genetic algorithm. Saxena and Kothari [21] use the ant lion optimization (ALO) to suppress the maximum SLL and to control the deep nulls of the LAA. In reference [22], a hybrid approach called particle swarm optimization and gravitational search algorithm-explore (PSOGSA-E) is proposed to reduce the maximum SLL of the random antenna array. Reference [23] uses the binary spider monkey optimization algorithm to design the work status of each element of the CCAA for achieving a lower maximum SLL.

In this paper, the invasive weed optimization (IWO) [24] is employed to solve the beam pattern synthesis problems of the LAA and the CAA for reducing the maximum SLL. First, we formulate a beam pattern optimization problem for reducing the maximum SLLs of the LAA and the CAA. Second, we use the IWO algorithm to solve the formulated problem. Then, the key parameters of the IWO algorithm are tuned to achieve better performance for synthesizing the beam patterns. Finally, we conduct simulations based on different numbers of antenna elements for the LAA and the CAA, respectively, to verify the effectiveness of IWO. Moreover, the electromagnetic (EM) simulations are also conducted to evaluate the beam patterns in practical conditions. The results show that IWO achieves the best performance compared with other algorithms for the LAA and the CAA optimization problems.

The rest of this paper is organized as follows. Section 2 discusses the geometries and the array factors of LAAs and CAAs. Section 3 formulates the sidelobe reduction problem. Section 4 introduces the IWO algorithm. Section 5 shows the simulation results. Section 6 summarizes the findings and concludes the paper.

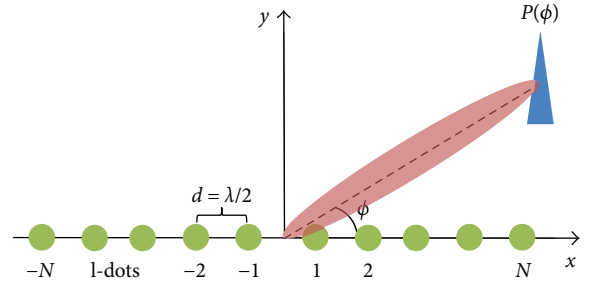


FIGURE 1: Geometry of $2N$ -element-symmetric LAA placed along the x -axis.

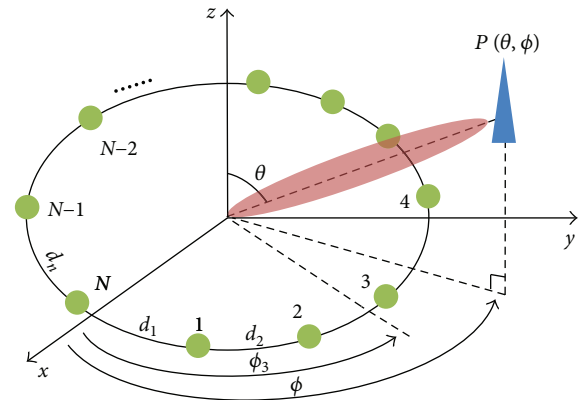


FIGURE 2: Geometry of a nonuniform CAA with N isotropic antennas.

2. System Model

In this section, the geometry structures and the array factors (AF) of LAA and CAA are introduced.

2.1. LAA. Figure 1 shows an LAA with $2N$ elements that are symmetrically distributed along the x -axis. The elements of the LAA are assumed as the isotropic radiators. Thus, according to the electromagnetic wave superposition principle, the AF of an LAA is expressed as follows [25]:

$$\text{AF}(\phi) = \sum_{n=-N}^N I_n \cos(kx_n \cos(\phi) + \varphi_n), \quad (1)$$

where k represents the wave number, I_n is the excitation current of the n th element, α_n is the phase of the n th element, x_n is the location of the n th element, and ϕ is the azimuth angle measured from the positive x -axis.

2.2. CAA. Figure 2 shows the geometry of a CAA with N isotropic antenna elements lying on the x - y plane ($\theta = 90^\circ$). These elements are uniformly placed on a ring with the radius of a . Similar with the LAA, the elements of the CAA are also assumed to be isotropic radiators. The AF of a CAA can be written as follows [4]:

$$AF(\theta, \phi) = \sum_{i=1}^N I_n \exp(j[ka \sin(\theta) \cos(\phi - \phi_n) + \alpha_n]),$$

$$ka = \frac{2\pi}{\lambda} a = \sum_{i=1}^N d_i, \quad (2)$$

$$\phi_n = \frac{2\pi \sum_{i=1}^n d_i}{ka},$$

$$\alpha_n = -ka \sin(\theta_0) \cos(\phi_0 - \phi_n),$$

where I_n is the excitation current of the n th element, α_n is the phase of the n th element, and d_n represents the arc distance between elements n and $n-1$ (d_1 is the arc distance between the first ($n=1$) and the last ($n=N$) elements). ϕ_n and θ_n represent the azimuth angle measured from the positive x -axis and the elevation angle measured from the z -axis, respectively. Moreover, θ_0 and ϕ_0 are set to be 90° and 0° , respectively.

3. Problem Formulation

This work is aiming to design the antenna arrays with minimum SLL. The excitation currents I of the antenna elements affect the beam pattern directly; hence, an optimal set of excitation currents for each element need to be determined to achieve lower SLL. Therefore, the optimization problem can be formulated as follows:

Minimize

$$f = 10 \log_{10} \frac{|AF(\phi_{MSL})|}{|AF(\phi_{ML})|}, \quad (3)$$

subject to

$$\phi_{ML} = \arg \max |AF(\phi)|, \quad \phi \in [-\pi, \pi], \quad (4)$$

$$\phi_{MSL} \in \max([-\pi, \phi_{FN1}] \cup [\phi_{FN2}, \pi]), \quad (5)$$

$$0 \leq I_n \leq 1, \quad (6)$$

where ϕ_{MSL} is the angle of the maximum SLL and ϕ_{ML} is the angle of the mainlobe, ϕ_{FN1} and ϕ_{FN2} are the first nulls in $(-\pi, \phi_{FN1})$ and $(-\pi, \phi_{FN2})$, respectively, and the first null beamwidth (FNBW) of the beam pattern can be determined by them. The constraint (4) determines the location of the mainlobe, the constraint (5) shows the range of the sidelobe, and the constraint (6) specifies the range of the normalized excitation current of each element.

4. Invasive Weed Optimization Algorithm

IWO is a novel numerical stochastic optimization algorithm inspired from weed colonization, and it is first proposed by Mehrabian and Lucas in reference [24]. In the IWO approach, the whole population is composed of a certain number of weeds, and each weed is made up of a set of decision variables. The weed is a plant that is vigorous and invasive, and it poses a serious threat to the desirable plants. These features show that the weeds are very robust and troublous in the agriculture.

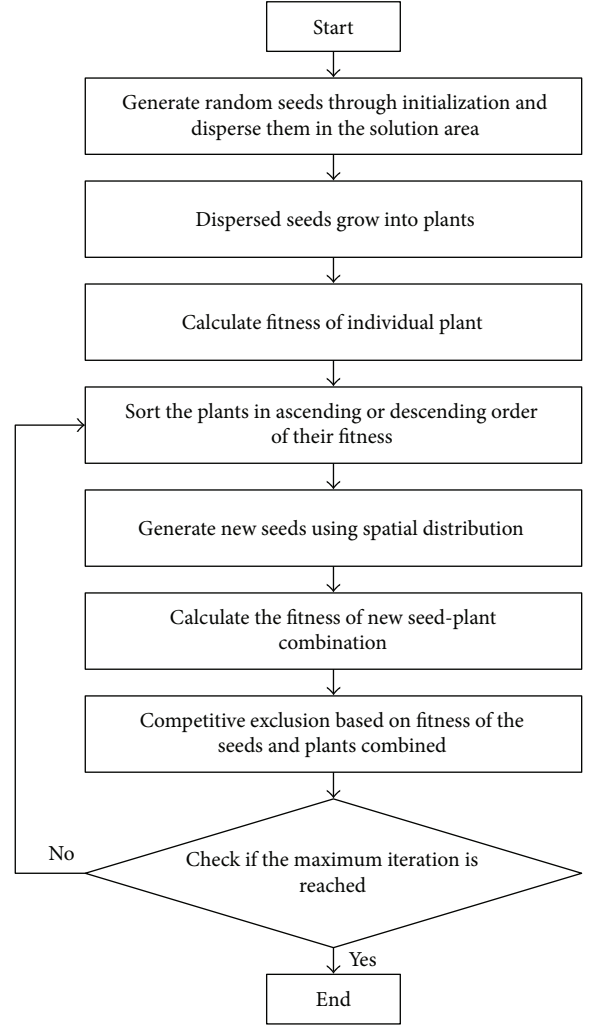


FIGURE 3: Flowchart of the IWO algorithm.

The working mechanism of IWO tried to imitate adaptation, robustness, and randomness of weeds in a very concise and efficient pattern. For a minimization problem, a weed with lower fitness value can generate more number of seeds. On the contrary, a weed with higher fitness value generates less number of seeds. The number of the newly generated seeds is decreased linearly from the maximum to the minimum allowable seeds in the colony. These newly generated seeds will be dispersed among the solution space with mean zero and varying standard deviations of normal distribution, and they will grow into new weeds. These weeds will generate new seeds. Moreover, in order to keep the certain number of the whole population, the weeds with worse fitness values will be eliminated from the colony.

The main procedure of IWO is shown in Figure 3, and the details of this algorithm are presented as follows. where S_{\min} and S_{\max} are the minimum and maximum number of the seeds, respectively, f is the fitness value of a certain weed, f_{worst} and f_{best} denote the worst and best fitness values in a certain iteration, respectively, and floor is the round down operation. where σ_{initial} and σ_{final} are the predefined initial and final standard deviations, respectively. iter is the current

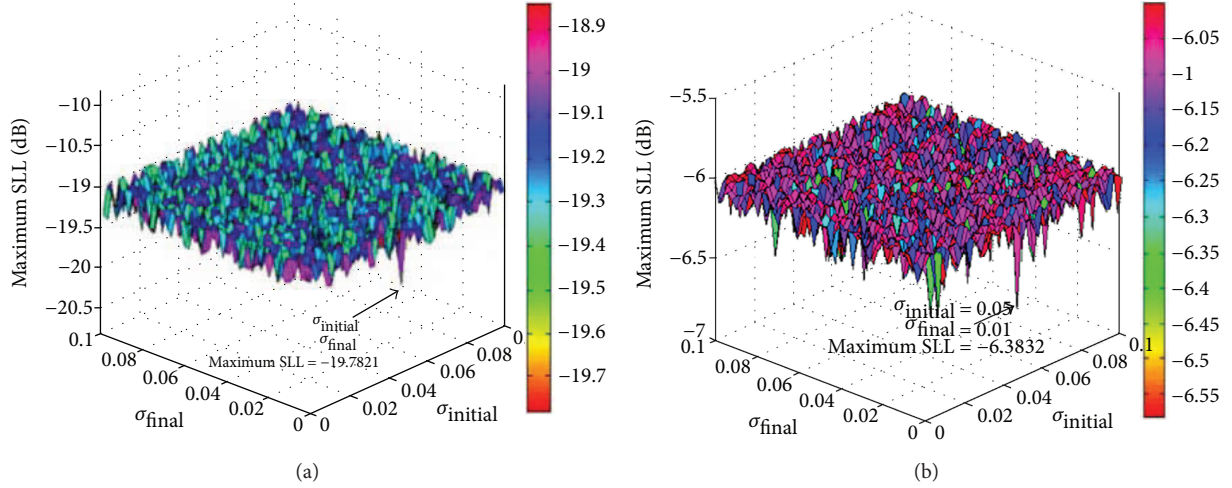


FIGURE 4: Parameter tunings for σ_{initial} and σ_{final} in IWO for reducing the maximum SLL of the 8-element antenna arrays. (a) LAA. (b) CAA.

iteration and m is the nonlinear modulation index. W^{iter} is a weed in the iterth iteration, $N(0, \sigma_{\text{iter}}^2)$ is a normal random number with mean zero and standard deviation σ_{iter} .

Step 1. Initialization. In the first step of IWO, the algorithm initializes a certain number of weeds (candidate solutions) to construct a population and disperse these solutions to the d dimensional problem space uniformly and randomly.

Step 2. Reproduction. In this step, each solution in the population reproduces seeds according to its own lowest and highest fitness values in the colony. The number of seeds reproduced by a weed is given as follows:

$$S = \text{floor} \left[S_{\min} + (S_{\max} - S_{\min}) \times \frac{f - f_{\text{worst}}}{f_{\text{best}} - f_{\text{worst}}} \right], \quad (7)$$

Step 3. Spatial dispersal. Next, the newly generated seeds will be distributed over the d dimensional searching space and randomly spread in the vicinity of their parent weeds in the normal distribution with mean zero and varying standard deviations, to grow into new weeds. By this way, the search efficiency can be enhanced. The computing method of the standard deviation σ_{iter} in a specific iteration is shown in (8), and the new weeds can be generated by (9).

$$\sigma_{\text{iter}} = \frac{(\text{iter}_{\max} - \text{iter})^m}{\text{iter}_{\max}^m} \times (\sigma_{\text{initial}} - \sigma_{\text{final}}) + \sigma_{\text{final}}, \quad (8)$$

$$W_{\text{new}}^{\text{iter}} = W^{\text{iter}} + N(0, \sigma_{\text{iter}}^2), \quad (9)$$

Step 4. Competitive exclusion. After several iterations, the number of weeds in the colony will exceed the predefined maximum limited value due to the growth and reproduction of the weeds. Therefore, an elimination mechanism needs to be applied to eliminate the weeds with worse fitness values until the maximum number of weeds in the colony is reached. Then, the reserved ones will remain to the next iteration.

For the beam pattern synthesis of the antenna array with IWO, the excitation currents of the elements can be regarded

as a candidate solution in IWO and the solution can be expressed as follows:

$$x = (I_1, I_2, I_3, \dots, I_n), \quad (10)$$

where n is the number of antenna elements. Then, the population of IWO can be written as follows:

$$\text{pop} = \begin{bmatrix} x_1 \\ x_1 \\ \dots \\ x_N \end{bmatrix} = \begin{bmatrix} I_1^1, I_2^1, I_3^1, \dots, I_n^1 \\ I_1^2, I_2^2, I_3^2, \dots, I_n^2 \\ \dots \\ I_1^N, I_2^N, I_3^N, \dots, I_n^N \end{bmatrix}, \quad (11)$$

where N is the population size.

5. Simulation and Analysis

In this section, the beam pattern synthesis for reducing the SLL of the LAA and the CAA is simulated by Matlab. The simulations are performed on a computer with an Intel (R) Core (TM) 2 Duo CPU and a 3.00 GB RAM. First, the main parameters of IWO are tuned to achieve the best performance for the beam pattern synthesis. Second, usage of IWO to synthesize the beam pattern is simulated and the results are compared with CS, FA, BBO, and PSO. Then, the stabilities of IWO and these benchmark algorithms are compared. Finally, we conduct EM simulations to verify the optimization performance of the antenna arrays in practical conditions.

5.1. Parameter Tunings and Setups. The parameter values of σ_{initial} and σ_{final} control the main updating procedure of IWO. Thus, they will be jointly tuned for achieving better performance of the algorithm. In the tuning test, the ranges of σ_{initial} and σ_{final} are (0.01, 0.1) and (0.01, 0.1), respectively, and the steps are both 0.002. Thus, the total number of points for a tuning test is 2500. The tests are independently repeated for 50 times and the average values are

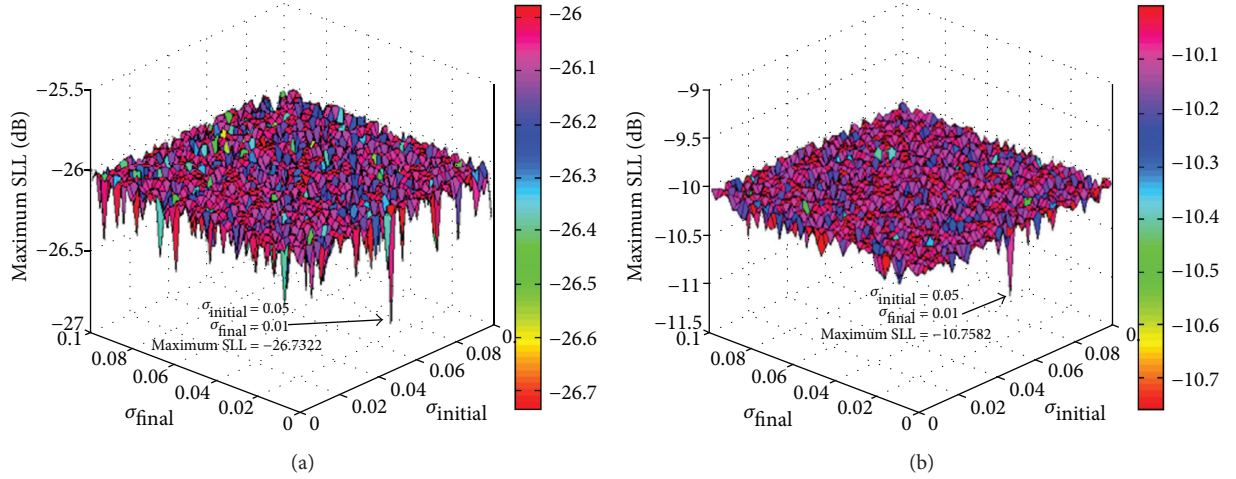


FIGURE 5: Parameter tunings for σ_{initial} and σ_{final} in IWO for reducing the maximum SLL of the 16-element antenna arrays. (a) LAA. (b) CAA.

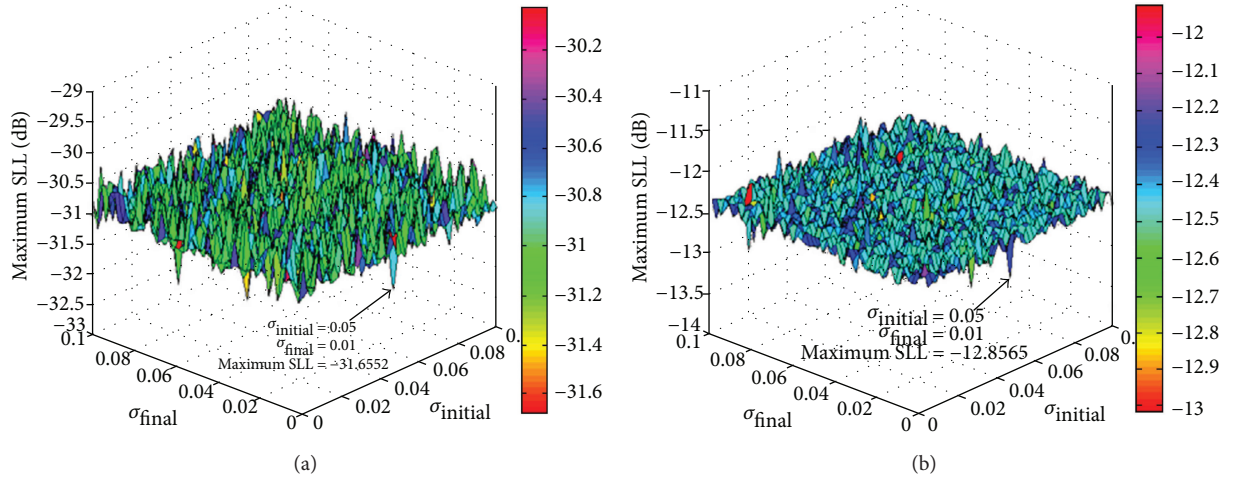


FIGURE 6: Parameter tunings for σ_{initial} and σ_{final} in IWO for reducing the maximum SLL of the 32-element antenna arrays. (a) LAA. (b) CAA.

TABLE 1: Parameter setups of IWO.

Parameters	Values
S_{max}	5
S_{min}	0
σ_{initial}	0.05
σ_{final}	0.01
m	3

presented. Figures 4(a), 4(b), 5(a), 5(b), 6(a), and 6(b) show the tuning results of the LAAs and the CAAs with 8, 16, and 32 elements. It can be seen from the figures that the optimal values of σ_{initial} and σ_{final} are 0.05 and 0.01, respectively, for both LAA and CAA.

The other parameters of IWO and the benchmark algorithms are shown in Table 1. Moreover, for the benchmark algorithms, we use the versions and the parameter values in [26–29] for BBO, CS, FA, and PSO, and the detailed parameter setups of these algorithms are shown in Table 2. Moreover, the population size and the maximum iteration of each algorithm are 20 and 200, respectively, for fairness.

TABLE 2: Parameter setups of the benchmark algorithms.

Algorithms	Parameters
BBO	Habitat modification probability: 1; immigration rate: 1; emigration rate: 1; mutation rate: 0.005
CS	Probability of egg detection: 0.25; step size of Lévy flight: 1
FA	Light absorption coefficient: 0.2; step factor: 0.6
PSO	Learning factor 1: 2; learning factor 2: 2

The time complexities of the algorithms above are analyzed here. The main computational cost will be the fitness function evaluations. Supposing the maximum number of iteration is t for each algorithm, then the time complexity of IWO is $O(N \cdot t)$ because there is only one inner loop in the algorithm; N is the population size. CS, FA, BBO, and PSO have similar algorithm structure with IWO; hence, the time complexities of these benchmark algorithms are also $O(N \cdot t)$. As can be seen, the computational costs of these algorithms are relatively inexpensive because the complexities are linear in terms of t .

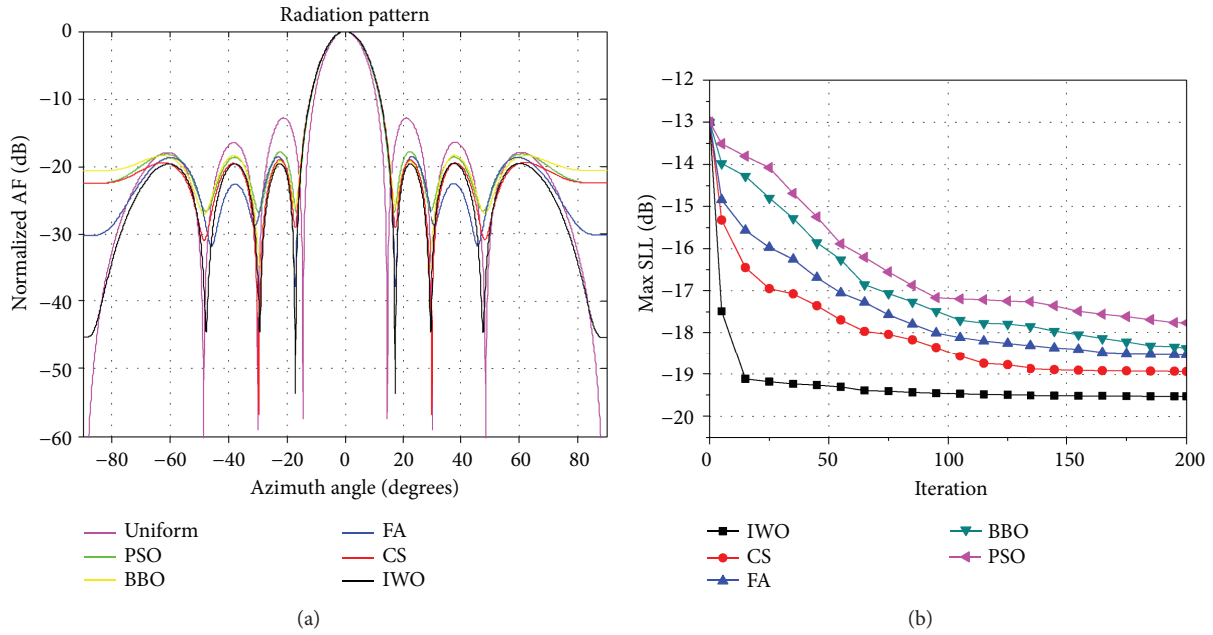


FIGURE 7: Beam patterns and convergence rates of the 8-element LAA obtained by different algorithms. (a) Beam patterns. (b) Convergence rates.

TABLE 3: Excitation currents and maximum SLL of the 8-element LAA obtained by different algorithms.

Algorithm	$(I_1, I_2, I_3, I_4, I_5, I_6, I_7, I_8)$	Max SLL (dB)
IWO	0.5891, 0.6562, 0.8840, 0.9855, 1.0000, 0.8575, 0.6712, 0.6115	-19.5215
CS	0.5853, 0.5491, 0.8083, 0.8071, 0.7859, 0.6131, 0.5531, 0.3801	-18.9278
FA	0.7033, 0.7033, 0.9412, 0.9381, 0.9565, 0.9082, 0.5943, 0.4540	-18.5229
BBO	0.4311, 0.4227, 0.6133, 0.6035, 0.8779, 0.6096, 0.5785, 0.4397	-18.3868
PSO	0.4634, 0.6319, 0.8124, 1.0000, 1.0000, 1.0000, 0.7746, 0.9151	-17.7736
Uniform	1.0000, 1.0000, 1.0000, 1.0000, 1.0000, 1.0000, 1.0000, 1.0000	-12.7972

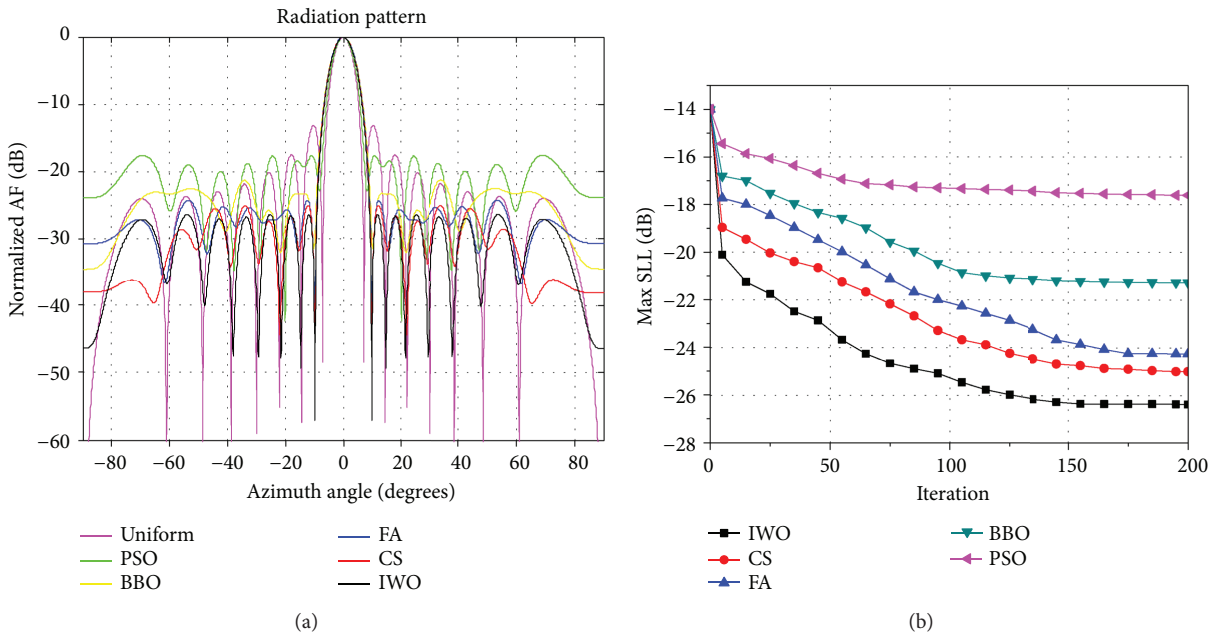


FIGURE 8: Beam patterns and convergence rates of the 16-element LAA obtained by different algorithms. (a) Beam patterns. (b) Convergence rates.

TABLE 4: Excitation currents and maximum SLL of the 16-element LAA obtained by different algorithms.

Algorithm	$(I_1, I_2, I_3, I_4, I_5, I_6, I_7, I_8, I_9, I_{10}, I_{11}, I_{12}, I_{13}, I_{14}, I_{15}, I_{16})$	Max SLL (dB)
IWO	0.3816, 0.3518, 0.4807, 0.5730, 0.7230, 0.8449, 0.8716, 0.9607, 0.9015, 0.9152, 0.8064, 0.7165, 0.6284, 0.4646, 0.3593, 0.3754	-26.3889
CS	0.2746, 0.4124, 0.4454, 0.6572, 0.6341, 0.7431, 0.8423, 0.8115, 0.9066, 0.7848, 0.7173, 0.7259, 0.5137, 0.3320, 0.3200, 0.3043	-25.0106
FA	0.2945, 0.3581, 0.4739, 0.6472, 0.6065, 0.6275, 0.7910, 0.9785, 0.7978, 0.6976, 0.7821, 0.6515, 0.5205, 0.4430, 0.1535, 0.2805	-24.2705
BBO	0.2211, 0.1887, 0.3124, 0.2465, 0.7824, 0.6565, 0.7495, 0.8711, 0.8811, 1.0000, 0.5846, 0.8090, 0.8059, 0.5463, 0.5439, 0.3832	-21.2792
PSO	1.0000, 0.0131, 0.4806, 0.5739, 1.0000, 1.0000, 1.0000, 1.0000, 1.0000, 1.0000, 1.0000, 1.0000, 1.0000, 1.0000, 1.0000, 1.0000	-17.6110
Uniform	1.0000, 1.0000, 1.0000, 1.0000, 1.0000, 1.0000, 1.0000, 1.0000, 1.0000, 1.0000, 1.0000, 1.0000, 1.0000, 1.0000, 1.0000, 1.0000	-13.1476

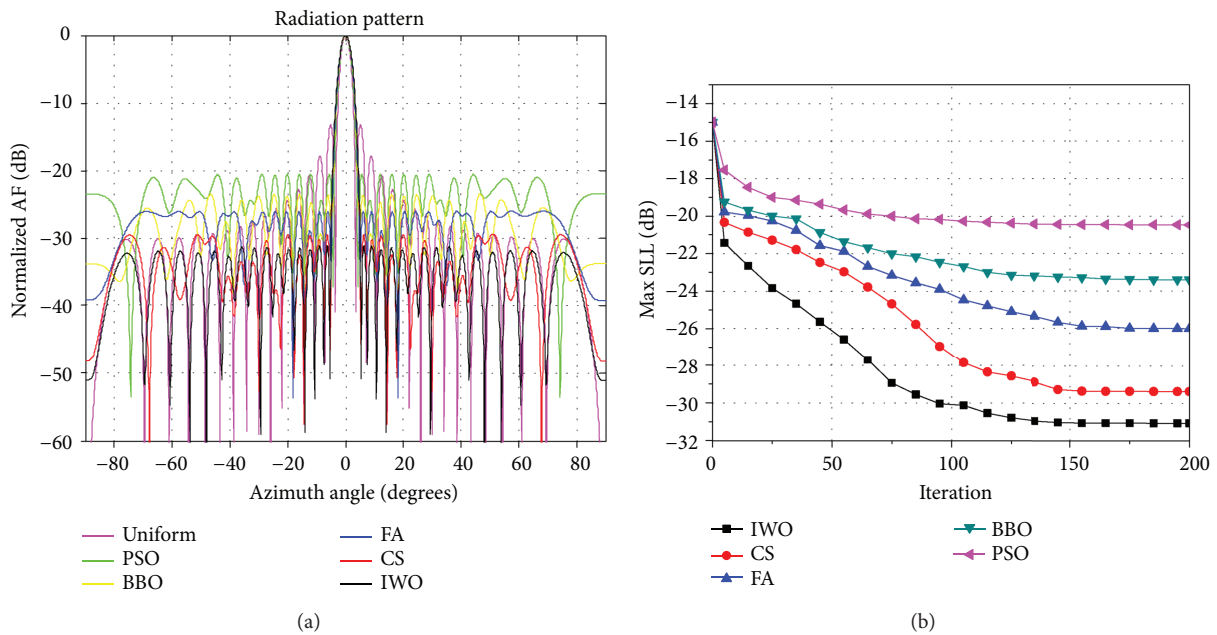


FIGURE 9: Beam patterns and convergence rates of the 32-element LAA obtained by different algorithms. (a) Beam patterns. (b) Convergence rates.

5.2. Beam Pattern Synthesis of the LAA. In this section, we use different algorithms to synthesize the beam patterns of the 8-element, 16-element, and 32-element LAAs, to compare the performances of these algorithms for the different dimensions of solutions.

5.2.1. Sample 1: Beam Pattern Synthesis for the 8-Element LAA. Figure 7(a) shows the beam patterns of an 8-element LAA obtained by the uniform array, PSO, BBO, FA, CS, and IWO. Note that the uniform array means that the excitation current of each antenna element is fixed as 1. Figure 7(b) shows the convergence rates during the optimization process of different algorithms. As can be seen, IWO has the best performance in terms of the accuracy as well as the convergence rate. Table 3 shows the maximum SLL obtained by these methods. It can be seen that the maximum SLL obtained by IWO is -19.5215 dB, which is the lowest among all the

algorithms. Moreover, the excitation currents optimized by each algorithm is also listed in Table 3.

5.2.2. Sample 2: Beam Pattern Synthesis for the 16-Element LAA. In this sample, the beam patterns of a LAA with 16 elements are synthesized by different approaches. Figure 8(a) shows the beam patterns obtained by different algorithms and Figure 8(b) shows the convergence rate of these algorithms. Table 4 compares the numerical results. It can be seen from the figures and table that IWO has the best performance in terms of the maximum SLL suppression and convergence rate in this case. In addition, the excitation currents obtained by different algorithms are also shown in Table 4.

5.2.3. Sample 3: Beam Pattern Synthesis for the 32-Element LAA. Figure 9(a) shows the beam patterns of a 32-element LAA optimized by different algorithms, and Table 5 presents that the maximum SLLs obtained by IWO, CS, FA,

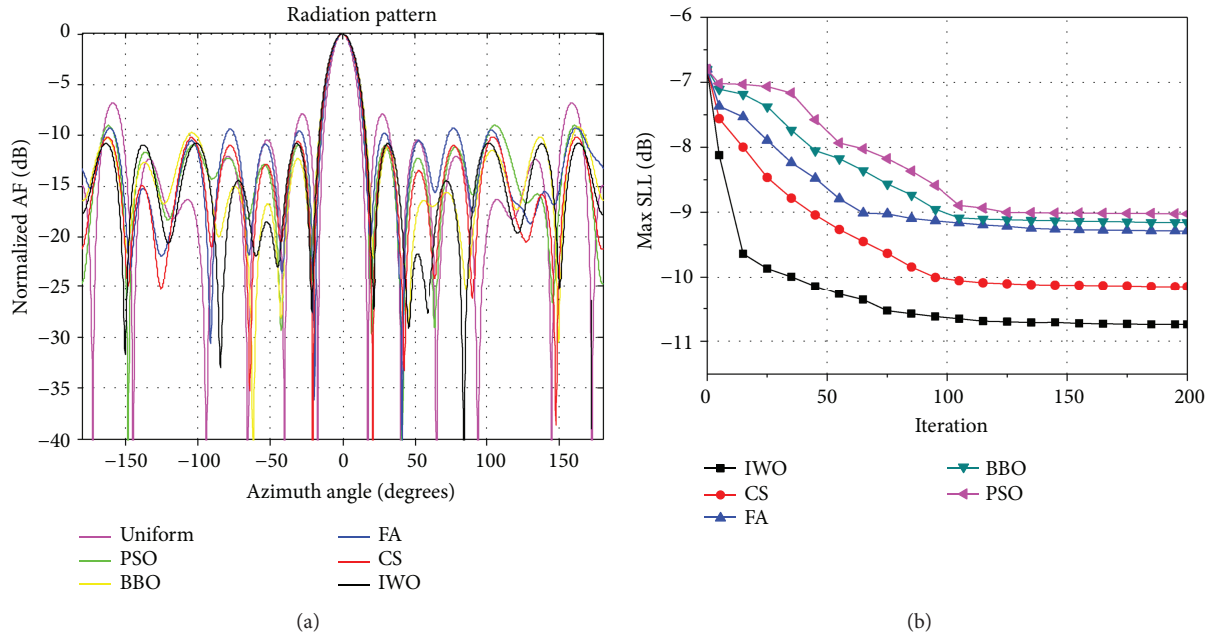


FIGURE 11: Beam patterns and convergence rates of the 16-element CAA obtained by different algorithms. (a) Beam patterns. (b) Convergence rates.

TABLE 7: Excitation currents and maximum SLLs of the 16-element CAA obtained by different algorithms.

Algorithm	$(I_1, I_2, I_3, I_4, I_5, I_6, I_7, I_8, I_9, I_{10}, I_{11}, I_{12}, I_{13}, I_{14}, I_{15}, I_{16})$	Max SLL (dB)
IWO	0.6134, 0.8125, 0.1244, 0.0000, 0.2476, 0.8644, 0.6049, 0.8260, 0.3362, 0.9878, 0.1337, 0.0000, 0.0091, 0.9322, 0.3423, 0.6827	-10.7440
CS	0.5780, 0.7596, 0.2491, 0.0546, 0.1192, 0.7774, 0.7137, 0.4641, 0.7711, 0.6402, 0.2849, 0.0799, 0.4616, 0.5811, 0.6121, 0.7003	-10.1490
FA	0.3282, 0.8088, 0.3292, 0.2406, 0.3882, 0.4132, 0.8062, 0.4230, 0.8580, 0.2449, 0.2122, 0.2156, 0.2339, 0.6581, 0.3901, 0.4245	-9.2885
BBO	1.0000, 1.0000, 0.4136, 0.0000, 0.0000, 0.9361, 0.7941, 1.0000, 0.3357, 1.0000, 0.0000, 0.4629, 0.0000, 1.0000, 0.5478, 1.0000	-9.1592
PSO	1.0000, 1.0000, 0.2790, 0.0003, 1.0000, 1.0000, 1.0000, 1.0000, 1.0000, 0.7687, 0.9998, 0.0000, 1.0000, 0.0000, 0.9998, 0.9564, 1.0000	-9.0261
Uniform	1.0000, 1.0000, 1.0000, 1.0000, 1.0000, 1.0000, 1.0000, 1.0000, 1.0000, 1.0000, 1.0000, 1.0000, 1.0000, 1.0000, 1.0000, 1.0000, 1.0000	-6.7578

BBO, and PSO are -31.0751 dB, -29.3774 dB, -26.0192 dB, -23.4108 dB, and -20.4785 dB, respectively. Moreover, the maximum SLL of the uniform array is -13.2318 dB. The excitation currents of these algorithms are also presented in the table. Figure 9(b) shows the convergence rates during the optimization process. Similar to the previous samples, IWO also has the best performance for this case.

5.3. Beam Pattern Synthesis of the CAA. The beam pattern synthesis results of the CAA are presented in this section. Corresponding to the case of LAA, three samples that are 8-element, 16-element, and 32-element CAAs are optimized by different algorithms.

5.3.1. Sample 4: Beam Pattern Synthesis for the 8-Element CAA. Figure 10(a) shows the beam patterns of an 8-element CAA optimized by different algorithms, and the

convergence rates of these methods are shown in Figure 10(b). The maximum SLLs obtained by these algorithms are listed in Table 6. As can be seen, the maximum SLL obtained by IWO is -6.2535 dB, which is the lowest among all the approaches. Moreover, the excitation currents obtained by different algorithms are also shown in Table 6.

5.3.2. Sample 5: Beam Pattern Synthesis for the 16-Element CAA. In this sample, we use different algorithms to optimize a 16-element CAA. Figures 11(a) and 11(b) show the beam pattern results and the convergence rates, respectively, and Table 7 compares the numerical results of the maximum SLL. As can be seen, the maximum SLL obtained by the uniform array, CS, FA, BBO, and PSO are -6.7578 dB, -10.1490 dB, -9.2885 dB, -9.1592 dB, and -9.0261 dB, respectively, and it is -10.7440 dB by using IWO. Thus, IWO achieves the best results for reducing the maximum SLL. Moreover,

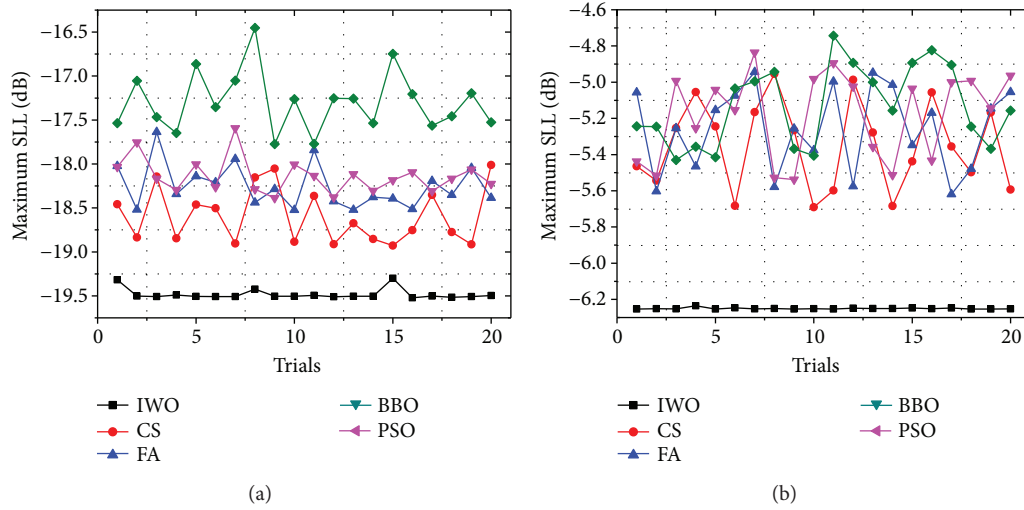


FIGURE 13: Stability test results of different algorithms of the 8-element antenna arrays. (a) LAA. (b) CAA.

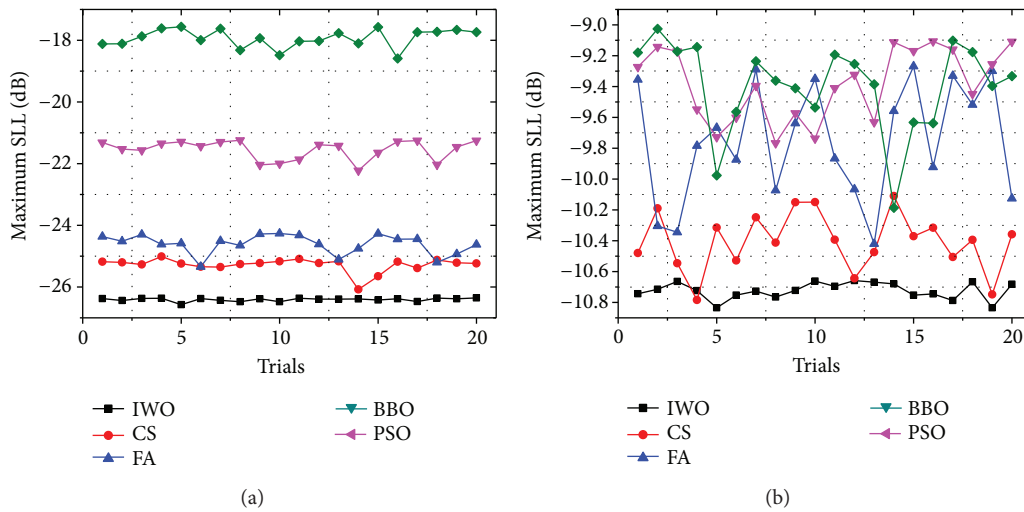


FIGURE 14: Stability test results of different algorithms of the 16-element antenna arrays. (a) LAA. (b) CAA.

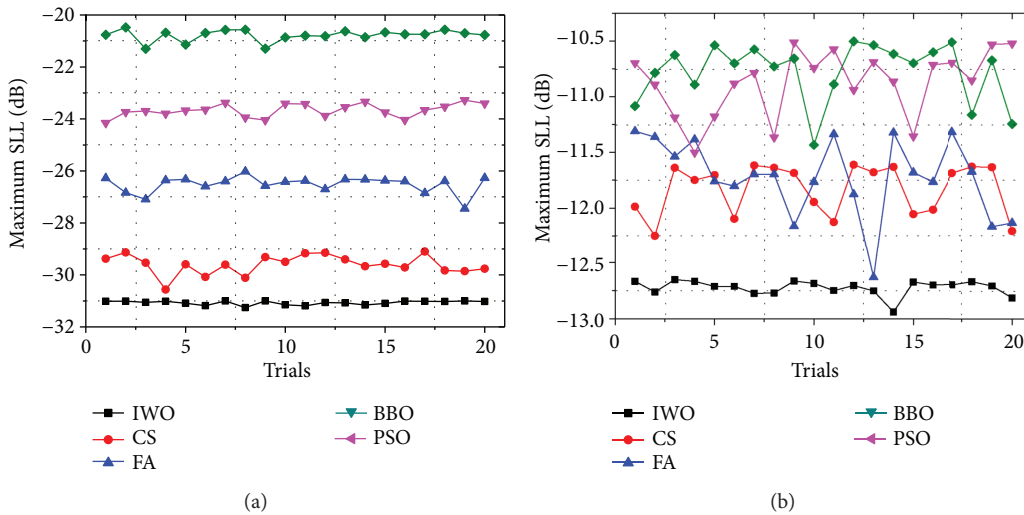


FIGURE 15: Stability test results of different algorithms of the 32-element antenna arrays. (a) LAA. (b) CAA.

TABLE 9: Statistical results of different algorithms for the beam pattern synthesis of the 8-element LAA.

	IWO	CS	FA	BBO	PSO
Best max SLL (dB)	-19.5215	-18.9278	-18.5229	-18.3868	-17.7736
Worst max SLL (dB)	-19.2991	-18.0124	-17.6362	-17.5935	-16.4526
Mean max SLL (dB)	-19.4814	-18.5891	-18.2556	-18.1386	-17.2987
SD max SLL (dB)	0.0623	0.3190	0.2489	0.2489	0.3416

TABLE 10: Statistical results of different algorithms for the beam pattern synthesis of the 16-element LAA.

	IWO	CS	FA	BBO	PSO
Best max SLL (dB)	-26.5733	-26.0809	-25.3447	-22.2250	-18.5918
Worst max SLL (dB)	-25.3512	-25.0106	-24.2640	-21.2444	-17.5628
Mean max SLL (dB)	-26.4087	-25.2805	-24.6071	-21.5447	-17.9288
SD max SLL (dB)	0.0550	0.2293	0.3180	0.3140	0.2986

TABLE 11: Statistical results of different algorithms for the beam pattern synthesis of the 32-element LAA.

	IWO	CS	FA	BBO	PSO
Best max SLL (dB)	-31.2566	-30.5608	-27.4520	-24.1520	-21.3014
Worst max SLL (dB)	-31.0004	-29.1010	-26.0192	-23.2783	-20.4785
Mean max SLL (dB)	-31.0725	-29.6016	-26.5173	-23.6655	-20.7816
SD max SLL (dB)	0.0770	0.3706	0.3293	0.2554	0.2256

TABLE 12: Statistical results of different algorithms for the beam pattern synthesis of the 8-element CAA.

	IWO	CS	FA	BBO	PSO
Best max SLL (dB)	-6.2535	-5.6903	-5.6191	-5.5380	-5.4304
Worst max SLL (dB)	-6.2351	-4.9543	-4.9435	-4.8355	-4.7435
Mean max SLL (dB)	-6.2502	-5.3487	-5.2555	-5.1819	-5.1311
SD max SLL (dB)	0.0042	0.2408	0.2336	0.2399	0.2222

TABLE 13: Statistical results of different algorithms for the beam pattern synthesis of the 16-element CAA.

	IWO	CS	FA	BBO	PSO
Best max SLL (dB)	-10.8352	-10.7847	-10.4207	-9.7679	-10.1871
Worst max SLL (dB)	-10.6590	-10.1100	-9.2688	-9.1071	-9.0261
Mean max SLL (dB)	-10.7242	-10.4058	-9.7527	-9.3833	-9.3953
SD max SLL (dB)	0.0541	0.1895	0.3816	0.2323	0.2946

TABLE 14: Statistical results of different algorithms for the beam pattern synthesis of the 32-element CAA.

	IWO	CS	FA	BBO	PSO
Best max SLL (dB)	-12.9380	-11.2514	-12.6309	-11.5015	-11.4336
Worst max SLL (dB)	-12.6506	-11.6105	-11.3092	-10.5104	-10.5015
Mean max SLL (dB)	-12.7218	-11.8298	-11.7194	-10.8731	-10.7724
SD max SLL (dB)	0.0675	0.2268	0.3515	0.2972	0.2660

of antenna elements. Tables 9, 10, 11, 12, 13, and 14 show the statistical results in terms of the best, the worst, the mean values of the maximum SLLs, and the standard divisions

(SD) of these trials. As can be seen, IWO achieves the lowest average maximum SLLs for both LAA and CAA. Moreover, the SDs of IWO are also the lowest which means that the

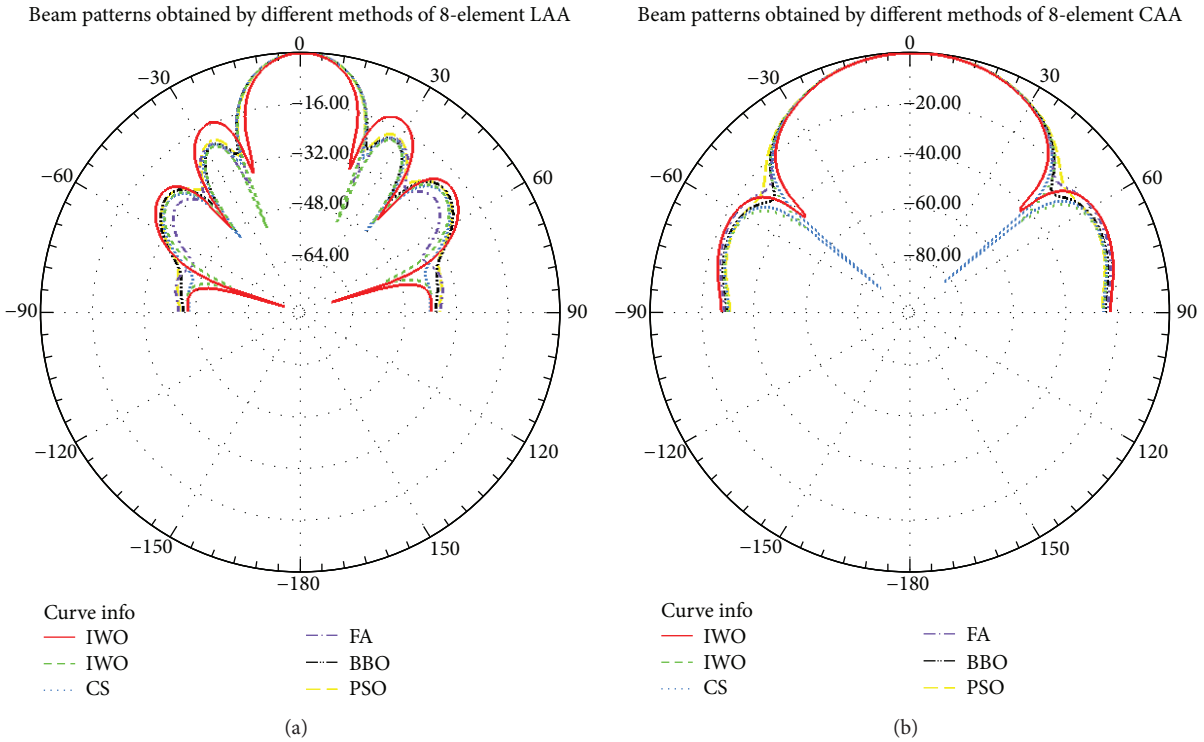


FIGURE 16: 2D beam pattern comparisons in polar coordinates based on different excitation currents obtained by different optimization methods in EM simulations. (a) 8-element LAA. (b) 8-element CAA.

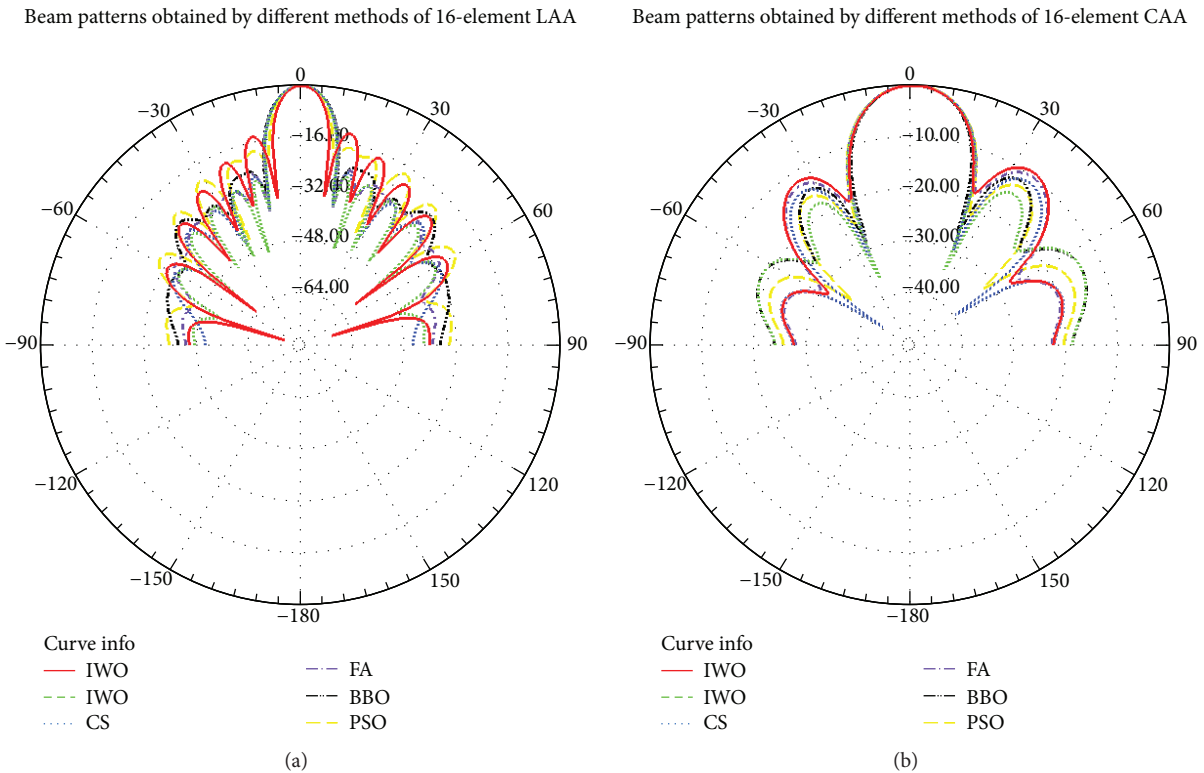


FIGURE 17: 2D beam pattern comparisons in polar coordinates based on different excitation currents obtained by different optimization methods in EM simulations. (a) 16-element LAA. (b) 16-element CAA.

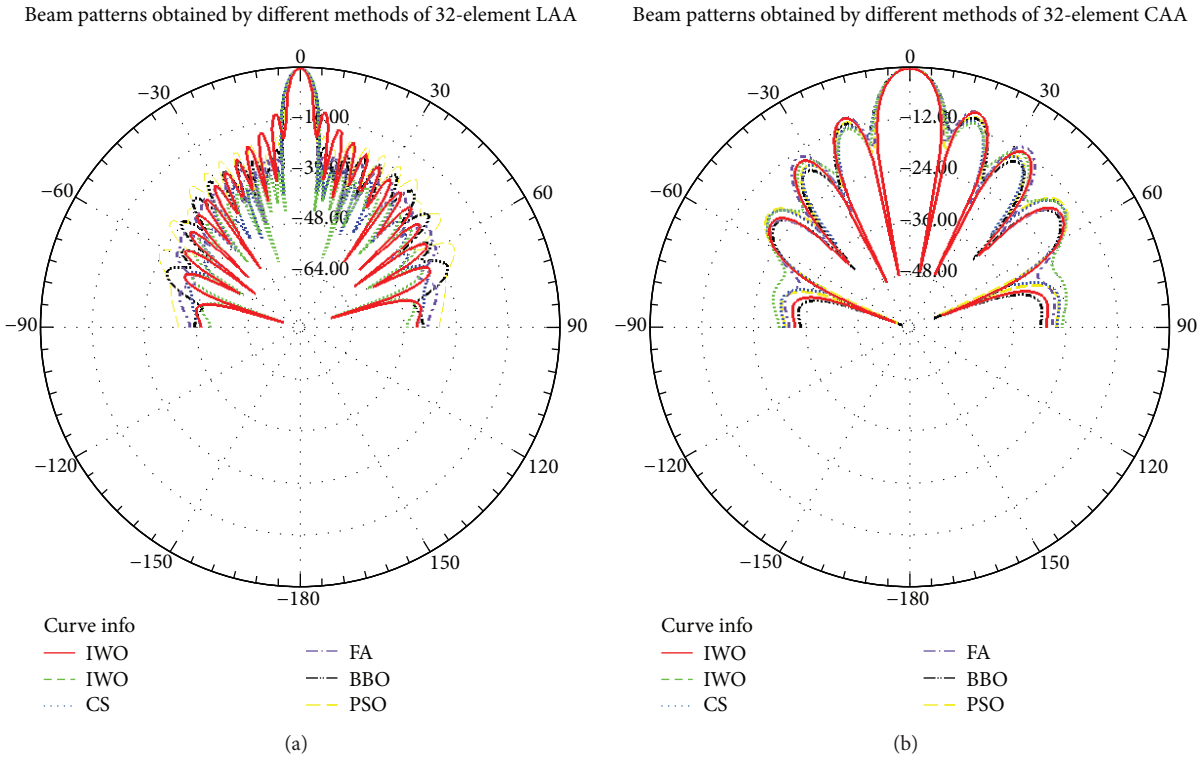


FIGURE 18: 2D beam pattern comparisons in polar coordinates based on different excitation currents obtained by different optimization methods in EM simulations. (a) 32-element LAA. (b) 32-element CAA.

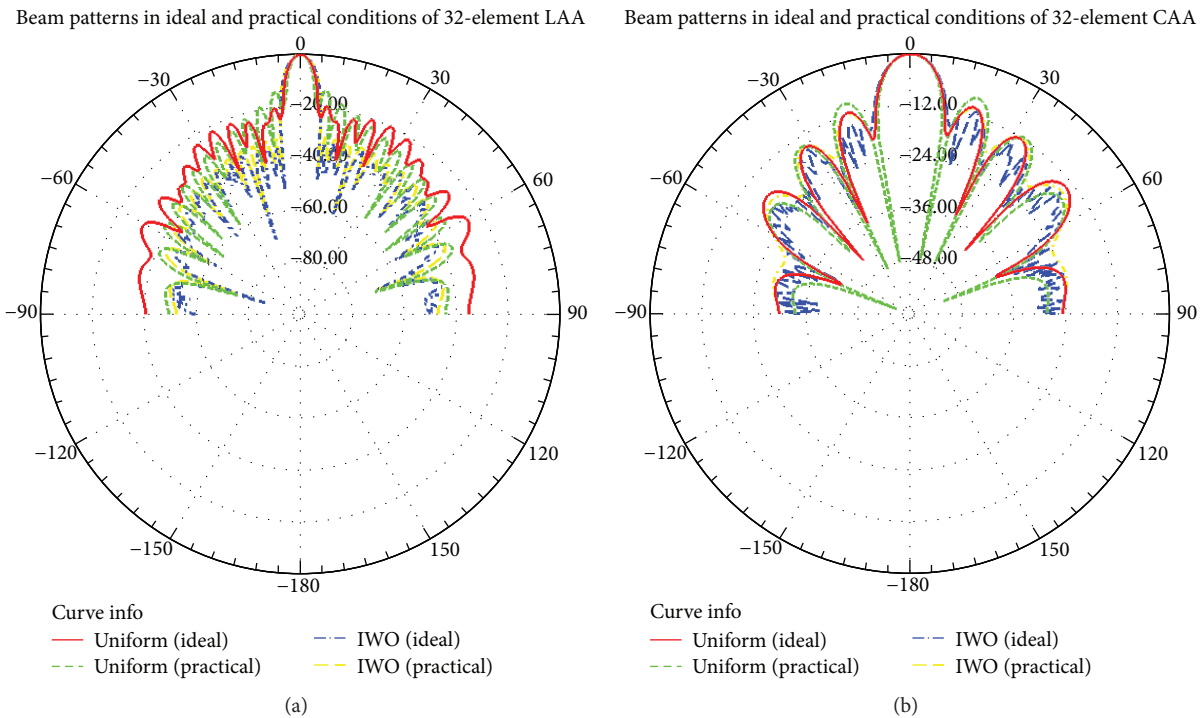


FIGURE 19: Beam patterns obtained by uniform excitation currents and IWO in ideal and practical conditions with EM simulations. (a) 32-element LAA. (b) 32-element CAA.

stability performance of IWO is the best compared with other benchmark algorithms for the sidelobe reductions of both LAA and CAA.

5.5. *EM Simulations.* To verify the beam pattern performances of the antenna arrays obtained by IWO as well as other algorithms in practical conditions, we design the LAAs

(8-element, 16-element, and 32-element) and the CAAs (8-element, 16-element, and 32-element) for EM simulations based on ANSYS Electromagnetics 2016 (HFSS 15.0). First, a physical structure of the array element is designed and we use the element to construct the LAAs and the CAAs. Then, we use the excitation currents obtained by uniform excitations, IWO, CS, FA, BBO, and PSO from Tables 3 to 8 for the LAAs and the CAAs, respectively, to conduct the EM simulations. Figures 16(a) and 16(b) show the beam patterns of the 8-element LAA and CAA with different excitation currents obtained by uniform excitations, IWO, CS, FA, BBO, and PSO, respectively. It can be seen from the figures that all of the optimization algorithms can reduce the maximum SLL compared with the uniform excitation method. However, IWO achieves the lowest maximum SLL among other methods. Figures 17(a) and 17(b) show the beam patterns of the 16-element LAA and CAA obtained by different algorithms. Figures 18(a) and 18(b) show the optimization results of EM simulation for the 32-element LAA and CAA, respectively. As can be seen, similar with cases of the 8-element LAA and CAA, the beam patterns obtained by IWO also have the lowest maximum SLL with a high number of antenna elements. Therefore, IWO has a better performance for reducing the maximum SLLs of the LAAs and the CAAs in practical conditions.

Moreover, to verify the differences of the beam patterns caused by the mutual coupling, we compare the results obtained by the model used for optimization and the EM model. Figures 19(a) and 19(b) show the beam patterns obtained by the uniform excitation currents and by IWO in ideal (the array model used for optimization and simulation) and practical (the array model used for EM simulation) conditions with EM simulations. As can be seen, the beam patterns of the practical condition are distorted compared to the ideal beam patterns. Moreover, the maximum SLLs of practical condition in EM simulation are higher than that in ideal condition obtained by Matlab. Thus, the mutual coupling affects the beam pattern performance. However, the IWO algorithm is still able to provide improvement for reducing the maximum SLL in practical conditions with mutual coupling.

6. Conclusion

In this paper, the IWO algorithm is used to solve the beam pattern synthesis problem of the LAA and the CAA. We formulate an optimization problem for this goal and use IWO as the optimizer to determine a set of optimal excitation currents to achieve the desired beam patterns. Six samples including 8-element, 16-element, and 32-element LAAs and CAAs are conducted to verify the optimization performances of the SLL reductions. Simulation results show that the SLLs can be effectively reduced by IWO. Moreover, compared with other benchmark algorithms, IWO has a better performance in terms of the accuracy, the convergence rate, and the stability. In addition, EM simulation results demonstrate that the optimization results obtained by IWO are also effective for the antenna arrays in practical conditions.

Conflicts of Interest

The authors declare that they have no conflicts of interest.

Acknowledgments

This work was supported by the National Natural Science Foundation of China (Grant no. 61373123), the Chinese Scholarship Council (no. [2016] 3100), and the Graduate Innovation Fund of Jilin University (2017016).

References

- [1] S. Liang, T. Feng, and G. Sun, "Sidelobe-level suppression for linear and circular antenna arrays via the cuckoo search-chicken swarm optimisation algorithm," *IET Microwaves, Antennas & Propagation*, vol. 11, no. 2, pp. 209–218, 2016.
- [2] I. F. Akyildiz, S. Nie, S. C. Lin, and M. Chandrasekaran, "5G roadmap: 10 key enabling technologies," *Computer Networks*, vol. 106, pp. 17–48, 2016.
- [3] D. Z. Zhu, P. L. Werner, and D. H. Werner, "Design and optimization of 3-D frequency-selective surfaces based on a multiobjective lazy ant colony optimization algorithm," *IEEE Transactions on Antennas & Propagation*, vol. 65, no. 12, pp. 7137–7149, 2017.
- [4] G. Sun, Y. Liu, S. Liang, A. Wang, and Y. Zhang, "Beam pattern design of circular antenna array via efficient biogeography-based optimization," *AEU-International Journal of Electronics and Communications*, vol. 79, pp. 275–285, 2017.
- [5] G. Sun, Y. H. Liu, J. Zhang, A. M. Wang, and X. Zhou, "Node selection optimization for collaborative beamforming in wireless sensor networks," *Ad Hoc Networks*, vol. 37, pp. 389–403, 2016.
- [6] G. Sun, Y. H. Liu, A. M. Wang, J. Zhang, X. Zhou, and Z. Liu, "Sidelobe control by node selection algorithm based on virtual linear array for collaborative beamforming in WSNs," *Wireless Personal Communications*, vol. 90, no. 3, pp. 1443–1462, 2016.
- [7] H. Li, Y. Liu, G. Sun, A. Wang, and S. Liang, "Beam pattern synthesis based on improved biogeography-based optimization for reducing sidelobe level," *Computers & Electrical Engineering*, vol. 60, pp. 161–174, 2017.
- [8] S. Jayaprakasam, S. K. A. Rahim, C. Y. Leow, T. O. Ting, and A. Eteng, "Multiobjective beampattern optimization in collaborative beamforming via NSGA-II with selective distance," *IEEE Transactions on Antennas and Propagation*, vol. 65, no. 5, pp. 2348–2357, 2017.
- [9] M. Fakhrazadeh, S. H. Jamali, S. Safavi-Naeini, and P. Mousavi, "A fast calibration algorithm for phased array antennas based on a modified perturbation method," in *2006 IEEE Antennas and Propagation Society International Symposium*, pp. 3343–3346, Albuquerque, NM, USA, July 2006.
- [10] B. K. Lau and Y. H. Leung, "A Dolph-Chebyshev approach to the synthesis of array patterns for uniform circular arrays," in *2000 IEEE International Symposium on Circuits and Systems. Emerging Technologies for the 21st Century. Proceedings (IEEE Cat No.00CH36353)*, vol. 1, pp. 124–127, Geneva, Switzerland, Switzerland, May 2000.
- [11] M. A. Sarker, M. S. Hossain, and M. S. Masud, "Robust beamforming synthesis technique for low side lobe level using taylor excited antenna array," in *2016 2nd International Conference*

- on *Electrical, Computer & Telecommunication Engineering (ICECTE)*, pp. 1–4, Rajshahi, Bangladesh, December 2016.
- [12] S. Todnatee and C. Phongcharoenpanich, "Iterative GA optimization scheme for synthesis of radiation pattern of linear array antenna," *International Journal of Antennas and Propagation*, vol. 2016, Article ID 7087298, 8 pages, 2016.
- [13] V. Chakravarthy and P. M. Rao, "Circular array antenna optimization with scanned and unscanned beams using novel particle swarm optimization," *Indian Journal of Applied Research*, vol. 5, no. 4, 2015.
- [14] G. Ram, D. Mandal, R. Kar, and S. P. Ghoshal, "Pencil beam pattern synthesis of time-modulated concentric circular antenna array using PSO with aging leader and challenger," *Journal of Electromagnetic Waves and Applications*, vol. 29, no. 12, pp. 1610–1629, 2015.
- [15] A. Sharaqa and N. Dib, "Circular antenna array synthesis using firefly algorithm," *International Journal of RF and Microwave Computer-Aided Engineering*, vol. 24, no. 2, pp. 139–146, 2014.
- [16] U. Singh and R. Salgotra, "Synthesis of linear antenna array using flower pollination algorithm," *Neural Computing and Applications*, vol. 29, no. 2, pp. 435–445, 2018.
- [17] P. Saxena and A. Kothari, "Optimal pattern synthesis of linear antenna array using grey wolf optimization algorithm," *International Journal of Antennas and Propagation*, vol. 2016, Article ID 1205970, 11 pages, 2016.
- [18] G. Sun, Y. Liu, Z. Chen, Y. Zhang, A. Wang, and S. Liang, "Thinning of concentric circular antenna arrays using improved discrete cuckoo search algorithm," in *2017 IEEE Wireless Communications and Networking Conference (WCNC)*, pp. 1–6, San Francisco, CA, USA, March 2017.
- [19] G. Sun, Y. Liu, J. Li, Y. Zhang, and A. Wang, "Sidelobe reduction of large-scale antenna array for 5G beamforming via hierarchical cuckoo search," *Electronics Letters*, vol. 53, no. 16, pp. 1158–1160, 2017.
- [20] A. Boldini, C. A. Gonano, F. Grimaccia et al., "Planar array optimization by means of SNO and StudGA," in *IEEE Antennas and Propagation Society International Symposium (APSURSI)*, pp. 1950–1951, Memphis, TN, USA, July 2014.
- [21] P. Saxena and A. Kothari, "Ant lion optimization algorithm to control side lobe level and null depths in linear antenna arrays," *Aeu-International Journal of Electronics and Communications*, vol. 70, no. 9, pp. 1339–1349, 2016.
- [22] S. Jayaprakasam, S. Rahim, and C. Y. Leow, "PSOGSA-explore: a new hybrid metaheuristic approach for beampattern optimization in collaborative beamforming," *Applied Soft Computing*, vol. 30, pp. 229–237, 2015.
- [23] U. Singh, R. Salgotra, and M. Rattan, "A novel binary spider monkey optimization algorithm for thinning of concentric circular antenna arrays," *Iete Journal of Research*, vol. 62, no. 6, pp. 736–744, 2016.
- [24] A. R. Mehrabian and C. Lucas, "A novel numerical optimization algorithm inspired from weed colonization," *Ecological Informatics*, vol. 1, no. 4, pp. 355–366, 2006.
- [25] A. Sharaqa and N. Dib, "Design of linear and elliptical antenna arrays using biogeography based optimization," *Arabian Journal for Science and Engineering*, vol. 39, no. 4, pp. 2929–2939, 2014.
- [26] D. Simon, "Biogeography-based optimization," *IEEE Transactions on Evolutionary Computation*, vol. 12, no. 6, pp. 702–713, 2008.
- [27] X.-S. Yang and S. Deb, "Cuckoo search via Lévy flights," in *2009 World Congress on Nature & Biologically Inspired Computing (NaBIC)*, pp. 210–214, Coimbatore, India, December 2009.
- [28] X.-S. Yang, "Firefly algorithms for multimodal optimization," in *International Symposium on Stochastic Algorithms*, pp. 169–178, Springer, 2009.
- [29] J. Kennedy, "Particle swarm optimization," in *Encyclopedia of Machine Learning*, Springer, 2011.

Research Article

Combination of the Improved Diffraction Nonlocal Boundary Condition and Three-Dimensional Wide-Angle Parabolic Equation Decomposition Model for Predicting Radio Wave Propagation

Ruidong Wang, Guizhen Lu, Rongshu Zhang, and Weizhang Xu

Communication University of China, Beijing 100024, China

Correspondence should be addressed to Ruidong Wang; 123495518@qq.com

Received 14 April 2017; Revised 23 July 2017; Accepted 20 August 2017; Published 28 September 2017

Academic Editor: Sotirios K. Goudos

Copyright © 2017 Ruidong Wang et al. This is an open access article distributed under the Creative Commons Attribution License, which permits unrestricted use, distribution, and reproduction in any medium, provided the original work is properly cited.

Diffraction nonlocal boundary condition (BC) is one kind of the transparent boundary condition which is used in the finite-difference (FD) parabolic equation (PE). The greatest advantage of the diffraction nonlocal boundary condition is that it can absorb the wave completely by using one layer of grid. However, the speed of computation is low because of the time-consuming spatial convolution integrals. To solve this problem, we introduce the recursive convolution (RC) with vector fitting (VF) method to accelerate the computational speed. Through combining the diffraction nonlocal boundary with RC, we achieve the improved diffraction nonlocal BC. Then we propose a wide-angle three-dimensional parabolic equation (WA-3DPE) decomposition algorithm in which the improved diffraction nonlocal BC is applied and we utilize it to predict the wave propagation problems in the complex environment. Numeric computation and measurement results demonstrate the computational accuracy and speed of the WA-3DPE decomposition model with the improved diffraction nonlocal BC.

1. Introduction

Electromagnetic lateral propagation, which includes lateral scattering, lateral diffraction, and the depolarization effect, affects the actual propagation in irregular terrains, especially in situations with steep transverse gradients. In this situation, the two-dimensional (2D) parabolic equation (PE) is no longer accurate. In order to get more accurate results, the three-dimensional parabolic equation (3DPE) is adopted. The 3DPE has two forms of scalar and vector, which comes from the scalar and vector wave equation, respectively. The scalar 3DPE has only one equation that can just reflect the propagation characteristics of an electromagnetic field in a particular component in 3D space. By contrast, vector 3DPE is composed of three equations, which can include all field components, with their boundary conditions. Levy [1] first used scalar 3DPE to calculate the diffraction problem behind urban buildings. Saini and Casiragh [2] studied the 3D split-step Fourier transformation method, in which

a 2D plane Fourier transformation was used, and the plane was perpendicular to the propagation direction. Compared with the 3D finite-difference method, 3D split-step Fourier transformation method decreased computational complexity, but the computational amount was still very large for large-scale computing problems. Zelly and Constantinou [3] established a 3DPE model based on implicit finite-difference method. The implicit finite-difference method can deal with the boundary conditions flexibly; therefore, it is relatively simple to solve the radio wave propagation problem on different terrains. However, due to the large-scale matrix operation, the computation amounts are still very large and the demand for resource is high. In recent years, using 3DPE to predict the radio wave propagation in a small area such as in the urban district environment has become a hot topic and has achieved many results [4–6].

The gradual improvement of the 3D geographic information system in recent years has caused the large-scale 3D electromagnetic propagation prediction to become a trend.

Similar to the case of the 2DPE development, the computational amount of the 3DPE is the main obstacle, especially for radio wave propagation on irregular terrains. The convergence rate depends on the height and lateral width of the computational domain. For large-scale and real-time computation, there still exists a considerable challenge. To accelerate the computational speed of the scalar wide-angle 3DPE (WA-3DPE), we propose a decomposition algorithm. According to this algorithm, the total field at the receiving point is approximately the sum of the straight wave and diffraction wave with the shortest propagation path. In our proposed algorithm, the WA-3DPE can be decomposed into two wide-angle 2DPEs which is called a WA-3DPE decomposition model. The WA-3DPE decomposition model can deal with the horizontal diffraction and vertical diffraction caused by irregular terrain obstructions simultaneously. Furthermore this approximation can largely decrease the computational complexity of the WA-3DPE and can accelerate the speed of computation.

Boundary condition (BC) is critical to the use of PE for accurate prediction of radio wave propagation. The 2DPE prediction of radio wave propagation involves two BCs, which are the upper BC and the lower BC, respectively. For the lower BC, before the 1990s, the smooth and perfect conducting BC was adopted. However, the ideal conducting BC caused large errors in practice. Until 1991, the introduction of hybrid Fourier transform method [7] made it possible to apply impedance BC in the solution PE. For non-PEC surfaces and buildings, the fields on them generally meet the impedance BC. For the upper boundary condition, the most used BCs include window function BC [8], perfect matching layers [9], and transparent BC [10, 11]. For the 3DPE, it contains four BCs. It needs to consider the left and right BCs as well as the upper and lower BCs like the 2DPE. And the most used left and right BCs of 3DPE are the window function BCs [12].

The nonlocal BC is an exact boundary that does not require the additional computational space in the form of absorbing layers. In the previous studies [13], we used the traditional nonlocal boundary conditions in wide-angle two-dimensional parabolic equation model to calculate the propagation loss. However, it has the disadvantage that the 2DPE ignored the lateral scattering and diffraction, and, due to the presence of a spatial convolution integral, the computation is time-consuming. This computation is also memory demanding as it requires the storage and use of all previous values of the field along the boundary. To solve this problem, [14] proposed the recursive convolution (RC) formulation to reduce the computational burden. The RC was achieved using the vector fitting (VF) method. The nonlocal BC combined with RC formulation was applied in a wide-angle 2DPE based on the FD solving method. The computational speed and the accuracy of the nonlocal BC combined with RC formulation were demonstrated. For the actual radio wave propagation problem, the initial source is often fixed at the start position, and there is no need to use the nonlocal BC. Using the simpler diffractive nonlocal BC [15] is enough. Therefore, we adopt the RC formulation to improve the computational speed of the diffraction nonlocal BC. As the diffraction

nonlocal BC is a simplified form of the nonlocal BC, the RC formulation can be applied directly from nonlocal BC to diffraction nonlocal BC. The RC formulation is applicable to the nonlocal BC as well as to the corresponding simpler diffractive nonlocal BC. We call the diffraction nonlocal BC combined with RC as improved diffraction nonlocal BC. We will apply this improved diffraction nonlocal BC in the WA-3DPE decomposition model (described in Section 2).

2. WA-3DPE Decomposition Model

In 3D Cartesian coordinate system, if radio wave propagates along the positive direction of x -axis, the 3DPE [15] can be written as

$$\frac{\partial u(x, y, z)}{\partial x} = -ik_0(1 - \sqrt{1+q})u(x, y, z), \quad (1)$$

where $q = 1/k_0^2(\partial^2/\partial_y^2 + \partial^2/\partial_z^2) + n^2 - 1$, ($k_0 = 2\pi/\lambda$) is the wave number in the free space, and n is the refractive index. Equation (1) corresponds to forward propagating wave.

For numerical implementation, we need a suitable approximation of the q operator. With the help of Padé approximation [15],

$$\sqrt{1+q} \approx \frac{(1+0.75q)}{(1+0.25q)}, \quad (2)$$

a WA-3DPE is obtained.

$$\left\{ \left(1 + \frac{1}{4}(n^2 - 1) \right) \frac{\partial}{\partial x} + \frac{1}{4k_0^2} \frac{\partial}{\partial x} \left(\frac{\partial^2}{\partial y^2} + \frac{\partial^2}{\partial z^2} \right) + \frac{i}{2k_0} \left(\frac{\partial^2}{\partial y^2} + \frac{\partial^2}{\partial z^2} \right) + \frac{i}{2}(n^2 - 1) \right\} u(x, y, z) = 0. \quad (3)$$

Equation (3) is called the Claerbout WA-3DPE, which keeps the propagation angle up to 40 degrees. Although the WA-3DPE can model radio wave propagation in 3D space, the computing efficiency is low because of large-scale matrix operations.

In order to accelerate the WA-3DPE speed of computation, similar to the ray tracing method, the main consideration is given to the straight wave and diffraction wave with the shortest propagation path, which can largely decrease the computational complexity of the WA-3DPE. It is assumed that the 3D function $u(x, y, z)$ can be expressed as the sum of two 2D functions:

$$u(x, y, z) \approx u_h(x, y) + u_v(x, z), \quad (4)$$

where $u_h(x, y)$ is propagation waves in (x, y) plane and $u_v(x, z)$ is propagation waves in (x, z) plane. By applying (4), (3) can be reduced to two 2DPEs:

$$\left\{ \left(1 + \frac{1}{4}(n^2 - 1) \right) \frac{\partial}{\partial x} + \frac{1}{4k_0^2} \frac{\partial^3}{\partial x \partial y^2} + \frac{i}{2k_0} \frac{\partial^2}{\partial y^2} + \frac{ik_0}{2}(n^2 - 1) \right\} u_h(x, y) = 0, \quad (5)$$

$$\left\{ \left(1 + \frac{1}{4} (n^2 - 1) \right) \frac{\partial}{\partial x} + \frac{1}{4k_0^2} \frac{\partial^3}{\partial x \partial z^2} + \frac{i}{2k_0} \frac{\partial^2}{\partial z^2} + \frac{ik_0}{2} (n^2 - 1) \right\} u_v(x, z) = 0. \quad (6)$$

Equations (5) and (6) are called WA-3DPE decomposition model. The WA-3DPE decomposition model actually contains two wide-angle 2DPEs. The total field at the receiving point is the sum of $u_h(x, y)$ and $u_v(x, z)$.

3. Finite-Difference Method of the WA-3DPE Decomposition Model

Since (5) and (6) are symmetrical in form, here we only take (5) as an example to introduce finite-difference implementation, and the finite-difference implementation of (6) can be obtained in the same way. We start by defining the integration grid, which is fixed in the y direction, but not in the x direction, so that it can adapt to the terrain shape. We let $y_{nh} = nh \cdot \Delta y$, $nh = 0, \dots, Nh$ be the grid point at y direction and $x_m = m \cdot \Delta x$, $m = 0, \dots, M, \dots$ be the successive

integration ranges. Using the central difference approximation, the derivatives of (5) are discretized as follows:

$$\varepsilon_m = \frac{x_{m-1} + x_m}{2}, \quad (7)$$

$$u_h(\varepsilon_m, y_{nh}) = \frac{u_h(x_m, y_{nh}) + u_h(x_{m-1}, y_{nh})}{2}. \quad (8)$$

In order to advance the solution from range x_{m-1} to range x_m , (7) and (8) give the midpoint

$$\frac{\partial u_h}{\partial x}(\varepsilon_m, y_{nh}) = \frac{u_h(x_m, y_{nh}) - u_h(x_{m-1}, y_{nh})}{\Delta x}. \quad (9)$$

Equation (9) gives the central finite-difference approximation of the derivative in range

$$\begin{aligned} \frac{\partial^2 u_h}{\partial y^2}(\varepsilon_m, y_{nh}) \\ = \frac{u_h(\varepsilon_m, y_{nh+1}) + u_h(\varepsilon_m, y_{nh-1}) - 2u_h(\varepsilon_m, y_{nh})}{\Delta y^2}. \end{aligned} \quad (10)$$

Equation (10) gives the central finite-difference approximation of the second-order derivative in y :

$$\begin{aligned} \frac{\partial^3 u_h}{\partial x \partial y^2}(x_m, y_{nh}) \\ = \frac{u_h(x_m, y_{nh+1}) + u_h(x_m, y_{nh-1}) - 2u_h(x_m, y_{nh}) - u_h(x_{m-1}, y_{nh+1}) - u_h(x_{m-1}, y_{nh-1}) + 2u_h(x_{m-1}, y_{nh})}{\Delta x \Delta y^2}. \end{aligned} \quad (11)$$

Equation (11) gives the central finite-difference approximation of the third-order mixed derivative.

Substituting (8)–(11) in (5) yields

$$\begin{aligned} \alpha_{h,m} u_{h,nh+1}^m + \beta_{h,m} u_{h,nh}^m + \alpha_{h,m} u_{h,nh-1}^m \\ = \alpha_{h,m-1} u_{h,nh+1}^{m-1} - \beta_{h,m-1} u_{h,nh}^{m-1} - \alpha_{h,m-1} u_{h,nh-1}^{m-1}, \end{aligned} \quad (12)$$

where we have used the following notations:

$$\begin{aligned} \alpha_{h,m} &= \frac{1 + jk_0 \Delta x}{4k_0^2 (\Delta y)^2}, \\ \alpha_{h,m-1} &= \frac{1 - jk_0 \Delta x}{4k_0^2 (\Delta y)^2}, \\ \beta_{h,m} &= 1 + \frac{1}{4} (n^2 (\varepsilon_m, y_{nh}) - 1) (1 + jk_0 \Delta x) \\ &\quad - \frac{1 + jk_0 \Delta x}{2k_0^2 (\Delta y)^2}, \\ \beta_{h,m-1} &= 1 + \frac{1}{4} (n^2 (\varepsilon_m, y_{nh}) - 1) (1 + jk_0 \Delta x) \\ &\quad - \frac{1 - jk_0 \Delta x}{2k_0^2 (\Delta y)^2}. \end{aligned} \quad (13)$$

Equation (12) has expressed values at range x_m as a function of values at range x_{m-1} in the form of a linear system. When $m = 1$, (12) can be written as

$$\begin{aligned} \alpha_{h,1} u_{h,nh+1}^1 + \beta_{h,1} u_{h,nh}^1 + \alpha_{h,1} u_{h,nh-1}^1 \\ = \alpha_{h,0} u_{h,nh+1}^0 - \beta_{h,0} u_{h,nh}^0 - \alpha_{h,0} u_{h,nh-1}^0. \end{aligned} \quad (14)$$

For the Gaussian source,

$$\begin{aligned} u_{h,nh}^0 &= u_h(0, nh \cdot \Delta z) = u_h(0, z) = A \frac{k_0 B}{2\sqrt{2\pi \log 2}} \\ &\quad \cdot \exp(-jk_0 \theta z) \exp\left(-\frac{B^2}{8 \log 2} k_0^2 (z - z_s)^2\right), \end{aligned} \quad (15)$$

where A is a normalization constant; B is half-power beamwidth; θ is elevation angle; and z_s is transmitting antenna height.

The finite-difference implementation of (6) is similar to (5). We let $z_{nv} = nv \cdot \Delta z$, ($nv = 0, \dots, Nv$) be the grid point in z direction and $x_m = m \cdot \Delta x$, ($m = 0, \dots, M, \dots$) be the successive integration ranges. The difference equation of (6) can be written as follows:

$$\begin{aligned} \alpha_{v,m} u_{v,nv+1}^m + \beta_{v,m} u_{v,nv}^m + \alpha_{v,m} u_{v,nv-1}^m \\ = \alpha_{v,m-1} u_{v,nv+1}^{m-1} - \beta_{v,m-1} u_{v,nv}^{m-1} - \alpha_{v,m-1} u_{v,nv-1}^{m-1}, \end{aligned} \quad (16)$$

where we have used the following notations:

$$\begin{aligned}\alpha_{v,m} &= \frac{1 + jk_0 \Delta x}{4k_0^2 (\Delta z)^2}, \\ \alpha_{v,m-1} &= \frac{1 - jk_0 \Delta x}{4k_0^2 (\Delta z)^2}, \\ \beta_{v,m} &= 1 + \frac{1}{4} \left(n^2 (\varepsilon_m, z_{nv}) - 1 \right) (1 + jk_0 \Delta x) \\ &\quad - \frac{1 + jk_0 \Delta x}{2k_0^2 (\Delta z)^2}, \\ \beta_{v,m-1} &= 1 + \frac{1}{4} \left(n^2 (\varepsilon_m, z_{nv}) - 1 \right) (1 + jk_0 \Delta x) \\ &\quad - \frac{1 - jk_0 \Delta x}{2k_0^2 (\Delta z)^2}.\end{aligned}\quad (17)$$

Equation (16) has expressed values at range x_m as a function of values at range x_{m-1} in the form of a linear system. When $m = 1$, the values of $u_{v,nv}^0$ can be obtained by the same way as $u_{h,nh}^0$.

Equations (12) and (16) are the difference equations of the WA-3DPE decomposition model. In order to complete the equation system, we need to include equations at boundaries. For the WA-3DPE decomposition model, it contains 4 boundaries in $\pm y$ and $\pm z$ directions, respectively. Here we employ the 2nd-order accurate discretization of the derivatives $\partial u_h / \partial y$ and $\partial u_v / \partial z$. Thus, at the boundaries,

$$\begin{aligned}\frac{\partial u_h (m\Delta x, y_{\max})}{\partial y} &\approx \frac{3u_{h,0}^m - 4u_{h,1}^m + u_{h,2}^m}{2\Delta y}, \\ \frac{\partial u_h (m\Delta x, y_{\min})}{\partial y} &\approx -\frac{3u_{h,Nh}^m - 4u_{h,Nh-1}^m + u_{h,Nh-2}^m}{2\Delta y}.\end{aligned}\quad (18)$$

Equations (18) give the 2nd-order accurate finite-difference approximation of the boundary conditions at $\pm y$:

$$\begin{aligned}\frac{\partial u_v (m\Delta x, z_{\max})}{\partial z} &\approx \frac{3u_{v,0}^m - 4u_{v,1}^m + u_{v,2}^m}{2\Delta z}, \\ \frac{\partial u_v (m\Delta x, 0)}{\partial z} &\approx -\frac{3u_{v,Nv}^m - 4u_{v,Nv-1}^m + u_{v,Nv-2}^m}{2\Delta z}.\end{aligned}\quad (19)$$

Equations (19) give the 2nd-order accurate finite-difference approximation of the boundary conditions at $\pm z$.

4. The Improved Diffraction Nonlocal BC

4.1. Diffraction Nonlocal BC. In order to use one equation to express the diffraction nonlocal BCs of (x, y) plane and (x, z) plane uniformly, we use “ s ” to represent “ y ” and “ z ”; therefore, for (x, y) plane, $s = y$, and, for (x, z) plane, $s = z$. According to [14, 15], the diffraction nonlocal BC in (x, s) plane can be written as

$$\frac{\partial f (x, s)}{\partial s} = -j\chi^2 k_0 \int_0^x \omega (x - \xi) \frac{\partial f (\xi, s)}{\partial \xi} d\xi, \quad (20)$$

where the convolution kernel ω is given by

$$\omega (x) = J_0 (k_0 x) e^{-jk_0 x}, \quad (21)$$

where $\chi = 1$ for $y = y_{\max}$ and $z = z_{\max}$, $\chi = -1$ for $y = y_{\min}$ and $z = 0$. J_0 is the zero-order Bessel function.

4.2. Recursive Convolution. According to [14], if the function in the convolution term in (20) can be expressed as $A_i \exp(B_i \cdot x)$ then

$$\begin{aligned}R(x) &= \int_0^x \omega (x - \xi) \frac{\partial f (\xi, s)}{\partial \xi} d\xi = R_i (x) \\ &= \int_0^x A_i \exp (B_i (x - \xi)) \frac{\partial f (\xi, s)}{\partial \xi} d\xi \\ &= R_i (m \cdot \Delta x) \\ &= \int_0^{m \cdot \Delta x} A_i \exp (B_i (m \cdot \Delta x - \xi)) \frac{\partial f (\xi, s)}{\partial \xi} d\xi \\ &= R_i^m.\end{aligned}\quad (22)$$

Therefore

$$\begin{aligned}R_i^{m-1} &= R_i [(m-1) \cdot \Delta x] = \int_0^{(m-1) \cdot \Delta x} A_i \\ &\quad \cdot \exp (B_i ((m-1) \cdot \Delta x - \xi)) \frac{\partial f (\xi, s)}{\partial \xi} d\xi.\end{aligned}\quad (23)$$

From (22) and (23), the following recursive formula can be derived:

$$\begin{aligned}R_i^m &= \exp (B_i \cdot \Delta x) R_i^{m-1} \\ &\quad + \int_{(m-1) \cdot \Delta x}^{m \cdot \Delta x} A_i \exp (B_i (m \cdot \Delta x - \xi)) \frac{\partial f (\xi, s)}{\partial \xi} d\xi.\end{aligned}\quad (24)$$

In general, $\omega(x)$ is approximately expressed as

$$\omega (x) \approx \bar{\omega} (x) = \sum_{i=1}^T A_i e^{B_i \cdot x}; \quad (25)$$

thus,

$$\begin{aligned}R(x) &= R^m \approx \sum_{i=1}^T R_i (x) = \sum_{i=1}^T R_i^m \\ &= \sum_{i=1}^T e^{B_i \cdot \Delta x} R_i^{m-1} \\ &\quad + \sum_{i=1}^T A_i e^{B_i \cdot m \Delta x} \int_{(m-1) \cdot \Delta x}^{m \cdot \Delta x} \exp \left(-B_i \cdot \xi \frac{\partial f (\xi, s)}{\partial \xi} \right) d\xi,\end{aligned}\quad (26)$$

where $R_i^0 = 0$.

The integral term in (26) can be discretized as follows:

$$\begin{aligned}
& \int_{(m-1)\Delta x}^{m\Delta x} \exp\left(-B_i \cdot \xi \frac{\partial f(\xi, v)}{\partial \xi}\right) d\xi \\
& \approx \int_{(m-1)\Delta x}^{m\Delta x} \exp\left(-B_i \right. \\
& \cdot \left. \xi \frac{f(m \cdot \Delta x, v) - f((m-1) \cdot \Delta x, v)}{\Delta x}\right) d\xi \\
& = \frac{f(m \cdot \Delta x, v) - f((m-1) \cdot \Delta x, v)}{\Delta x} \\
& \times \int_{(m-1)\Delta x}^{m\Delta x} \exp(-B_i \cdot \xi) d\xi = \exp(-B_i \cdot m\Delta x) \\
& \cdot \left(\frac{f(m \cdot \Delta x, v) - f((m-1) \cdot \Delta x, v)}{\Delta x}\right) \\
& \times \left(\frac{1 - \exp(-B_i \cdot \Delta x)}{-B_i}\right).
\end{aligned} \tag{27}$$

From (26) and (27), it follows that

$$\begin{aligned}
& j\chi^2 k_0 \int_0^x \omega(x - \xi) \frac{\partial f(\xi, s)}{\partial \xi} d\xi \\
& = \tau \chi f^m - \tau \chi f^{m-1} + \chi \Psi_m^f,
\end{aligned} \tag{28}$$

where we have used the following notations:

$$\begin{aligned}
\tau & = 2jk_0 \sum_{i=1}^T A_i \left(\frac{1 - e^{-B_i \Delta x}}{-B_i \cdot \Delta x}\right), \\
\Psi_m^f & = 2jk_0 \sum_{i=1}^T e^{B_i \Delta x} R_i^{m-1}.
\end{aligned} \tag{29}$$

In (28), the integral term in (20) is expressed by recursive convolution method.

4.3. The VF Approximation. As indicated in (25), the function $\omega(x)$ must be curve fitted with a function $\tilde{\omega}(x)$ which is a summation of exponential terms. In $A_i \exp(B_i \cdot x)$, A_i and B_i are complex numbers. To achieve this we use first the VF method [14] to express the function $g(r) = J_0(r)$ as a sum of exponential terms. In the VF method, the Laplace transform of $g(r)$, that is, $G(s)$, is approximated with a sum of fractions $a_i/(s - b_i)$:

$$G(s) = \frac{1}{\sqrt{s^2 + 1}} \approx \sum_{i=1}^T \frac{c_i}{s - d_i}; \tag{30}$$

thus

$$g(r) = J_0(r) \approx \tilde{g}(r) = \sum_{i=1}^T c_i \cdot e^{d_i \cdot r}. \tag{31}$$

Therefore, (21) can be written as

$$\omega(x) = J_0(k_0 x) e^{-jk_0 x} \approx \sum_{i=1}^T c_i \cdot e^{d_i k_0 x} e^{-jk_0 x}. \tag{32}$$

From (25) and (32), it follows that $A_i = c_i$, $B_i = k_0(d_i - j)$. According to [14], $g(r)$ is curve fitted over the argument region $0 \leq r \leq 65000$. It was found that $T = 20$ was sufficient for the computations. The values of c_i and d_i can be found in [14].

5. The WA-3DPE Decomposition Model with the Improved Diffraction Nonlocal BCs

Through formulae (18), (20), and (28), where $s = y$ and $f = u_h$, we can obtain the following expression:

$$u_{h,A}^m = \rho_h u_{h,B}^m + \eta_h u_{h,C}^m + \Xi_{h,A}^m, \tag{33}$$

where we have used the following notations:

$$\begin{aligned}
\rho_h & = \frac{4}{(3 + 2\tau\Delta y)}, \\
\eta_h & = -\frac{1}{(3 + 2\tau\Delta y)},
\end{aligned} \tag{34}$$

$$\Xi_{h,A}^m = \frac{\rho_h \tau \Delta y}{2} (u_{h,A}^{m-1}) - \frac{\rho_h \Delta y}{2} (\Psi_{m,A}),$$

where $A = 0$, $B = 1$, $C = 2$ for $y = y_{\max}$, $A = Nh$, $B = Nh - 1$, $C = Nh - 2$ for $y = y_{\min}$

Through formulae (19), (20), and (28) where $s = z$ and $f = u_v$, we can also obtain the following expression:

$$u_{v,A}^m = \rho_v u_{v,B}^m + \eta_v u_{v,C}^m + \Xi_{v,A}^m, \tag{35}$$

where we have used the following notations:

$$\begin{aligned}
\rho_v & = \frac{4}{(3 + 2\tau\Delta z)}, \\
\eta_v & = -\frac{1}{(3 + 2\tau\Delta z)},
\end{aligned} \tag{36}$$

$$\Xi_{v,A}^m = \frac{\rho_v \tau \Delta z}{2} (u_{v,A}^{m-1}) - \frac{\rho_v \Delta z}{2} (\Psi_{m,A}),$$

where $A = 0$, $B = 1$, $C = 2$ for $z = z_{\max}$, $A = Nv$, $B = Nv - 1$, $C = Nv - 2$ for $z = 0$.

Equations (33) and (35) are the two-dimensional improved diffraction nonlocal BCs in (x, y) plane and (x, z) plane, respectively. As the improved diffraction nonlocal BCs are linear equations, they can be applied in (12) and (16) directly. From (12) and the BC (33), the following global matrix equation is obtained:

$$\Lambda_{h,m} U_{h,m} = \Lambda_{h,m-1} U_{h,m-1} + \Omega_h. \tag{37}$$

From (16) and the BC (35), the following global matrix equation is obtained:

$$\Lambda_{v,m} U_{v,m} = \Lambda_{v,m-1} U_{v,m-1} + \Omega_v. \tag{38}$$

Equations (37) and (38) are the WA-3DPE decomposition model with the improved diffraction nonlocal BCs. The details of the matrices/vectors are given in Appendix.

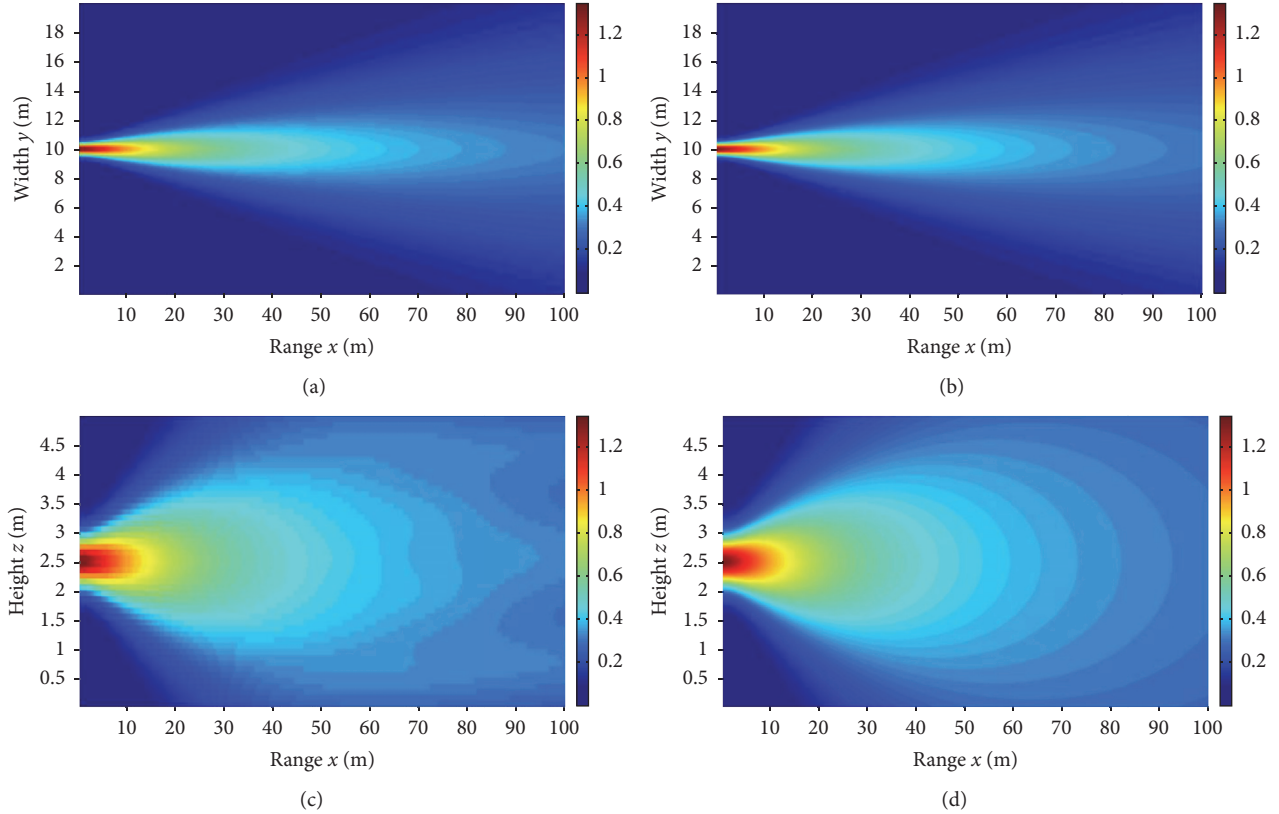


FIGURE 1: Pseudocolor maps of field amplitude. Field amplitude of u_h in (x, y) plane and at $z = 2.5$ m, computed by (a) the standard 3DPE decomposition model with the window function BCs; (b) the WA-3DPE decomposition model with the improved diffraction nonlocal BCs. Field amplitude of u_v in (x, z) plane and at $y = 10$ m, computed by (c) the standard 3DPE decomposition model with the window function BCs; (d) the WA-3DPE decomposition model with the improved diffraction nonlocal BCs.

6. Numerical and Experimental Results

6.1. Free Space Propagation. The biggest advantage of diffraction nonlocal BCs is that it can be used in conjunction with any initial source. In the following computation, we choose Gaussian source [15] as the initial field. We consider radio wave propagation along the positive direction of x -axis in free space, which means that the improved diffraction nonlocal BC can be applied in $\pm y$ and $\pm z$ four boundaries. The sizes of computational region are that $z_{\max} = 5$ m, $z_{\min} = 0$ m, $y_{\max} = 20$ m, $y_{\min} = 0$ m, $x_{\max} = 100$ m, and $x_{\min} = 0$ m. The transmitting antenna is fixed at the point $(x = 0, y = 10, z = 2.5)$. The transmitting antenna frequency is 3 GHz; the 3 dB beamwidth is 5 deg and elevation angle is 0 deg. The refractive index $n = 1$. In order to verify the computational accuracy and efficiency of the WA-3DPE decomposition model with the improved diffraction nonlocal BCs, we choose the computation results of the standard 3DPE decomposition model [16] as a comparison. As it is accurate when the elevation angle is 0 deg, the standard 3DPE decomposition model computation results can be chosen as a comparison. The standard 3DPE decomposition model was solved by the Split-Step Fourier Transform (SSFT) method with the window function BCs. Figures 1(a) and 1(b) are the pseudocolor map of field amplitude of u_h in

(x, y) plane and at $z = 2.5$ m. Figure 1(a) gives the standard 3DPE decomposition model with window function BC computation results and Figure 1(b) shows the WA-3DPE decomposition model with the improved diffraction nonlocal BC computation results. Figures 1(c) and 1(d) are the pseudocolor map of field amplitude of u_v in (x, z) plane and at $y = 10$ m. Figure 1(c) gives the standard 3DPE decomposition model with window function BC computation results and Figure 1(d) shows the WA-3DPE decomposition model with the improved diffraction nonlocal BC computation results.

Table 1 gives some specific parameters involved in the computation of the WA-3DPE decomposition model and the standard 3DPE decomposition model. The computer CPU is the Intel(R) Core(TM) i5-2400 @3.1 GHz. For the standard 3DPE decomposition model solved by SSFT, four window functions are necessary in $\pm y$ and $\pm z$ directions. The window function in the computation is Hanning window function [8]. Theoretically, the greater the thickness of the absorbing layer is, the better the absorbing effect is; but for large-scale radio propagation problems in complex environments, the thickness of the absorbing layer cannot be large enough due to the restriction of computation amount. In our computation, the thickness of the absorbing layer is 20 times larger than the computation area in y and z directions. The size of the actual computation area of the standard 3DPE decomposition

TABLE I: Computation parameters for the WA-3DPE decomposition model and the standard 3DPE decomposition model.

Computation methods	Discretization Size (m)			Actual computation range (m)			Number of steps N/h	N_V	Computation times (s)
	Δx	Δy	Δz	x_{\max}	y_{\max}	z_{\max}			
WA-3DPE decomposition model with the improved diffraction nonlocal BCs	0.5	0.01	0.01	100	20	5	200	500	1.216934
Standard 3DPE decomposition model with widow functions	0.5	0.1	0.1	100	400	100	200	1000	0.191947

TABLE 2: Parameters of knife edge propagation.

Names	Values
Tx antenna height	0.8 cm
Rx antenna height	1 cm
Range	2.5 m
Width	1 m
$d1$	30 cm
$d2$	25 cm
$w1$	84.7 cm
$w2$	89 cm
$h1$	6.5 cm
$h2$	4.9 cm

model in y direction reaches $y_{\max} = 400$ m. It means that the total thickness of the absorbing layer is 380 m and 190 m in the $+y$ and $-y$ direction, respectively. The size of the actual computation area of the standard 3DPE decomposition model in z direction reaches $y_{\max} = 100$ m. It means that the total thickness of the absorbing layer is 95 m and 47.5 m in the $+z$ and $-z$ direction, respectively. It can be seen from Table 1 that the computational speed of the standard 3DPE decomposition model is faster than the WA-3DPE decomposition model. But it is easy to find in Figure 1 that the computational accuracy of the WA-3DPE decomposition model is higher than the standard 3DPE decomposition model. Besides, it can be found that although the discretization size of FD is more restrictive than SSFT, the improved nonlocal BCs can absorb wave completely without increasing extra computation space. For the window function BCs, it is difficult to absorb the wave completely even if the computation space is further increased.

Paper [14] had already investigated the improvement of computation speed brought by RC formulation with VF method, so it does not need to be analyzed again. For the above-mentioned 3D problem, the computing time of Dalrymple and Martin method [14] is 18.9054 s.

6.2. Knife Edge Propagation. To verify the effectiveness of the WA-3DPE decomposition model with the improved diffraction nonlocal BCs, knife edge propagation problems are computed and measured. As depicted in Figure 2, two knife edges are center symmetrically situated on a metal plane. The parameters of their size and location are given in Table 2.

The measurements are made by transmitting a continuous wave signal which are generated by the Agilent Signal Generator. The transmitter output power is 0 dBm. The transmitting antenna for the measurements is a quarter wavelength monopole antenna, and the gain of it is ignored. The Agilent Spectrum Analyzer is used as a receiver with very narrow bandwidth. The receiving antenna is a waveguide antenna, having a gain of 0 dBi and working at the frequencies from 8 GHz to 10 GHz. According to the aforementioned properties of experiment equipment, the working frequency is chosen at 9.375 GHz. Both the transmitting antenna and

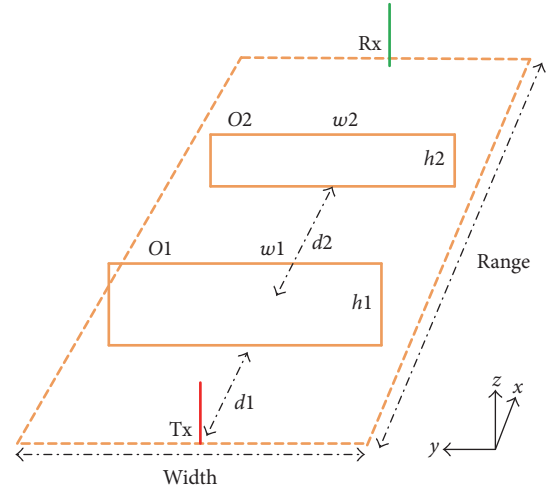


FIGURE 2: Knife edge propagation.

receiving antenna are set on an aluminous plane which is surrounded by wave-absorbing materials to simulate free space propagation environment.

Both of the single knife edge propagation and double knife edges propagation are simulated and measured. In the simulation and experiment of single knife edge propagation, we only keep the knife edge O1 and take the knife edge O2 away. The curves of propagation loss varying with range are given in Figure 3. Figure 3(a) gives the simulation and experiment results of the single knife edge propagation. Then we put on the knife edge O2 and measured again. Figure 3(b) gives the simulation and experiment results of the double knife edges propagation. In order to increase the comparability, we also give the MoM (Method of Moment) and WA-2DPE (wide-angle two-dimensional parabolic equation) computation results in Figure 3. In the simulations, the surface BC is set as PEC, which means the improved diffraction nonlocal BC is applied in up, left, and right boundaries. The results of MoM are obtained by the commercial solver FEKO 7.0.

It can be seen from Figure 3 that the results of the WA-3DPE decomposition model with the improved diffraction nonlocal BCs, MoM, measurement, and WA-2DPE are basically the same no matter for the single knife edge propagation or the double knife edge propagation. However, there exists a big difference in which MoM computation presents fluctuant results while the WA-3DPE decomposition model with the improved diffraction nonlocal BCs and measurement does not. This is because PE only deals with the forward propagation wave, and the signal fluctuation caused by forward propagation and backward propagation interference is not modeled in front of the edges. Theoretically, the measurement should also present fluctuant results in front of the edges, but they are not shown in Figure 3 in that the receiving antenna in our experiment is a waveguide antenna, which can only receive forward propagation waves. The computation results of WA-3DPE are more closer to measurement results than those of WA-2DPE, as the WA-3DPE considers the horizontal diffraction propagation.

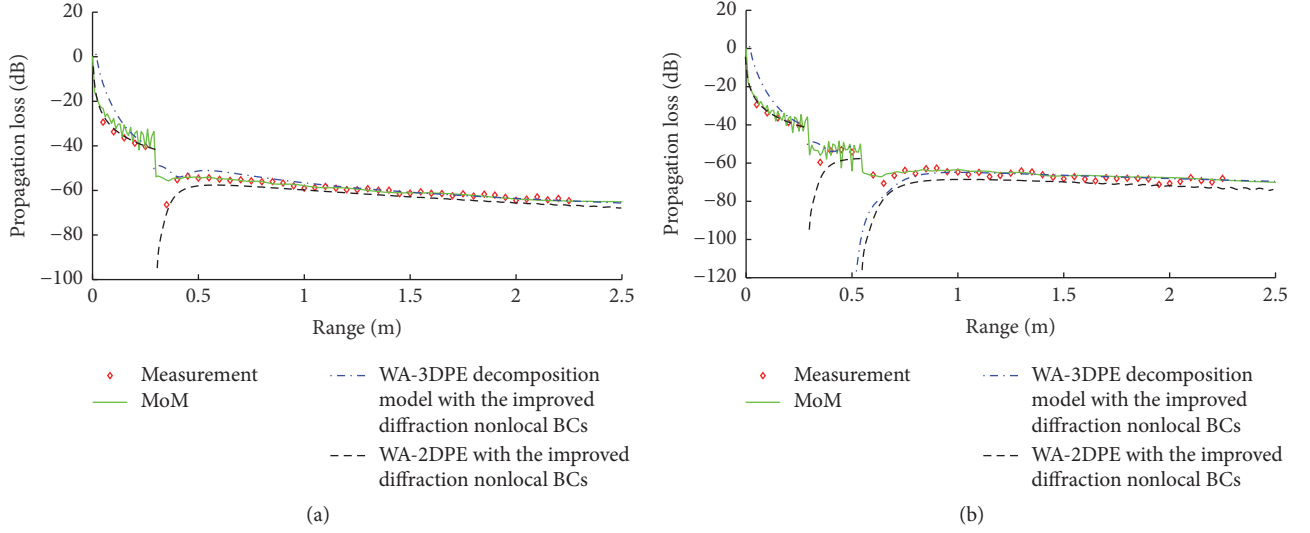


FIGURE 3: Comparison of the results of the WA-3DPE decomposition model with the improved diffraction nonlocal BCs with the measurement, MoM, and WA-2PDE results: (a) propagation loss versus range for single knife edge and (b) propagation loss versus range for double knife edges.

7. Conclusion

In order to accelerate the computational speed, we proposed to apply the RC formulation with VF method in the diffraction nonlocal BC. Furthermore, the improved diffraction nonlocal BC with RCs was applied in the WA-3DPE decomposition model. The computational accuracy and speed of the WA-3DPE decomposition model with diffraction nonlocal BC with RC formulation were demonstrated through the comparison with the standard 3DPE decomposition model, MoM, measurement, and WA-2PDE. The proposed WA-3DPE decomposition model with the improved diffraction nonlocal BC with RC formulation is suitable for the predictions of radio wave propagation in small areas like urban district environments.

Appendix

$$\Lambda_{h,m} = \begin{bmatrix} \beta'_{h,m} & \alpha'_{h,m} & 0 & \cdots & 0 & 0 \\ \alpha_{h,m} & \beta_{h,m} & \alpha_{h,m} & \cdots & 0 & 0 \\ 0 & \alpha_{h,m} & \beta_{h,m} & \alpha_{h,m} & \cdots & 0 \\ \vdots & \vdots & \vdots & \vdots & \vdots & \vdots \\ 0 & \cdots & \alpha_{h,m} & \beta_{h,m} & \alpha_{h,m} & 0 \\ 0 & 0 & \cdots & \alpha_{h,m} & \beta_{h,m} & \alpha_{h,m} \\ 0 & 0 & 0 & \cdots & \alpha'_{h,m} & \beta'_{h,m} \end{bmatrix},$$

$$\beta'_{h,m} = \beta_{h,m} + \rho_h \alpha_{h,m},$$

$$\alpha'_{h,m} = \alpha_{h,m} + \eta_h \alpha_{h,m},$$

$$\Lambda_{h,m-1}$$

$$= \begin{bmatrix} \beta_{h,m-1} & \alpha_{h,m-1} & 0 & \cdots & 0 & 0 \\ \alpha_{h,m-1} & \beta_{h,m-1} & \alpha_{h,m-1} & \cdots & 0 & 0 \\ 0 & \alpha_{h,m-1} & \beta_{h,m-1} & \alpha_{h,m-1} & \cdots & 0 \\ \vdots & \vdots & \vdots & \vdots & \vdots & \vdots \\ 0 & \cdots & \alpha_{h,m-1} & \beta_{h,m-1} & \alpha_{h,m-1} & 0 \\ 0 & 0 & \cdots & \alpha_{h,m-1} & \beta_{h,m-1} & \alpha_{h,m-1} \\ 0 & 0 & 0 & \cdots & \alpha_{h,m-1} & \beta_{h,m-1} \end{bmatrix},$$

$$\Omega_h = \begin{bmatrix} -u_{h,0}^{m-1} \\ \vdots \\ -u_{h,Nh}^{m-1} \end{bmatrix} - \begin{bmatrix} \Xi_{h,0}^m \\ \vdots \\ \Xi_{h,Nh}^m \end{bmatrix},$$

$$U_{h,m} = \begin{bmatrix} u_{h,1}^m \\ \vdots \\ u_{h,Nh-1}^m \end{bmatrix},$$

$$U_{h,m-1} = \begin{bmatrix} u_{h,1}^{m-1} \\ \vdots \\ u_{h,Nh-1}^{m-1} \end{bmatrix},$$

$$\begin{aligned}
\Lambda_{v,m} &= \begin{bmatrix} \beta'_{v,m} & \alpha'_{v,m} & 0 & \cdots & 0 & 0 \\ \alpha_{v,m} & \beta_{v,m} & \alpha_{v,m} & \cdots & 0 & 0 \\ 0 & \alpha_{v,m} & \beta_{v,m} & \alpha_{v,m} & \cdots & 0 \\ \vdots & \vdots & \vdots & \vdots & \vdots & \vdots \\ 0 & \cdots & \alpha_{v,m} & \beta_{v,m} & \alpha_{v,m} & 0 \\ 0 & 0 & \cdots & \alpha_{v,m} & \beta_{v,m} & \alpha_{v,m} \\ 0 & 0 & 0 & \cdots & \alpha'_{v,m} & \beta'_{v,m} \end{bmatrix}, \\
\beta'_{v,m} &= \beta_{v,m} + \rho_v \alpha_{v,m}, \\
\alpha'_{v,m} &= \alpha_{v,m} + \eta_v \alpha_{v,m}, \\
\Lambda_{v,m-1} &= \begin{bmatrix} \beta_{v,m-1} & \alpha_{v,m-1} & 0 & \cdots & 0 & 0 \\ \alpha_{v,m-1} & \beta_{v,m-1} & \alpha_{v,m-1} & \cdots & 0 & 0 \\ 0 & \alpha_{v,m-1} & \beta_{v,m-1} & \alpha_{v,m-1} & \cdots & 0 \\ \vdots & \vdots & \vdots & \vdots & \vdots & \vdots \\ 0 & \cdots & \alpha_{v,m-1} & \beta_{v,m-1} & \alpha_{v,m-1} & 0 \\ 0 & 0 & \cdots & \alpha_{v,m-1} & \beta_{v,m-1} & \alpha_{v,m-1} \\ 0 & 0 & 0 & \cdots & \alpha_{v,m-1} & \beta_{v,m-1} \end{bmatrix}, \\
\Omega_v &= \begin{bmatrix} -u_{v,0}^{m-1} \\ \vdots \\ -u_{v,Nv}^{m-1} \end{bmatrix} - \begin{bmatrix} \Xi_{v,0}^m \\ \vdots \\ \Xi_{v,Nv}^m \end{bmatrix}, \\
U_{v,m} &= \begin{bmatrix} u_{v,1}^m \\ \vdots \\ u_{v,Nv-1}^m \end{bmatrix}, \\
U_{v,m-1} &= \begin{bmatrix} u_{v,1}^{m-1} \\ \vdots \\ u_{v,Nv-1}^{m-1} \end{bmatrix}.
\end{aligned} \tag{A.1}$$

Conflicts of Interest

The authors declare that there are no conflicts of interest regarding the publication of this paper.

Acknowledgments

This work was supported by National Key Technology Support Program 2015BAK05B01: research on a new generation news-gathering system based on ultrahigh speed WLAN and BD-2.

References

[1] M. F. Levy, "Parabolic equation modelling of propagation over irregular terrain," *Electronics Letters*, vol. 26, no. 15, pp. 1153–1155, 1990.

[2] L. Saini and U. Casiragh, "A 3D Fourier split-step technique for modelling microwave propagation in urban areas," in *Proceedings of European Conference on Radio Relay Systems IET*, pp. 210–214, 2002.

[3] C. A. Zelly and C. C. Constantinou, "A three-dimensional parabolic equation applied to VHF/UHF propagation over irregular terrain," *IEEE Transactions on Antennas and Propagation*, vol. 47, no. 10, pp. 1586–1596, 1999.

[4] M. F. Levy, "Diffraction studies in urban environment with wide-angle parabolic equation method," *Electronics Letters*, vol. 28, no. 16, pp. 1491–1492, 1992.

[5] A. A. Zaporozhets and M. F. Levy, "Modelling of radiowave propagation in urban environment with parabolic equation method," *Electronics Letters*, vol. 32, no. 17, pp. 1615–1616, 1996.

[6] R. Janaswamy and J. B. Andersen, "Path loss predictions in urban areas sprawling over irregular terrain," in *Proceedings of the 1998 9th IEEE International Symposium on Personal, Indoor and Mobile Radio Communications, PIMRC. Part 3 (of 3)*, pp. 874–878, September 1998.

[7] J. R. Kuttler and G. D. Dockery, "Theoretical description of the parabolic approximation/Fourier split-step method of representing electromagnetic propagation in the troposphere," *Radio Science*, vol. 26, no. 2, pp. 381–393, 1991.

[8] P. Zhang, L. Bai, Z. Wu, and F. Li, "Effect of window function on absorbing layers top boundary in parabolic equation," in *Proceedings of the 3rd Asia-Pacific Conference on Antennas and Propagation, APCAP 2014*, pp. 849–852, chn, July 2014.

[9] J.-P. Berenger, "A perfectly matched layer for the absorption of electromagnetic waves," *Journal of Computational Physics*, vol. 114, no. 2, pp. 185–200, 1994.

[10] M. Ehrhardt and A. Zisowsky, "Discrete non-local boundary conditions for split-step Padé approximations of the one-way Helmholtz equation," *Journal of Computational and Applied Mathematics*, vol. 200, no. 2, pp. 471–490, 2007.

[11] G. H. Song, "Transparent boundary conditions for beam-propagation analysis from the green's function method," *Journal of the Optical Society of America A: Optics and Image Science, and Vision*, vol. 10, no. 5, pp. 896–904, 1993.

[12] P. Zhang, L. Bai, Z. Wu, and L. Guo, "Applying the Parabolic Equation to Tropospheric Groundwave Propagation: A review of recent achievements and significant milestones," *IEEE Antennas and Propagation Magazine*, vol. 58, no. 3, pp. 31–44, 2016.

[13] Z. Ge, G. Lu, and R. Wang, "Using the finite difference parabolic equation with nonlocal boundary condition for complex environment radiowave propagation prediction," in *Proceedings of the 11th International Symposium on Antennas, Propagation and EM Theory, ISAPE 2016*, pp. 478–480, chn, October 2016.

[14] C. Mias, "Fast computation of the nonlocal boundary condition in finite difference parabolic equation radiowave propagation simulations," *Institute of Electrical and Electronics Engineers. Transactions on Antennas and Propagation*, vol. 56, no. 6, pp. 1699–1705, 2008.

[15] M. F. Levy, *Parabolic Equation Methods for Electromagnetic Wave Propagation*, vol. 45, The Institution of Electrical Engineers, London, UK, 1st edition, 2000.

[16] G. Lu, R. Wang, Z. Cao, and K. Jiang, "A decomposition method for computing radiowave propagation loss using three-dimensional parabolic equation," *Progress In Electromagnetics Research M*, vol. 44, pp. 183–189, 2015.

Research Article

Application of Genetic Algorithm to Estimation of Function Parameters in Lightning Currents Approximations

V. Javor,¹ K. Lundengård,² M. Rančić,² and S. Silvestrov²

¹Faculty of Electronic Engineering, University of Niš, A. Medvedeva 14, 18000 Niš, Serbia

²Division of Applied Mathematics, UKK, Mälardalen University, Västerås, Sweden

Correspondence should be addressed to V. Javor; vesna.javor@elfak.ni.ac.rs

Received 23 May 2017; Revised 19 June 2017; Accepted 20 June 2017; Published 27 August 2017

Academic Editor: Christos Kalialakis

Copyright © 2017 V. Javor et al. This is an open access article distributed under the Creative Commons Attribution License, which permits unrestricted use, distribution, and reproduction in any medium, provided the original work is properly cited.

Genetic algorithm (GA) is applied for the estimation of two-peaked analytically extended function (2P-AEF) parameters in this paper. 2P-AEF is used for approximation of measured and typical lightning discharge currents. Lightning discharge channel is often modeled as thin-wire vertical antenna at perfectly conducting ground. Engineering lightning stroke models assume that the current along that channel is related to the channel-base current which may be measured at the instrumented tall towers and in triggered lightning experiments. Mathematical modeling of lightning currents is important in verification of lightning strokes models based on simultaneously measured electromagnetic fields at various distances, so as in lightning protection studies, computation of lightning induced effects and simulation of overvoltages in power systems. Typical lightning discharge currents of the first positive, first negative, and subsequent negative strokes are defined by IEC 62305 Standard based on comprehensive measurements. Parameters of 2P-AEF's approximation of the typical negative first stroke current are determined by GA and compared to approximations obtained by other functions. Measured currents at Monte San Salvatore in Switzerland, at Morro de Cachimbo Station in Brazil, and in rocket-triggered lightning experiments at Camp Blanding in Florida are approximated by 2P-AEFs, and good agreement with experimentally measured waveshapes is obtained.

1. Introduction

Besides cloud-to-ground lightning discharges, intracloud and discharges between thunderclouds, there are also great transient luminous events above troposphere, such as blue jets, gigantic jets, red sprites, elves, and halos. A small percentage of powerful thunderstorms, mostly with positive cloud-to-ground flashes and lightning discharge currents of the order of hundreds of kA, trigger such phenomena at tens of kilometers above thunderclouds. However, the majority of cloud-to-ground lightning discharges (about 90%) transfer negative charges from thunderclouds to the ground. Typical waveshapes of the first positive, first negative, and subsequent negative strokes currents are obtained from comprehensive measurements of Berger et al. [1, 2] and Lin et al. [3] and measurements at tall instrumented towers [4] and in rocket-triggered lightning experiments [5, 6]. These currents, so as some estimated parameters of lightning discharges, are often used in modeling of lightning strokes, in research and

lightning protection studies [2, 7], and in the IEC 62305 Standard [8]. Engineering models [9] assume that the current pulse propagates with distortion and attenuation along the channel between the ground and the center of charges in thunderclouds. Spatial and temporal current distribution (or charge-density distribution) along the channel radiates lightning electromagnetic field over the conducting ground. Based on lightning strokes parameters (measured channel-base currents and their derivatives, estimated speed of propagating front, and return stroke speed evaluated from the channel luminosity), model-predicted electromagnetic field results are compared to the measured data at various distances from the channel in order to validate such models. Electromagnetic models assume that the lightning channel is a lossy thin-wire monopole antenna at perfectly conducting ground. Current distribution along the channel is determined by solving Maxwell's equations, for the satisfied boundary conditions, and afterwards, electric and magnetic fields are computed and compared to the measured ones. The influence of finite

ground conductivity may be also taken into account in these models. Approximation of various channel-base currents waveshapes by analytical functions is very important, so as evaluation of their parameters.

There are many possible applications of evolutionary algorithms in lightning research and modeling of lightning strokes. Particle Swarm Optimization (PSO) is used for evaluation of lightning return stroke models' parameters (return stroke speed, channel height, and the constant of exponential current attenuation factor), based on electromagnetic theory relations and measured magnetic flux density in [10], whereas remote electric fields are used for estimation of lightning current waveforms and return stroke velocity profiles in [11, 12]. Genetic algorithm (GA) is proposed in [13] and Powell algorithm combined with PSO in [14] for identifying channel-base current parameters in the sum of two Heidler's functions [15], but only for single-peaked waveshapes of typical negative subsequent strokes. GA is also used for evaluation of parameters in the same function based on measured triggered lightning currents, and for the estimation of reflection coefficients [16] based on lightning discharge currents measured at tall instrumented towers, but also for the single-peaked channel-base current. An inversion method based on time series neural network and back-propagation neural network is presented in [17].

Approximation of negative first stroke currents is more difficult than of negative subsequent stroke currents, due to multiple peaks in waveshapes. For approximations of such waveshapes, linear combinations of a few functions from literature are usually used, as double-exponential function [18], Pulse function [19], Heidler's function, and others. A sum of seven Heidler's functions is used in [20] to approximate first negative strokes currents as measured in Brazil [21]. Such waveshapes are approximated, for example, in order to calculate overvoltages induced in transmission lines [22]. There are in total 28 parameters needed for that sum. Two-peaked analytically extended function (2P-AEF) uses just 7 parameters for the same waveshape [23]. The accuracy is estimated in [20] from the current's peaks values obtained by the sum of seven Heidler's functions, whereas in the case of 2P-AEF, these peaks are chosen as exact values at the corresponding time moments. Besides, N -peaked AEF is a linear combination itself, so its number of peaks and parameters determine the accuracy of the obtained approximation. It is suitable for a variety of multip peaked waveshapes.

Application of GA to estimation of 2P-AEF parameters is presented in this paper. This function is based on the new channel-base current function [24], used to approximate the IEC 62305 Standard currents and other typical lightning currents [25]. Marquardt least squares method is used for estimation of its parameters in [26]. In this paper, 2P-AEF parameters are obtained by GA and given for an assumed negative first stroke current [27], but also for the measured currents waveshapes at Monte San Salvatore in Switzerland [1] and at Morro de Cachimbo Station in Brazil [21]. Parameters of 2P-AEF are determined also for the typical first negative stroke current [1] and compared to results obtained by other functions. Triggered lightning current waveshape measured

in artificially induced lightning discharge [28] is also approximated by 2P-AEF and its parameters are optimized by GA. 2P-AEF is described in Section 2 and application of GA to estimation of its parameters for the assumed two-peaked current waveshape in Section 3. Measured negative stroke currents are approximated in Section 4, the typical negative stroke current in Section 5, and triggered lightning current in Section 6. In order to validate the results of the obtained approximations, Feature Selective Validation (FSV) method [29, 30] is applied in this paper, adopted by the IEEE Standard 1597.1 [31] for validation of computational electromagnetics results, computer modeling, and simulations. GA proved to have better results than least squares method used for the Two-rise function (TRF) [23].

2. Two-Peaked Analytically Extended Function

Analytical functions used for approximation of lightning currents with satisfying accuracy usually have a few parameters to be determined. The simplest function for representing pulse waveshapes is double-exponential (DEXP) function [18]. First derivative of this function at $t = 0$ is not of zero value, as in realistic cases, which results in certain difficulties in lightning electromagnetic field computation. Its convex waveshape from zero to the maximum value is also not suitable for representing realistic lightning currents.

Heidler's function [15] has a concave rising part of the waveshape and first derivative of zero value at $t = 0$. It is given by

$$i(t) = \frac{I_0}{\eta} \frac{(t/\tau_1)^n}{(t/\tau_1)^n + 1} \exp\left(-\frac{t}{\tau_2}\right), \quad (1)$$

for the current I_0 , time constants τ_1 and τ_2 , degree n (usually chosen from 2 to 10), and the current peak correction factor $\eta = \exp[-(\tau_1/\tau_2)(n\tau_2/\tau_1)^{1/n}]$. It is often used in the literature and adopted in the IEC 62305 Standard [8] for representation of typical lightning currents. A sum of two Heidler's functions is used for approximation of single-peaked lightning currents, as suggested in [32], and used in [10–14]. For the measured negative first stroke currents, a sum of seven Heidler's functions is needed [20].

Linear combination of Heidler's function (for $n = 2$) and DEXP function is used in [33] for the negative subsequent stroke current and given by

$$i(t) = \frac{I_{01}}{\eta} \frac{(t/\tau_1)^2}{(t/\tau_1)^2 + 1} \exp\left(-\frac{t}{\tau_2}\right) + I_{02} \left[\exp\left(-\frac{t}{\tau_3}\right) - \exp\left(-\frac{t}{\tau_4}\right) \right]. \quad (2)$$

In order to approximate waveshapes with two distinct rise portions, a combination of power and exponential functions from [34] is simplified in [27], so the following form is

obtained:

$$i(t) = \frac{I_0}{\eta} [(1-c)X(t) + cY(t)] \exp\left(-\frac{t}{\tau}\right), \quad (3)$$

for $Y(t) = [a(t/T)^k + (t/T)^{n_1}]/[1 + (t/T)^{n_1}]$, $X(t) = (bt/T)^{n_2}/[1 + (bt/T)^{n_2}]$, parameters a, b, c, T, k, n_1, n_2 , current I_0 , and peak correction factor η .

Pulse function [19] is given by the following expression:

$$i(t) = \frac{I_0}{\xi} \left[1 - \exp\left(-\frac{t}{\tau_1}\right)\right]^n \exp\left(-\frac{t}{\tau_2}\right), \quad (4)$$

for the current I_0 , time constants τ_1 and τ_2 , degree n , and the current peak correction factor $\xi = [n\tau_2/(\tau_1 + n\tau_2)]^n [\tau_1/(\tau_1 + n\tau_2)]^{\tau_1/\tau_2}$.

2P-AEF is given by the following expression:

$$i(t) = \begin{cases} I_{m1} \sum_{i=1}^{k_1} b_{1i} \left[\frac{t}{t_{m1}} \exp\left(1 - \frac{t}{t_{m1}}\right) \right]^{a_{1i}}, & 0 \leq t \leq t_{m1}, \\ I_{m1} + I_{m2} \sum_{i=1}^{k_2} b_{2i} \left[\frac{t - t_{m1}}{t_{m2} - t_{m1}} \exp\left(1 - \frac{t - t_{m1}}{t_{m2} - t_{m1}}\right) \right]^{a_{2i}}, & t_{m1} \leq t \leq t_{m2}, \\ (I_{m1} + I_{m2}) \sum_{i=1}^{k_3} b_{3i} \left[\frac{t}{t_{m2}} \exp\left(1 - \frac{t}{t_{m2}}\right) \right]^{a_{3i}}, & t_{m2} \leq t < \infty, \end{cases} \quad (5)$$

for the first peak I_{m1} at t_{m1} and the second peak $I_{m1} + I_{m2}$ at t_{m2} . There are $2k_1$ parameters to be determined (a_{1i} and b_{1i} , for $i = 1, \dots, k_1$) for the first interval (from zero to the first peak), $2k_2$ parameters (a_{2i} and b_{2i} , for $i = 1, \dots, k_2$) for the second interval (from the first to the second peak), and $2k_3$ parameters (a_{3i} and b_{3i} , for $i = 1, \dots, k_3$) for the last interval (after the second peak). The following three relations are valid:

$$\sum_{i=1}^{k_n} b_{ni} = 1, \quad n = 1, 2, 3, \quad (6)$$

which results in $K = 2(k_1 + k_2 + k_3) - 3$ unknown parameters to be determined for 2P-AEF(k_1, k_2, k_3). For the two-peaked waveshapes, satisfying accuracy is obtained by 2P-AEF(2,1,2), for $k_1 = 2, k_2 = 1, k_3 = 2$, and just $K = 7$ unknown parameters to be estimated by GA. Greater k_i increase the accuracy in i -th interval, at the expense of increased number of parameters to be determined.

Different techniques may be employed for evaluation of these functions parameters. Among procedures based on least squares fitting are nonlinear curve fitting method (NLCF) [19] applied to Pulse function parameters and Marquardt least squares method [35] applied to DEXP [36], Heidler's function [37–39], Pulse function [39], and NP-AEFs [26]. GA is applied in this paper for evaluation of 2P-AEF's parameters for the typical and measured waveshapes of negative first strokes.

3. Application of GA to Estimation of 2P-AEF's Parameters

GA is an evolutionary algorithm which has been applied for a few decades already [40] to a great variety of problems in different domains. A problem plays the role of an environment with an initial population of individuals generated at random or heuristically. An individual represents a possible

solution to the problem with a certain degree of adaptation to its environment. Biological principle of natural evolution is used for artificial selection based on the computed fitness function. The candidate solution is encoded in its "genome" and new genetic material is introduced in each generation as in natural evolutionary mechanisms. Like in nature, better solutions to the problem are obtained, and GA is possibly leading to the optimal ones. One of the possible applications is curve fitting [41].

GA is applied in this paper with a goal to optimize 2P-AEFs parameters, so that the resulting waveforms well approximate measured and typical negative first stroke currents. Fitness function ff is the L -infinity norm described as

$$ff = \max_i |I_{gi} - I_{AEFi}|, \quad (7)$$

for steps $i = 1, \dots, N$, whereas I_{gi} are function's goal values and I_{AEFi} values obtained by 2P-AEF. The goal values may be obtained either by measurements or by using another reference current function already validated as an appropriate one for representing the recorded data. For the following examples, GA parameters setting is given in Table 1. Number of randomly created individuals that populate the initial generation, that is, the population size parameter, is set to 100 in all the examples. Based on calculated fitness values, parents are being chosen. Subsequent generations are created through crossover and mutation processes which are defined by the crossover fraction parameter (the fraction of individuals in the next generation that are created by crossover) and the number of elite individuals (certain number of most fit individuals in the current population that automatically survive to the next generation). The stopping criterion is the number of generations, that is, maximum number of iterations after which the procedure is stopped. In order to assist GA, upper and lower bounds (UB-upper bound; LB-lower bound) for each parameter being optimized are defined. These search regions are given in Table 2. It should

TABLE 1: Parameter settings for the genetic algorithm.

Parameter	Value
Population size	100
Number of generations	150
Number of elite individuals	2
Crossover fraction	0.8, which equals 78 individuals
Individuals created by mutation	20

TABLE 2: Search regions of the genome variables.

	Example 1		Example 2		Example 3		Example 4	
	LB	UB	LB	UB	LB	UB	LB	UB
b_{11}	0.2	0.8	0.2	0.8	0.2	0.3	0.05	1.2
a_{11}	1.5	3	1.5	3	1.5	6	1.5	10
a_{12}	5	90	5	60	10	45	10	45
a_{21}	4.5	15	5	20	10	30	0.1	1.1
b_{31}	0.35	0.45	0.35	0.6	0.2	0.9	0.3	0.9
a_{31}	1.5	2.5	2.5	4	0.005	0.04	0.001	0.01
a_{32}	0.02	0.08	0.02	0.06	0.2	1.3	2	5

be noticed that for 2P-AEF(2,1,2) no bounds are needed for b_{12} , b_{21} , and b_{32} , as these are not unknowns, but determined from (6) as $b_{12} = 1 - b_{11}$, $b_{21} = 1$, and $b_{32} = 1 - b_{31}$.

An assumed two-peaked waveshape [27], based on (3), is given in Figure 1. It is chosen to be approximated by 2P-AEF(2,1,2), for the first peak $I_{m1} = 16.5$ kA at $t_{m1} = 3.3 \mu\text{s}$ and the second peak $I_{m1} + I_{m2} = 30$ kA at $t_{m2} = 4.6 \mu\text{s}$. In order to do so, lower and upper bounds of all parameters being optimized are given in Table 3. Values of 2P-AEF parameters obtained by GA are denoted by GA 2P-AEF, whereas results obtained by least squares method for TRF [23] are denoted by LS TRF in Table 3. Parameters values [27] corresponding to the function given by (3) are also shown in Table 3. These three current functions are presented in Figure 2. Amplitude Difference Measure (ADM) obtained by 1D FSV Tool [42], which is applied to the assumed current from [27] and its approximation by 2P-AEF(2,1,2) using GA, shows the quality of this approximation. The corresponding Grade-Spread chart is presented in Figure 3. Grade and Spread values obtained by 1D FSV Tool may range from 1 (best quality) to 6 (worst quality). ADMc is probability density function showing the proportion of point-by-point analysis in Figure 4(a) in order to check the measure of approximation's confidence. ADMi is showing point-by-point comparison of the amplitude differences in Figure 4(b).

In the x -axis shown in Figure 4(a), EX stands for excellent, VG for very good, G for good, F for fair, P for poor, and VP for very poor approximated data. The EX score (for 92.5%) and VG score (for 7.5%) of this approximation are confirmed by 1D FSV Tool. For smaller values of Grade (rated from 1 to 6), the quality of approximation is better, and for smaller values of Spread (rated from 1 to 6), the reliability of results

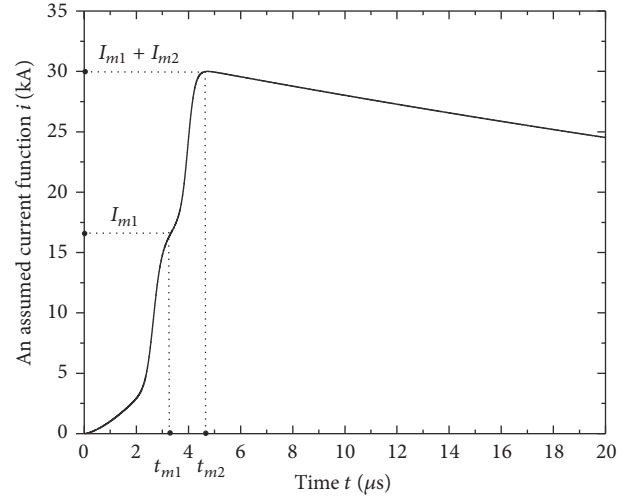


FIGURE 1: An assumed two-peaked current waveshape from [27] given by (3).

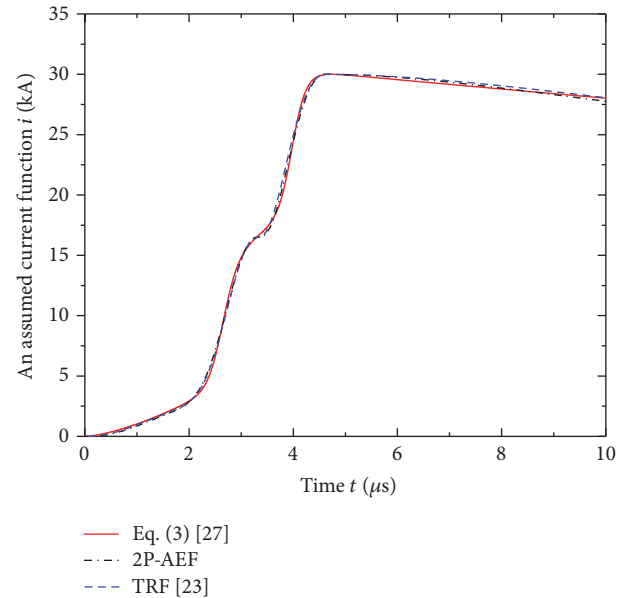


FIGURE 2: An assumed two-peaked current waveshape [27], TRF [23], and 2P-AEF(2,1,2).

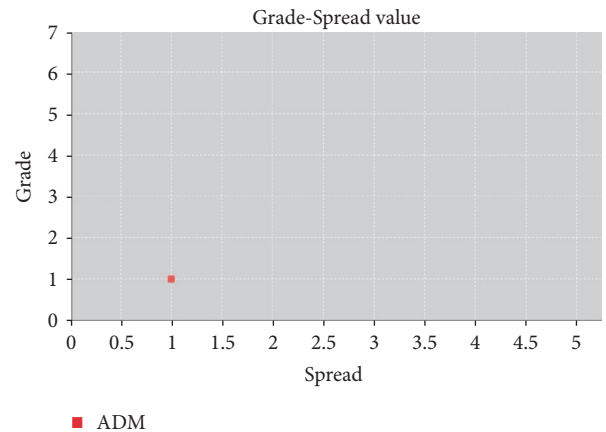


FIGURE 3: Grade-Spread value obtained by FSV applied to the assumed current [27] and its approximation by 2P-AEF(2,1,2) using GA for parameters evaluation.

TABLE 3: Upper and lower bounds of the genome variables and parameters values for 2P-AEF, TRF, and current function (3).

	GA bounds		GA 2P-AEF	LS TRF [23]	Equation (3) [27]	
	LB	UB				
b_{11}	0.2	0.5	0.2000	0.2	I_{\max} [kA]	30
b_{12}	/	/	0.8000	0.8	η	0.937
a_{11}	1.5	2.7	2.7000	2.5	n_1	30
a_{12}	30	45	33.287	35	n_2	18
b_{21}	/	/	1	1	k	1.5
a_{21}	3.4	5	3.4029	3	T [μ s]	4
b_{31}	0.5	0.9	0.8491	0.75	τ [μ s]	75
b_{32}	/	/	0.1509	0.25	a	0.4
a_{31}	0.02	0.06	0.0579	0.04	b	1.5
a_{32}	0.6	1.2	1.1513	0.6	c	0.65

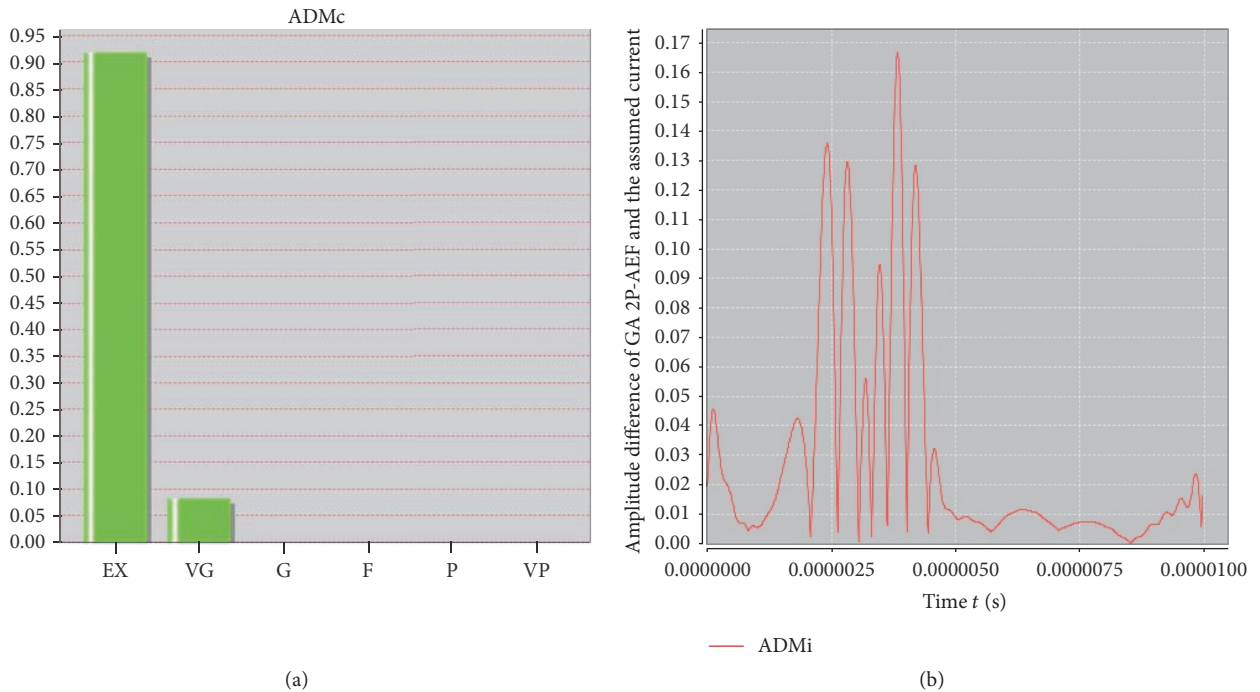


FIGURE 4: (a) ADMc and (b) ADMi obtained by FSV applied to the assumed current from [27] and its approximation by 2P-AEF(2,1,2) using GA for parameters evaluation.

is higher. Results obtained by 1D FSV Tool for GA 2P-AEF approximation are Grade value 1 and Spread value 1 (Figure 3) for the threshold set at 85% by default. These two values (1,1) stand for the best quality of approximation.

The first derivative of the current (3) for the assumed waveshape [27], TRF's derivative, and 2P-AEF's derivative for parameters obtained by GA are given in Figure 5.

4. Approximation of the Measured Negative First Stroke Currents by 2P-AEF

Previously described GA procedure is employed for optimizing 2P-AEFs parameters in order to approximate the measured negative first stroke currents. For all the examples,

GA uses exact values for the current peaks and corresponding time moments as the input data (peaks are I_{m1} at t_{m1} and $I_{m1} + I_{m2}$ at t_{m2}). As the first example, two-peaked waveshape of the negative first stroke current measured at Monte San Salvatore [1] is approximated by 2P-AEF(2,1,2) with 7 parameters estimated by GA. Parameters values for Example 1 are given in Table 4. Waveshape of the measured current denoted by MSS-FST#2peaks in [20], approximated by the sum of seven Heidler's functions (1), is the goal function for GA. Parameters of TRF are obtained by the least squares method [23] and denoted by LS TRF in Table 4.

Results of these approximations are given in Figure 6 in 100 μ s, and first derivatives of these currents are given in Figure 7 in 20 μ s.

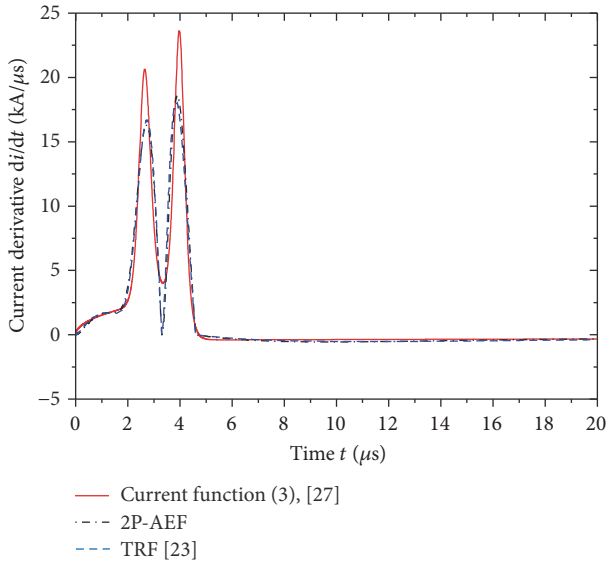


FIGURE 5: Derivatives of the assumed current waveshape [27], TRF [23], and 2P-AEF(2,1,2).

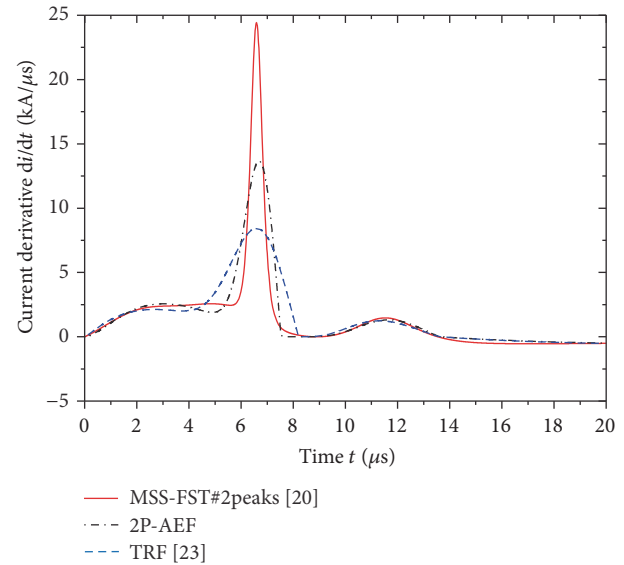


FIGURE 7: Derivatives of MSS-FST#2peaks [20], TRF [23], and 2P-AEF(2,1,2).

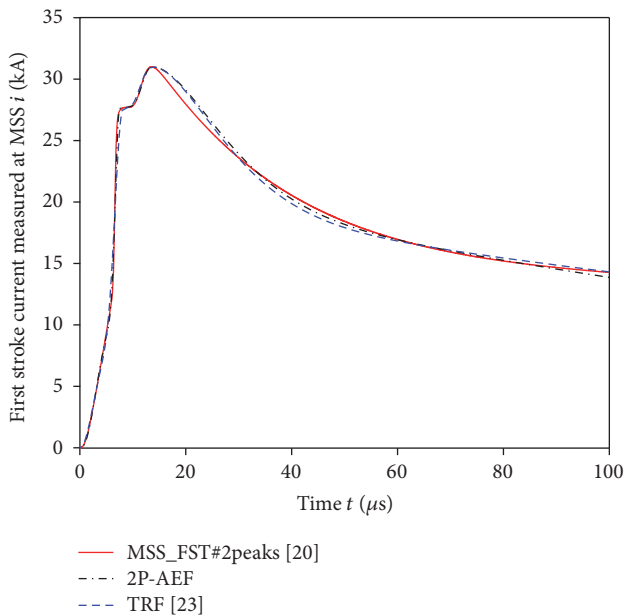


FIGURE 6: Measured current MSS_FST#2peaks [20], TRF [23], and 2P-AEF(2,1,2).

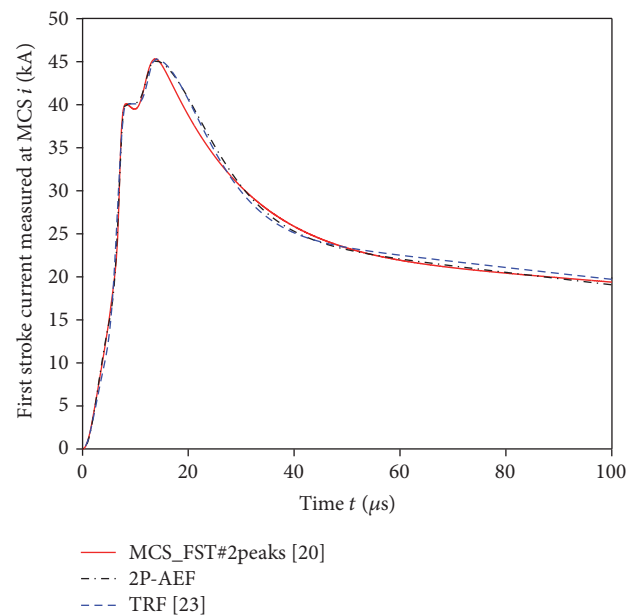


FIGURE 8: Measured current MCS_FST#2peaks [20], TRF [23], and 2P-AEF(2,1,2).

As the second example, the negative first stroke current measured at Morro do Cachimbo station in Brazil [21] is approximated by 2P-AEF(2,1,2) with 7 parameters estimated by GA. Parameters values for Example 2 are given in Table 4. Waveshape of the measured current denoted by MCS-FST#2peaks in [20], approximated by the sum of seven Heidler's functions (1), is the goal function for GA. Parameters of TRF are obtained by the least squares method [23] and denoted by LS TRF in Table 4. Results of these approximations are given in 100 μ s in Figure 8, and first derivatives of these currents are given in 20 μ s in Figure 9.

Grade-Spread chart, obtained by FSV code which is applied to the sum of seven Heidler's functions representing MSS_FST#2peaks results from [20] and its approximation by 2P-AEF(2,1,2) using GA, is presented in Figure 10. ADMc confidence histogram is given in Figure 11(a), ADMi point-by-point comparison of the amplitude differences in Figure 11(b). EX score is obtained (94%). For the approximation of amplitudes by GA 2P-AEF, the following scores are obtained: EX for 94%, VG for 5%, and G for 1% of results. Analysis by FSV code results in the Grade value 1 and Spread value 1 which stand for the best quality of

TABLE 4: 2P-AEF parameters in approximations of lightning currents.

	Example 1		Example 2		Example 3	Example 4
	GA 2P-AEF	LS TRF [23]	GA 2P-AEF	LS TRF [23]		
b_{11}	0.4020	0.37	0.4653	0.37	0.2366	1.1997
b_{12}	0.5980	0.63	0.5347	0.63	0.7634	-0.1997
a_{11}	2.7948	2.2	2.5624	2.2	1.5045	8.5640
a_{12}	83.551	28	58.8574	28	12.487	12.1617
b_{21}	1	1	1	1	1	1
a_{21}	9.6746	5.5	12.2015	15	27.919	0.9004
b_{31}	0.3784	0.4	0.4551	0.45	0.6191	0.6475
b_{32}	0.6216	0.6	0.5449	0.55	0.3809	0.3525
a_{31}	1.9436	2	2.7653	3.3	0.0399	0.0100
a_{32}	0.0754	0.06	0.0583	0.055	1.2955	4.0248
t_{m1} [μ s]	7.53	8.2	8	8.2	10.6	3.6733
I_{m1} [kA]	27.7	27.66	40.1	40.07	29.67	14.862
t_{m2} [μ s]	13.6	13.6	13.6	13.8	15.9	6.9
$I_{m1} + I_{m2}$ [kA]	31	31	45.1	45.28	30	10.862

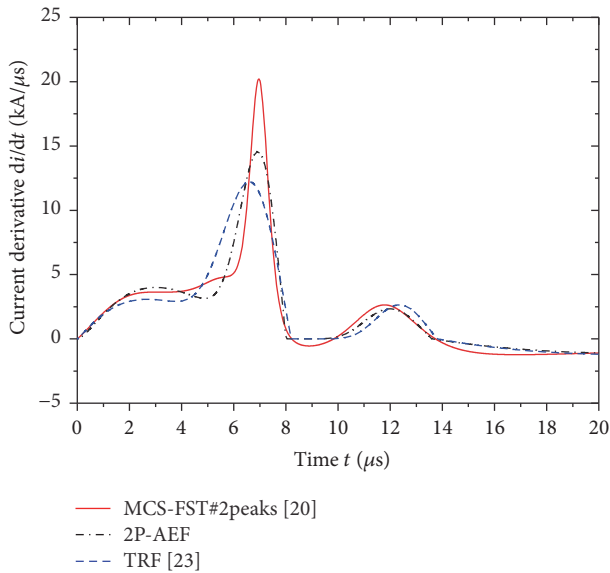


FIGURE 9: Derivatives of MCS_FST#2peaks [20], TRF [23], and 2P-AEF(2,1,2).

approximation. For MCS_FST#2peaks current from [20] and its approximation obtained by 2P-AEF(2,1,2) using GA, Grade value is 1 and Spread value 1, as given in Figure 12. Amplitude approximation has EX (89%) and VG (11%) scores as given in Figure 13(a), and ADMi is as in Figure 13(b).

5. Approximation of the Typical Negative First Stroke Current by 2P-AEF

Typical waveshape representing 88 measured negative first stroke currents [1], normalized to the maximum current value, is approximated by 2P-AEF(2,1,2) and presented in Figure 14. As 50% of measured negative first strokes currents

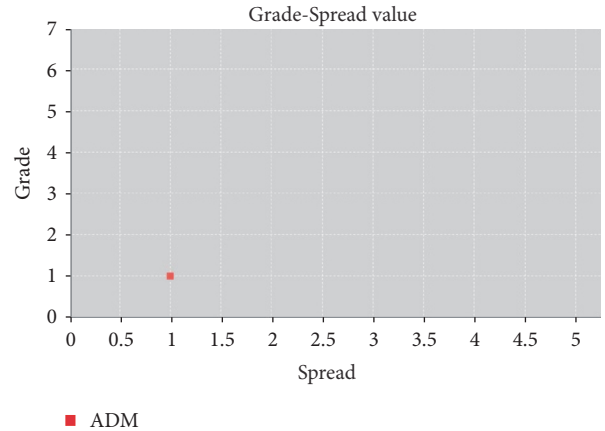


FIGURE 10: Grade-Spread value obtained by FSV applied to MSS_FST#2peaks results [20] and its approximation by 2P-AEF(2,1,2) using GA for parameters evaluation.

exceed 30 kA [1], it is often chosen as typical maximum current for this waveshape (which is the second peak $I_m = I_{m1} + I_{m2} = 30$ kA at $t_{m2} = 15.9$ μ s).

DEXP function parameters are obtained in [36] by Marquart least squares method in order to approximate current waveshape of typical negative first stroke from [1]. However, due to a very steep rise of DEXP function at $t = 0$, unlike slow rise of the approximated waveshape, this could not result in an accurate approximation. Certain improvement in the rising part is obtained by using Pulse function and is somewhat better by using Heidler's function, both optimized by Marquart least squares method [39]. Such a waveshape may be approximated only by more complex functions or by a linear combination of usually used functions. However, 2P-AEF(2,1,2) is suitable for approximation of this waveshape with just 7 parameters to be determined, as in previous examples. 2P-AEF's parameters are obtained by GA and their

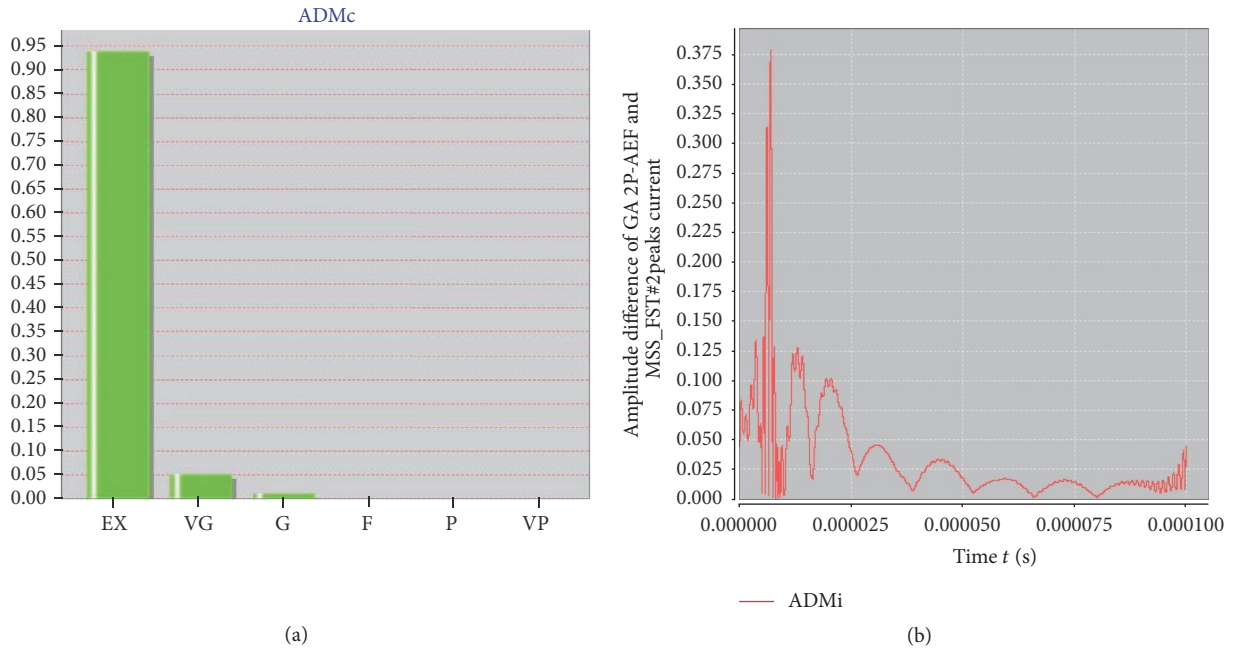


FIGURE 11: (a) ADMc and (b) ADMi obtained by FSV applied to MSS_FST#2peaks results [20] and its approximation by 2P-AEF(2,1,2) using GA for parameters evaluation.

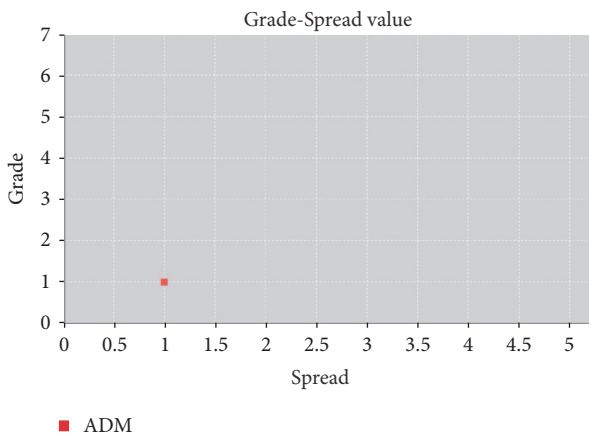


FIGURE 12: Grade-Spread value obtained by FSV applied to MCS_FST#2peaks results [20] and its approximation by 2P-AEF(2,1,2) using GA for parameters evaluation.

values are given in Table 4 for Example 3. Waveshapes of the normalized typical negative first stroke current [1] and its approximations by DEXP, Pulse, Heidler's function, and 2P-AEF(2,1,2), for parameters evaluated by GA, are presented in Figure 14.

Better approximation in the decaying part may be also obtained by 2P-AEF with more parameters in the third interval (after the second peak), for example, by 2P-AEF(2,1,3) with $K = 9$ parameters or 2P-AEF(2,1,4) with $K = 11$ parameters. A simple form of the function is preferable in many applications, if it is still able to correctly approximate the measured waveshape, so it was the reason to choose the smaller number of parameters.

6. Approximation of Rocket-Triggered Negative Stroke Currents by 2P-AEF

The approximation of rocket-triggered lightning current [28] was dealt with in [38, 39]. Heidler's, Pulse, and DEXP functions were optimized by using Marquart least squares method in order to represent this set of measured data. Heidler's function is better than the other two in representing the rising part of this current waveshape, but the decaying part is not represented well by any of these functions, due to its two-peaked waveshape. These waveshapes are given in Figure 15. However, the maximum current value and time to half of the maximum value are well approximated. 2P-AEF(2,1,2) is applied for approximation of this waveshape and its parameters are obtained by GA. The parameters values are given in Table 4 (Example 4). This function is also presented in Figure 15 and denoted by 2P-AEF.

If compared to other functions, the waveshape obtained by 2P-AEF's approximation has better accuracy for just 7 parameters determined by GA. Accuracy of this approximation may be also improved by introducing more terms in the decaying part (for $k_3 \geq 3$).

7. Conclusion

There are many possible applications of evolutionary algorithms in lightning research [10–14, 16, 17, 43]. Among these, genetic algorithm application to estimation of function parameters for curve fitting is presented in this paper. Measured multi-peaked waveshapes of lightning currents and typical lightning current waveshapes of the negative first strokes are approximated in this paper by 2P-AEFs with parameters estimated by GA. If compared to other functions

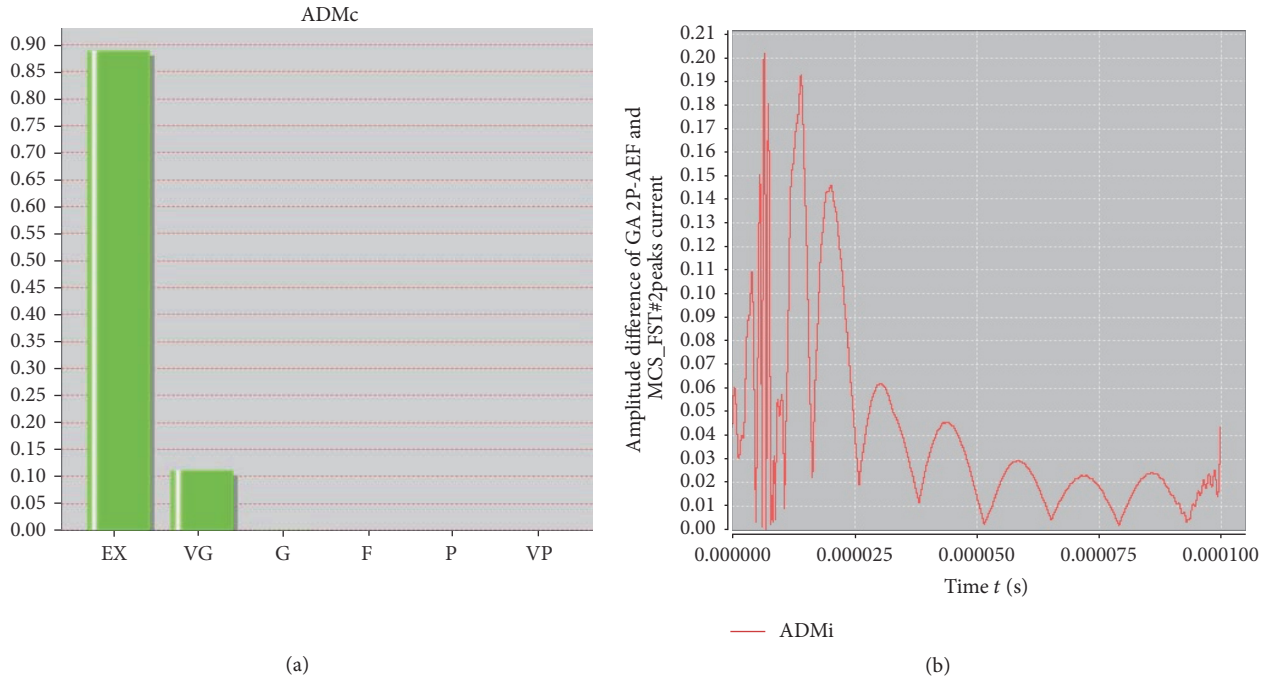


FIGURE 13: (a) ADMc and (b) ADMi obtained by FSV applied to MCS_FST#2peaks results [20] and its approximation by 2P-AEF(2,1,2) using GA for parameters evaluation.

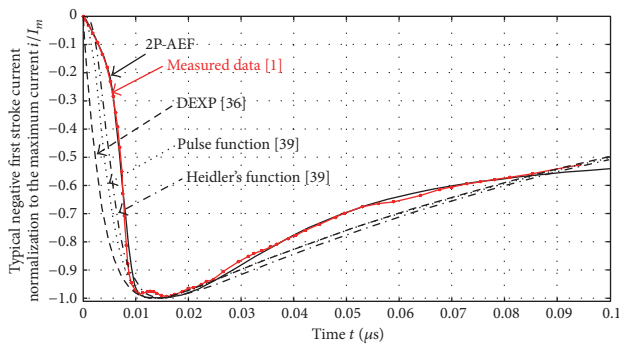


FIGURE 14: Normalized typical negative first stroke current [1] and its approximations by DEXP, Pulse, Heidler's function, and 2P-AEF(2,1,2).

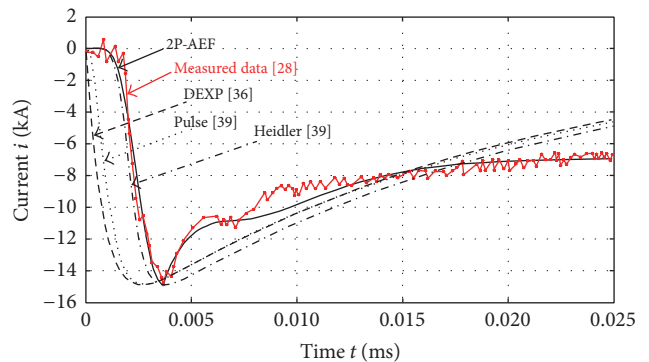


FIGURE 15: Measured rocket-triggered lightning current [28] and its approximations by DEXP, Pulse, Heidler's function, and 2P-AEF(2,1,2).

used for this purpose, better accuracy of approximation is obtained by 2P-AEF for a smaller number of parameters to be determined. Analytical expressions for 2P-AEF's first derivative, integral, integral of the square of this function, and its Fourier transform are given in [23–25] which makes 2P-AEF suitable for time and frequency domain calculations of lightning electromagnetic fields and lightning induced effects.

Genetic algorithm is applied to the estimation of 2P-AEF's parameters in approximation of an assumed current waveshape [27], and the same procedure is used in cases of measured lightning currents of negative first strokes. For 2P-AEF and its parameters evaluated by GA, the quality of approximation is confirmed by FSV tools [29–31, 42]. There

is an excellent agreement of results obtained by 2P-AEFs and the goal functions. Currents derivatives waveshapes are also compared. Further research will aim at approximation of both currents and currents derivatives waveshapes by using GA. In comparison to other functions from the literature, the best quality of 2P-AEF's approximation is obtained for the typical negative first stroke [1] which is useful in lightning models verification and lightning protection studies. Measured rocket-triggered lightning currents are also well represented by 2P-AEFs.

The main advantage of this function is that its N -peaked form may be used for approximation of various multip peaked waveshapes. For such waveshapes, N peaks at the corresponding time moments are chosen prior to application of

GA. Greater numbers of terms in the intervals between the peaks improve the accuracy of approximation at the expense of increased number of parameters to be determined. However, a procedure applying GA for optimization of NP-AEF's parameters is generalized, so it may be useful in curve fitting of any waveshape.

Conflicts of Interest

The authors declare that there are no conflicts of interest regarding the publication of this paper.

Acknowledgments

The authors are grateful to Professor A. Orlandi from the University of LAquila in Italy for providing an opportunity to use the FSV Tool Version 2.0.9L [42] developed in the frame of FSV project in order to validate the quality of computational results. The research presented in this paper is supported in part by Ministry of Education, Science and Technological Development of the Republic of Serbia (Project HUMANISM III 44004).

References

- [1] K. Berger, R. B. Anderson, and H. Kröniger, "Parameters of lightning flashes," *Electra*, vol. 41, pp. 23–37, 1975.
- [2] R. B. Anderson and A. J. Eriksson, "Lightning parameters for engineering application," *Electra*, vol. 69, pp. 65–102, 1980.
- [3] Y. T. Lin, M. A. Uman, J. A. Tiller et al., "Characterization of lightning return stroke electric and magnetic fields from simultaneous two-station measurements," *Journal of Geophysical Research*, vol. 84, no. 10, pp. 6307–6314, 1979.
- [4] V. A. Rakov, "Transient response of a tall object to lightning," *IEEE Transactions on Electromagnetic Compatibility*, vol. 43, no. 4, pp. 654–661, 2001.
- [5] J. C. Willett, J. C. Bailey, V. P. Idone, A. Eybert-Berard, and L. Barret, "Submicrosecond intercomparison of radiation fields and currents in triggered lightning return strokes based on the transmission-line model," *Journal of Geophysical Research*, vol. 94, no. D11, Article ID 13286, pp. 13–286, 1989.
- [6] C. Leteinturier, C. Weidman, and J. Hamelin, "Current and electric field derivatives in triggered lightning return strokes," *Journal of Geophysical Research*, vol. 95, no. 1, pp. 811–828, 1990.
- [7] W. R. Gamerota, J. O. Elismé, M. A. Uman, and V. A. Rakov, "Current waveforms for lightning simulation," *IEEE Transactions on Electromagnetic Compatibility*, vol. 54, no. 4, pp. 880–888, 2012.
- [8] *Protection against Lightning Part 1: General principles*, IEC Standard 62305, 2nd edition, 2010.
- [9] V. A. Rakov and M. A. Uman, "Review and evaluation of lightning return stroke models including some aspects of their application," *IEEE Transactions on Electromagnetic Compatibility*, vol. 40, no. 4, pp. 403–426, 1998.
- [10] M. Izadi, M. Z. A. Ab Kadir, C. Gomes, and M. T. Askari, "Evaluation of lightning return stroke parameters using measured magnetic flux density and PSO algorithm," *Przegląd Elektrotechniczny (Electrical Review)*, vol. 88, no. 10a, pp. 201–204, 2012.
- [11] M. Izadi, M. Z. A. Ab Kadir, M. T. Askari, and M. Hajikhani, "Evaluation of lightning current using inverse procedure algorithm," *International Journal of Applied Electromagnetics and Mechanics*, vol. 41, pp. 267–278, 2013.
- [12] G. Yang, Z. Yu, Y. Zhang, S. Chen, B. Zhang, and J. He, "Evaluation of Lightning Current and Return Stroke Velocity Using Measured Far Electric Field Above a Horizontally Stratified Ground," *IEEE Transactions on Electromagnetic Compatibility*, pp. 1–9, 2017.
- [13] K. Chandrasekaran and G. S. Punekar, "Use of genetic algorithm to determine lightning channel-base current-function parameters," *IEEE Transactions on Electromagnetic Compatibility*, vol. 56, no. 1, pp. 235–238, 2014.
- [14] G. Yang, F. Zhou, Y. Ma, Z. Yu, Y. Zhang, and J. He, "Identifying lightning channel-base current function parameters by powell particle swarm optimization method," *IEEE Transactions on Electromagnetic Compatibility*, pp. 1–6, 2017.
- [15] F. Heidler, "Analytische blitzstromfunktion zur LEMP-berechnung," in *Proceedings of the Ninth Power Systems Computation Conference on Lightning Protection*, Munich, Germany, 1985.
- [16] J. L. Bermudez, C. A. Peña-Reyes, F. Rachidi, and F. Heidler, "Use of genetic algorithms to extract primary lightning current parameters," in *Proceedings of the EMC Europe 2002 International Symposium on Electromagnetic Compatibility*, pp. 241–246, 2002.
- [17] G. Yang, K. Chen, Z. Yu, Y. Zhang, F. Zhou, and J. He, "An inversion method for evaluating lightning current waveform based on time series neural network," *IEEE Transactions on Electromagnetic Compatibility*, vol. 59, no. 3, pp. 887–893, 2017.
- [18] C. Bruce and R. Golde, "The lightning discharge," *Journal of the Institution of Electrical Engineers - Part II: Power Engineering*, vol. 88, no. 6, pp. 487–505, 1941.
- [19] Z. Feizhou and L. Shanghe, "A new function to represent the lightning return-stroke currents," *IEEE Transactions on Electromagnetic Compatibility*, vol. 44, no. 4, pp. 595–597, 2002.
- [20] A. De Conti and S. Visacro, "Analytical representation of single- and double-peaked lightning current waveforms," *IEEE Transactions on Electromagnetic Compatibility*, vol. 49, no. 2, pp. 448–451, 2007.
- [21] S. Visacro, A. Soares Jr., M. A. O. Schroeder, L. C. L. Cherchiglia, and V. J. de Sousa, "Statistical analysis of lightning current parameters: measurements at Morro do Cachimbo station," *Journal of Geophysical Research D: Atmospheres*, vol. 109, no. 1, pp. D01105–11, 2004.
- [22] F. H. Silveira, A. De Conti, and S. Visacro, "Lightning overvoltage due to first strokes considering a realistic current representation," *IEEE Transactions on Electromagnetic Compatibility*, vol. 52, no. 4, pp. 929–935, 2010.
- [23] V. Javor, "Approximation of a double-peaked lightning channel-base current," *COMPEL - The International Journal for Computation and Mathematics in Electrical and Electronic Engineering*, vol. 31, no. 3, pp. 1007–1017, 2012.
- [24] V. Javor and P. D. Rancic, "A channel-base current function for lightning return-stroke modeling," *IEEE Transactions on Electromagnetic Compatibility*, vol. 53, no. 1, pp. 245–249, 2011.
- [25] V. Javor, "New functions for representing iec 62305 standard and other typical lightning stroke currents," *Journal of Lightning Research*, vol. 4, no. 1, pp. 50–59, 2012.
- [26] K. Lundengård, M. Rančić, V. Javor, and S. Silvestrov, "Estimation of parameters for the multi-peaked AEF current functions," *Methodology and Computing in Applied Probability*, pp. 1–15, 2016.

- [27] F. Heidler and J. Cvetić, "A class of analytical functions to study the lightning effects associated with the current front," *European Transactions on Electrical Power*, vol. 12, no. 2, pp. 141–150, 2002.
- [28] J. Schoene, M. A. Uman, V. A. Rakov et al., "Characterization of return-stroke currents in rocket-triggered lightning," *Journal of Geophysical Research Atmospheres*, vol. 114, no. 3, Article ID D03106, 2009.
- [29] A. P. Duffy, A. J. M. Martin, A. Orlandi, G. Antonini, T. M. Benson, and M. S. Woolfson, "Feature selective validation (FSV) for validation of computational electromagnetics (CEM). Part 1 - the FSV method," *IEEE Transactions on Electromagnetic Compatibility*, vol. 48, no. 3, pp. 449–458, 2006.
- [30] A. Orlandi, A. P. Duffy, B. Archambeault, G. Antonini, D. E. Coleby, and S. Connor, "Feature selective validation (FSV) for validation of computational electromagnetics (CEM). Part II - assessment of fsv performance," *IEEE Transactions on Electromagnetic Compatibility*, vol. 48, no. 3, pp. 460–467, 2006.
- [31] IEEE Standards Association, "Standard for validation of computational electromagnetics computer modeling and simulations," *IEEE Standards Association 1597.1*, 2008.
- [32] G. Diendorfer and M. A. Uman, "An improved return stroke model with specified channel-base current," *Journal of Geophysical Research*, vol. 95, no. D9, p. 13621, 1990.
- [33] C. A. Nucci, G. Diendorfer, M. Uman, F. Rachidi, and C. Mazzetti, "Lightning return-stroke models with channel-base specified current: a review and comparison," *Journal of Geophysical Research*, vol. 95, no. 12, pp. 20395–20408, 1990.
- [34] F. Heidler and Ch. Hopf, "Lightning current function for LEMP calculation," in *Proceedings of the 22nd International Conference on Lightning Protection*, Budapest, Hungary, 1994.
- [35] D. Marquardt, "An algorithm for least-squares estimation of nonlinear parameters," *SIAM Journal on Applied Mathematics*, vol. 11, no. 2, pp. 431–441, 1963.
- [36] D. Lovrić, S. Vujević, and T. Modrić, "Least squares estimation of double-exponential function parameters," in *Proceedings of the 11th International Conference on Applied Electromagnetics PIEC*, pp. 1–4, Niš, Serbia, 2013.
- [37] S. Vujević, D. Lovrić, and I. Jurić-Grgić, "Least squares estimation of Heidler function parameters," *European Transactions on Electrical Power*, vol. 21, no. 1, pp. 329–344, 2011.
- [38] D. Lovrić, S. Vujević, and T. Modrić, "On the estimation of Heidler function parameters for reproduction of various standardized and recorded lightning current waveshapes," *International Transactions on Electrical Energy Systems*, vol. 23, no. 2, pp. 290–300, 2013.
- [39] K. Lundengård, M. Rančić, V. Javor, and S. Silvestrov, "Estimation of pulse function parameters for approximating measured lightning currents using the Marquardt least-squares method," in *Proceedings of the 2014 International Symposium on Electromagnetic Compatibility, EMC Europe 2014*, pp. 571–576, Gothenburg, Sweden, September 2014.
- [40] D. E. Goldberg, *Genetic Algorithms in Search, Optimization and Machine Learning*. Addison-Wesley, Reading, MA, USA, 1989.
- [41] K. Wong, H. M. Ryan, J. Tindle, J. Blackett, and M. W. Watts, "Digital measurement of lightning impulse parameters using curving fitting algorithms," in *Proceedings of the 11th International Symposium on High-Voltage Engineering (ISH 99)*, London, UK, August 1999.
- [42] "FSV Tool Version 2.0.9L," EMC Laboratory of the University of L'Aquila, 2017, http://orlandi.ing.univaq.it/pub/FSV_Tool.20.
- [43] D. Aranguren, A. Delgadillo, M. Vargas, E. Pérez, and H. Torres, "Estimation of lightning electrostatic parameters based on atmospheric electric field measurements and genetic algorithms," in *Proceedings of the 19th International Lightning Detection Conference*, 2006.

Research Article

Design, Simulation, and Optimization of an Irregularly Shaped Microstrip Patch Antenna for Air-to-Ground Communications

L. A. R. Ramirez and J. C. A. Santos

Electrical Engineering Department, Military Institute of Engineering (IME), Rio de Janeiro, RJ, Brazil

Correspondence should be addressed to J. C. A. Santos; araujo@ime.eb.br

Received 22 December 2016; Revised 20 February 2017; Accepted 5 March 2017; Published 28 March 2017

Academic Editor: Sotirios K. Goudos

Copyright © 2017 L. A. R. Ramirez and J. C. A. Santos. This is an open access article distributed under the Creative Commons Attribution License, which permits unrestricted use, distribution, and reproduction in any medium, provided the original work is properly cited.

In this study an irregularly shaped microstrip patch antenna was designed, simulated, and optimized for air-to-ground communication (ATG) applications. The process started with the design of a rectangular patch antenna with the traditional transmission line and cavity methods, followed by a simulation with the finite-difference time-domain method (FDTD) in conjunction with a genetic algorithm (GA). The aim of the study was to design an efficient patch antenna. The designed antenna is resonating at 14.25 GHz with 35 dB return loss. The 10 dB bandwidth of the antenna is 3.7 GHz.

1. Introduction

The use of microstrip structures to radiate electromagnetic waves started in the 1950s [1]. The earliest form of planar antennas, integrated with planar transmission lines, was developed by Deschamps and Sichak [2]. Practical implementation started to increase in the 1970s when suitable substrate materials became available. The development of microstrip antennas in the 1970s and 1980s has been well documented by Bahl and Bhartia [3] and James and Hall [4], and later several good books were published on this subject [5–16].

A microstrip patch antenna in its simplest configuration consists of a radiating patch on one side of a dielectric substrate and a ground plane on the other side. With regard to the shape, microstrip antenna patches can be regular or irregular. Typical regular shapes are rectangular, square, circular, elliptic, and triangular, among others. These shapes have been widely studied and the design procedures are well established. They are used as conformal antennas for airplanes, cars, missiles, portable devices and many other applications. Regularly shaped antennas are more common, mainly because they are easy to analyze and usually present a symmetric radiation pattern. The irregularly shaped patch antenna refers to a microstrip antenna whose patch geometry is designed to fulfill a specific antenna property such as

compactness, wideband characteristics, and multiresonant operation. Examples include H-Shape, E-Shape, and L-Shape, as well as combinations of these antennas [3–16]. In the past few years, patch antennas with nonintuitive and novel shapes have appeared. The radiating patch is modified through an optimization process, aimed at improving its specific properties, in particular increasing the bandwidth [17–22].

In [17], Michael Johnson and Rahmat-Samii described the technique of combining GA optimization with method of moments for broadband patch antenna design. Their study included the optimization of a simple patch antenna to produce a wider operational bandwidth than classical designs. Specifically, the goal was to produce an irregularly shaped patch antenna with a voltage standing wave ratio (VSWR) of 2:1 over 20% bandwidth centered at 3 GHz. The GA optimized the subpatch by removing the square metal sections from the patch region. Choo et al. [18] designed a broadband patch antenna using an approach similar to that described in [17]. They began with a metal patch, in which subpatches were represented by Boolean subpatches, either ones (metal) or zeros (nonmetal). The goal was to broaden the bandwidth of a microstrip antenna around the center frequency of 2 GHz by changing the patch shape. Chapter 32 of a handbook published by Balanis [19] presents an overview of antenna optimization using GA and provides some cases of use and a selected bibliography. In [20], Griffiths et al.

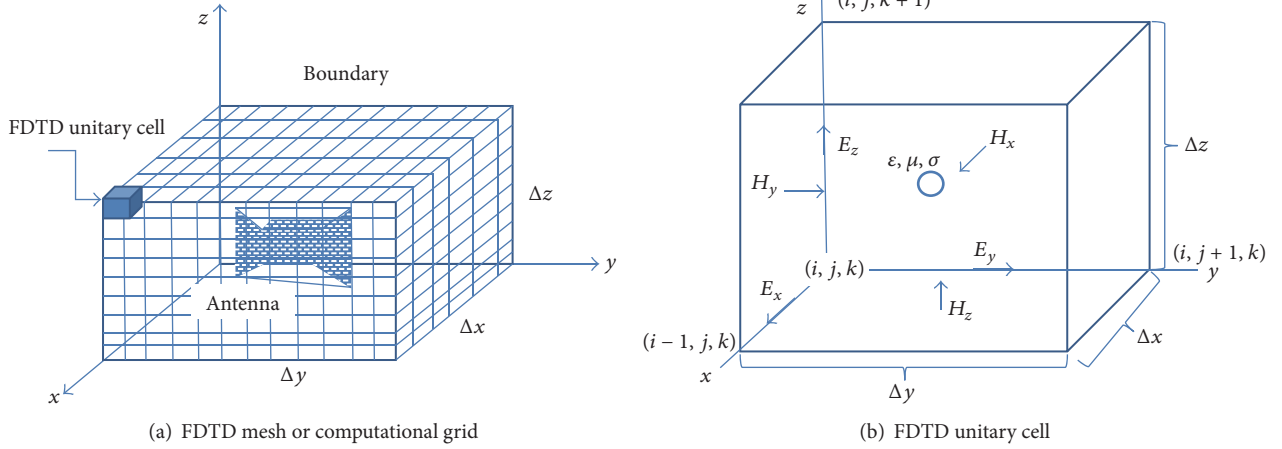


FIGURE 1: FDTD (a) grid and (b) field components in a unitary cell.

report the use of GA for the generation of compact antennas (broadband and multiband), where the patch is modified using ellipses to create new forms, with higher bandwidth and return loss. In [21], a semiautomatic antenna design method is proposed to design a multiband monopole antenna. In the antenna optimization, particle swarm optimization (PSO) was used, with a new technique of grid patch generation, and good simulation and measurement results were obtained. In [22], Modiri and Kiasaleh used the binary particle swarm optimization (BPSO) algorithm to design several irregularly shaped microstrip antennas, the main focus being the frequency selectivity of a software-defined radio (SDR).

As in [17–22], an irregularly shaped microstrip antenna is the object of this study; however, here it will be applied to air-to-ground (ATG or A2G) communication.

Ground-to-ground radio communication is a common application of mobile wireless networks. ATG communication has received increased attention recently [23]. It is used for communication between aircraft and stations on the ground or on water. Line-of-sight (LOS) conditions are usually established. Internet service providers also use ATG to connect planes to the Internet, which has significant limitations in terms of the speed and latency of the connection (on-board WiFi allows no video streaming and no fast browsing, phone calls are of poor quality, etc.). ATG systems are less expensive than satellite-based systems and, thus, services can be provided to passengers at lower cost [23]. Also, this technology will enable a much larger set of applications due to the lower latency and cost per bit. Interest is enhanced by the fact that several companies (e.g., Alcatel and Nokia) currently provide 4G services using air-to-ground LTE [24]. This technology has also become of interest for unmanned aerial vehicles (UAVs), commonly known as a drones, for military, agriculture, and surveillance applications [25].

In this paper, we report the design of a microstrip patch antenna for the ATG frequency band, starting from the classical rectangle microstrip antenna with an inset-fed line to obtain an improved antenna. In this study, the finite-difference time-domain numerical method FDTD-3D

is combined with a genetic algorithm (GA) to optimize the bandwidth and return loss of the antenna. The full wave FDTD-3D method is described in Section 2. Section 3 presents the GA. The design of the antenna is described in Section 4, and the numerical results are reported in Section 5. Finally, Section 6 provides the conclusions.

2. Finite Differences in Time Domain

In the finite-difference time-domain method, Maxwell equations in a differential form are transformed into discrete finite-difference equations. This results in a fully explicit system of difference equations, whereby chronological values of the electric and magnetic field components are obtained in a leap-frog manner; that is, the electric field is solved at a given instant of time and the magnetic field is solved at the next time instant. The process is cyclically repeated. Spatially, the calculation of the electric and magnetic field components is dependent only on the neighbors in each case.

For the FDTD-3D case, the computational domain is divided into small cells (Figure 1(a)). The components \vec{E} and \vec{H} are distributed in space, with the components \vec{E} positioned on the edges and components \vec{H} distributed at the center of the faces of the cells (Figure 1(b)) [26].

With this field distribution, with two adjacent cubes connected by a vertex, each field component of \vec{E} is surrounded by four components of \vec{H} , and similarly each component of \vec{H} is surrounded by four components of \vec{E} , which can be seen in detail in Figure 2.

In linear, homogeneous, isotropic, and free source media, Maxwell equations can be written as

$$\begin{aligned} \nabla \times \vec{E} &= -\mu \frac{\partial \vec{H}}{\partial t}, \\ \nabla \times \vec{H} &= \sigma \vec{E} + \epsilon \frac{\partial \vec{E}}{\partial t}. \end{aligned} \quad (1)$$

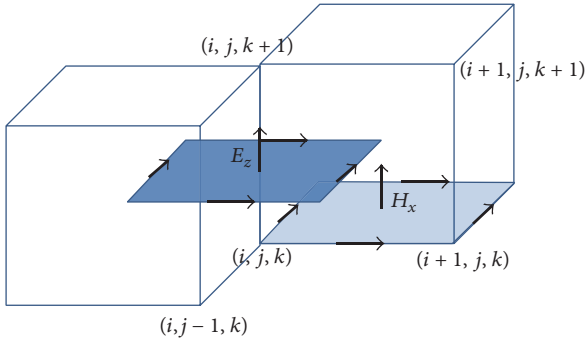


FIGURE 2: Fields components of \vec{E} and \vec{H} in two adjacent unitary cells.

The spatial and temporal derivatives in (1) are written in a discrete form using a central difference scheme.

The choice of cell size is critical in applying the FDTD method. It must be small enough to permit accurate calculations at the highest frequencies of interest and yet be large enough to ensure that the computational resources are manageable. The cell size is directly affected by the objects in the mesh. Once the cell size is chosen, the maximum time step is determined by satisfying the Courant stability criterion

$$\Delta t \leq \frac{1}{v_{\max} \sqrt{1/(\Delta x_{\min})^2 + 1/(\Delta y_{\min})^2 + 1/(\Delta z_{\min})^2}} \quad (2)$$

which enforces the property that an incident waveform cannot pass through more than one cell during one time step. This is because during one time step the FDTD algorithm can only propagate across one cell to its nearest neighbor. In (2), v_{\max} is the maximum speed of wave propagation in the model, Δx , Δy , and Δz are the space increments, and Δt is the time step [26].

Together with the FDTD method, the uniaxial perfectly matched layer (UPML) [26, 27] was used. This is an absorbent boundary condition, used to simulate the propagation of waves in free space outside the computational domain, such as an anechoic chamber. Figure 3 illustrates the UPML with an FDTD grid.

3. Genetic Algorithm

A genetic algorithm (GA) is an optimization technique that can handle the common characteristics of electromagnetic fields. It is an iterative optimization procedure and it maintains a population of probable solutions (chromosomes) within a search space (which is usually discrete) over many simulated generations.

The basic principles of GA were inspired by the mechanism of natural selection of Darwin and genetic laws, where stronger individuals are likely to be winners (the fittest) in a competing environment and present better characteristics for adaptation [28]. GA assumes that the potential solution of any problem is an individual from a population. Any chromosome can be represented by a set of parameters. These parameters are regarded as the genes and can be structured

by a string of values (alleles) in binary form or real values. In a computer algorithm, genes represent the basic building blocks of a genetic algorithm. Figure 4 shows a sample of a binary chromosome and three of its components.

A chromosome (or individual) is an array of genes, and a group of chromosomes is known as a population (see the following).

Matrix representation of components of a genetic algorithm, adapted from [28], is as follows:

$$\text{population} = \underbrace{\begin{bmatrix} \text{chrom}_1 \\ \text{chrom}_2 \\ \text{chrom}_3 \\ \text{chrom}_4 \end{bmatrix}}_{\text{chromosomes}} = \underbrace{\begin{bmatrix} g_{11} & g_{12} & \dots & g_{1M} \\ g_{21} & g_{22} & & \\ \vdots & & \ddots & \vdots \\ g_{N1} & & \dots & g_{NM} \end{bmatrix}}_{\text{genes}} \quad (3)$$

Each gene of a chromosome will represent a property of the patch antenna and all genes belonging to a chromosome will represent an antenna configuration. At each iteration (or generation) three basic genetic operations (“selection,” “crossover,” and “mutation”) are performed. The initial population is a randomly generated chromosome satisfying boundary or system constraints to the known configuration that needs to be optimized. A good choice of the population size optimizes the convergence of the simulation.

During each generation, the chromosomes are evaluated, using an associated cost function, and this gives some measurements for the fitness or relative merit. A new generation is formed by selection, according to the fitness values, to create the next generation of individuals from the previous population. These individuals are called parents while those created by applying evolutionary operators to the parents are referred to as offspring. These new chromosomes (offspring) can be formed using several techniques, for instance, by either merging two chromosomes from the current generation using a crossover operator or modifying a chromosome using a mutation operator. In this process, some of the parents and offspring are chosen while others are rejected, so as to keep the population size constant. Fitter chromosomes have a higher probability of being selected. After several generations, the algorithms converge to the best chromosome, which is expected to represent the optimum or suboptimal solution to the problem. Figure 5 shows a flowchart of the GA used.

4. Microstrip Antenna Design

4.1. Antenna Design. The first step in the design of the proposed antenna was the dimensioning of a classical rectangular patch antenna through the transmission line and resonant cavity methods [29]. The antenna is shown in Figure 6. The frequency of resonance was chosen in accordance with air-to-ground technology. Input data were center frequency (f_0) at 14.25 GHz and frequency band range of 13.25 to 15.25 GHz. The three metal components (ground plane, antenna patch, and feed line) have a conductivity of 5.8×10^7 S/m (for copper clad substrates). The substrate RT/duroid 5880 was used, which has a relative permittivity of 2.20. Additional

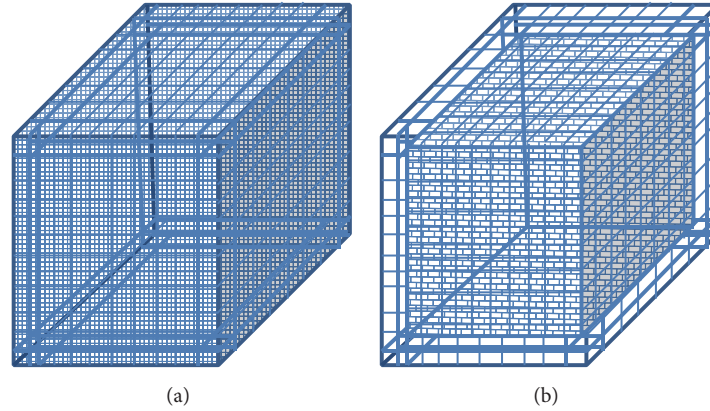


FIGURE 3: UPML layers around the FDTD mesh with (a) all layers and (b) removed frontal layers. The FDTD mesh is highlighted.

TABLE 1: Characteristics of microstrip inset patch antenna.

Component	Width (mm)	Length (mm)	Thickness (mm)
Ground plane (copper)	16.8	24.5	0.5
Patch (copper)	8.0	10.0	0.5
Substrate (duroid 5880)	16.6	28.5	3.5
Feed line (copper)	1.5	17.0	0.5

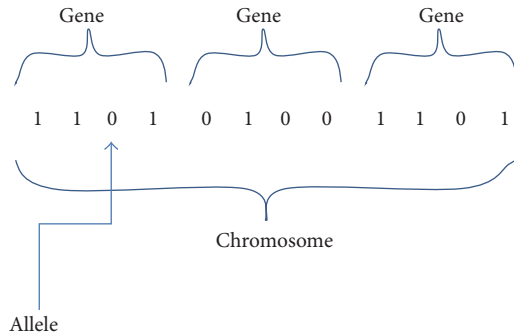


FIGURE 4: Sample of a binary chromosome.

parameters are given in Table 1. The origin of the coordinate system was set at the center of the ground plane, at zero height on the base.

4.2. FDTD Considerations. The FDTD method works in the time domain. Thus, the use of signals with variant spectrum is recommended. There are three approaches to this method: total field/scattered field formulation; additive source; and hard-source. Since the energy is introduced into the space-time lattice, the hard-source solution was used. This is incorporated into the FDTD code by specifying the electric field value at a specific location by a time function (typically Gaussian or a Gaussian derivative), which takes advantage of the wideband nature of the problem. In this study, Morlet's wavelet function was used. The driving field is given by

$$E_z(t) = E_0 \exp[-(2\pi f_b(t-t_0))^2] \cos[2\pi f_c(t-t_0)] \quad (4)$$

with $E_0 = 12$ V/m, $t_0 = 375$ ps, $f_c = 14.25$ GHz, and $f_b = 2000$ MHz, where E_0 is the signal amplitude, t_0 is the time at which the pulse reaches its maximum value, f_c is the center frequency, and t represents the propagation time signal with $0 \leq t \leq 8000\Delta t$, where $\Delta t = 0.0342$ ns is the time step. This signal is shown in Figure 7. The spatial steps $\Delta x = 0.234$ mm, $\Delta y = 0.21$ mm, and $\Delta z = 0.11$ mm were used. A mesh is generated by dividing the computational domain into $72 \times 113 \times 39$ tiny cells. The time step is calculated according to Courant criterion (see (2)). 8000 iterations were necessary to address the steady-state, rendering approximately 9 minutes of computer time.

4.3. Validation. The software implemented was verified by comparing the results for a common microstrip inset patch antenna with those obtained from the commercial software package CST-MWS[®]. The magnitudes of S_{11} for both packages are shown in Figure 8. The nature of the variation of S_{11} obtained with FDTD follows closely that obtained by CST-MWS.

4.4. GA Considerations. For the optimization process, all elements of the initial population refer to a standard rectangular patch antenna with inset (Figure 6). The corresponding resonant patch is divided into a binary matrix of 17×17 subpatches (see sample in Figure 9). The subpatches correspond to the intrinsic representation of the problem. This indicates the presence (set as 1) or the absence (set as 0) of copper in a candidate solution (chromosome). The idea is that, in the random generation of the initial population, the subpatches to be generated have behavior similar to that of the passive resonating elements. Considering that both the FDTD and GA are time-consuming processes, various

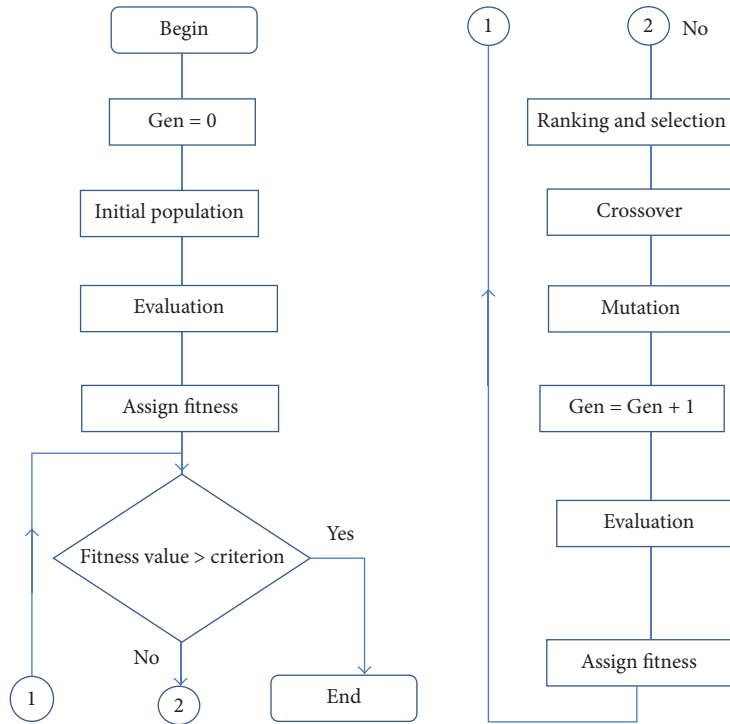


FIGURE 5: Flowchart of the basic genetic algorithm.

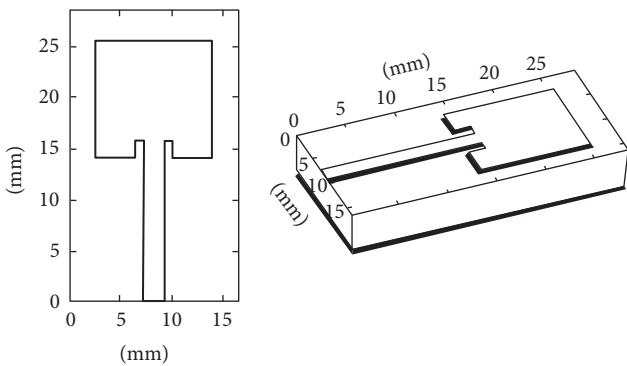


FIGURE 6: Microstrip antenna with inset (unscaled).

chromosome sizes were tested. A digital individual with 289 elements showed a good balance between accuracy and computational burden.

Each chromosome is composed of 289 alleles. Within the program a one-dimensional binary array represents the irregular patch antenna. Each subpatch is an exact multiple of the size of the corresponding dimensional step in order to create a second 17×17 mesh of subpatches. The latter is stored in a two-dimensional array. The corresponding conversion from vector to matrix and vice versa is done through a subroutine.

The initial size of the population was set at 70 chromosomes (all different). This number should be sufficient to ensure the generation of good parents (i.e., with sufficient diversity to ensure that some chromosomes have the desired

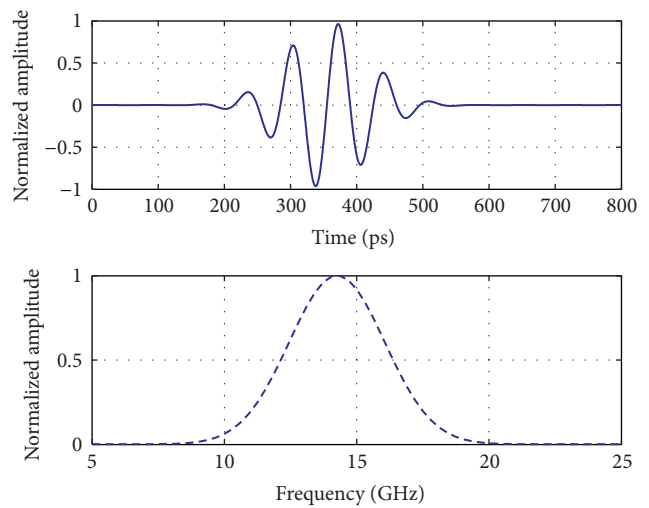


FIGURE 7: Signal excitation in time and frequency domains.

characteristics). For the evaluation of each population, the time consumed was 10.5 hours on a PC with i7 processor, 12 GB of RAM, and Nvidia® GeForce GT 610 Graphics Accelerator, with 2 GB DDR3/ 64 bits.

Another consideration is related to the fitness function used to evaluate if the individual is a good solution. Each chromosome in a population has a fitness value associated with it and the chromosomes are ranked from best to worst based on this value. This function is considered to be the most important part of the algorithm, because its success

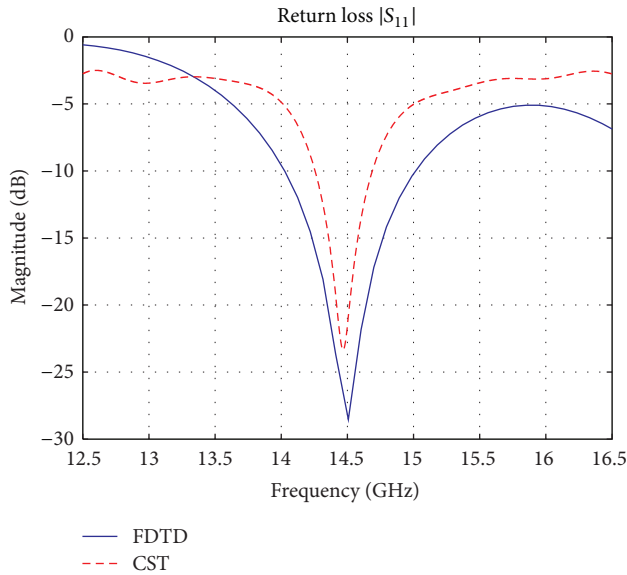


FIGURE 8: Simulated results for the return loss of a rectangular patch antenna with CST and the developed simulator.

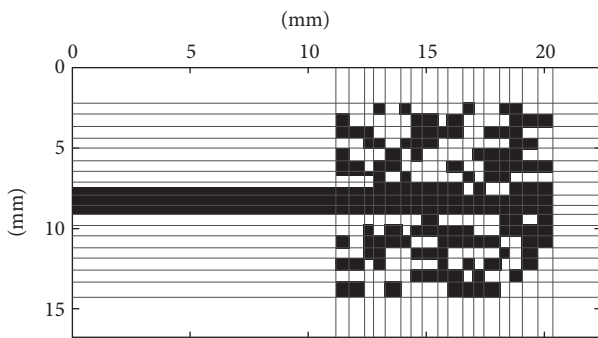


FIGURE 9: Patch antenna configuration in the evolutionary process.

is dependent on how well the fitness function evaluates each solution in relation to the overall objectives of the optimization problem. The fitness function is related to the bandwidth and the return loss (see (5)). The two optimization objectives functions were combined to form a single overall fitness function.

In (5), α is a weighting factor in the range $[0, 1]$. This parameter allows us to choose the emphasis or preference of one parameter with respect to another. The fitness function related to bandwidth is set to a minimum bandwidth of 2.0 GHz, as in the study described in [30], and the related return loss value is better than 20 dB, as reported in [31].

$$\text{fit} = \alpha \text{fitBW} + (1 - \alpha) \text{fitPR}. \quad (5)$$

For the application of the basic genetic operators, that is, selection, crossover, and mutation, the specific bit operator roulette wheel, single point crossover, and elitism, were used. In the roulette wheel, each member of the new population is selected in a random way from the elements of the previous population, where the probability of selecting a member from

the previous population is proportional to its fitness value. Crossover involves creating two “offspring” chromosomes from the complementary part of two “parent” chromosomes. A random point is chosen, the two parents are then divided, and in the left side the first parent becomes the left side of second parent and vice versa. A crossover probability controls the frequency of the operator, which was fixed at 0.8. In the mutation process, the operator mutation randomly flips some of the bits in a chromosome. Mutation probability was fixed at 0.05, changing the offspring properties. Crossover and mutation are important operators that are responsible for improving the diversity.

Elitism is the process of retaining or inserting the best individual into the next generation from the current generation. This is performed to avoid the loss of the best individual in any population during the crossover and mutation operations. Thus, using these operators, good candidates are retained while others are discarded in such a way that the population size remains constant.

5. Results

Figure 10 shows snapshots of the iterative evolutionary process, together with their respective S_{11} graphs (dB). Wideband and high return loss were the optimization criteria. Figures 10(a) and 10(b) show two instants in the evolutionary process in which the corresponding chromosomes have distinct characteristics. Figure 10(a) shows a return loss of the order of 26 dB and a poor bandwidth of 1 GHz, while Figure 10(b) shows a poor return loss but frequency response with a wideband behavior. These two chromosomes are the arguments in the crossover process that will generate the next individuals. The antennas in Figures 10(c) and 10(d) were the best solutions. In Figure 10(c) the peak value for the return loss is 27.04 dB, with a 10 dB bandwidth of 6 GHz. In Figure 10(d), the values for the return loss are around 35 dB, with a 10 dB bandwidth of 3.7 GHz, and better return loss is observed in the middle frequencies.

For the antenna of Figure 10(d), the corresponding radiation patterns are presented in Figure 11, at 13 GHz, 14.25 GHz, and 15 GHz, corresponding to the columns of the figure. This antenna presents 15 dB minimum return loss at ATG frequency range. The XY plane (azimuth) responses are shown in Figures 11(a), 11(b), and 11(c); the XZ plane responses are shown in Figures 11(d), 11(e), and 11(f); and the YZ plane responses are shown in Figures 11(g), 11(h), and 11(i).

6. Conclusions

In this study, a compact irregularly shaped microstrip patch antenna for use in ATG devices was designed. Excellent return loss and bandwidth values were obtained, with 10 dB bandwidths up to 6 GHz, and peak return loss of around 27 dB. The best antenna showed 15 dB minimum return loss over the full ATG frequency band. The finite-difference time-domain method (FDTD) was used in conjunction with a genetic algorithm. The proposed methodology can be applied

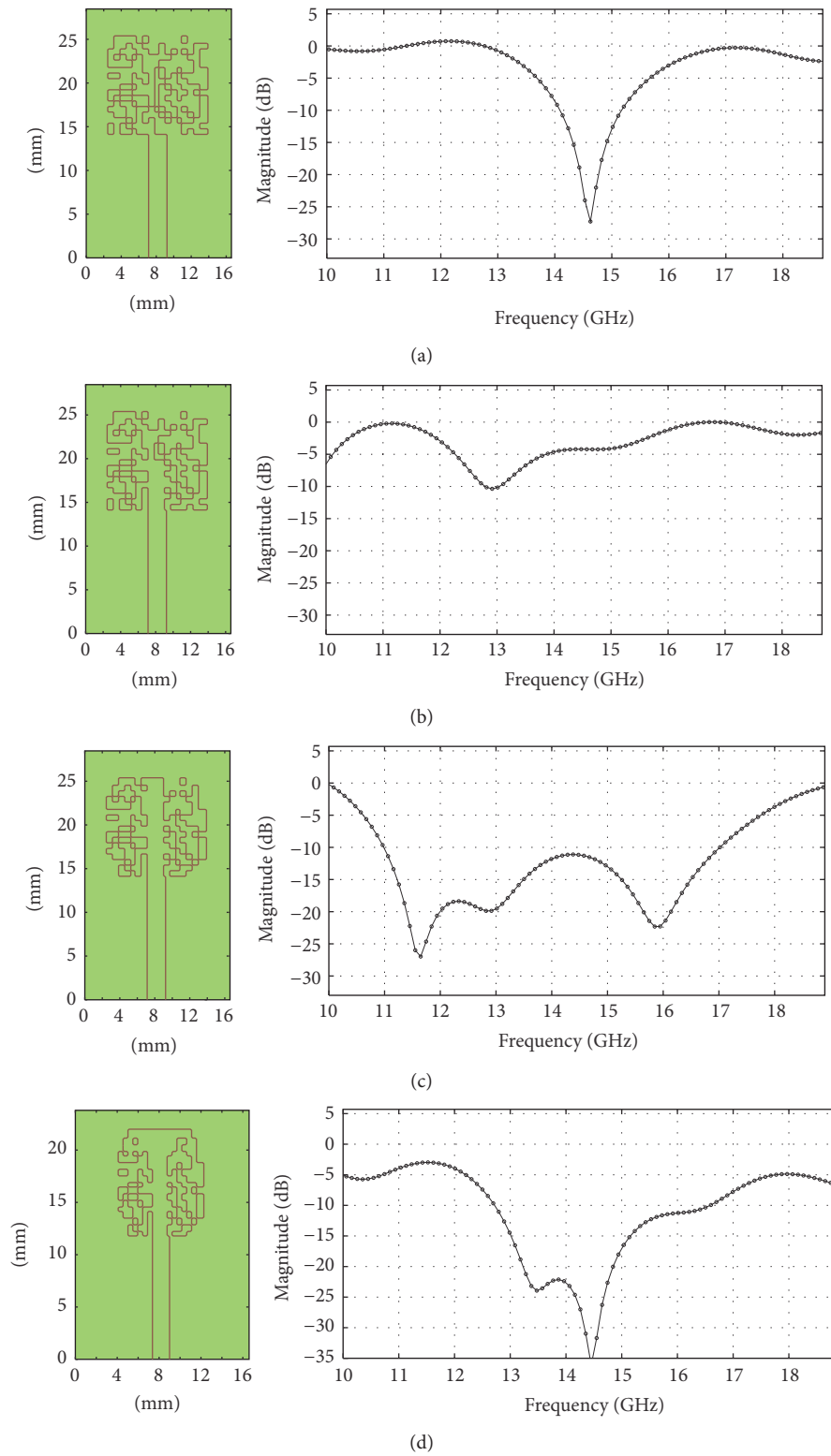


FIGURE 10: Some snapshots from the evolutionary optimization process.

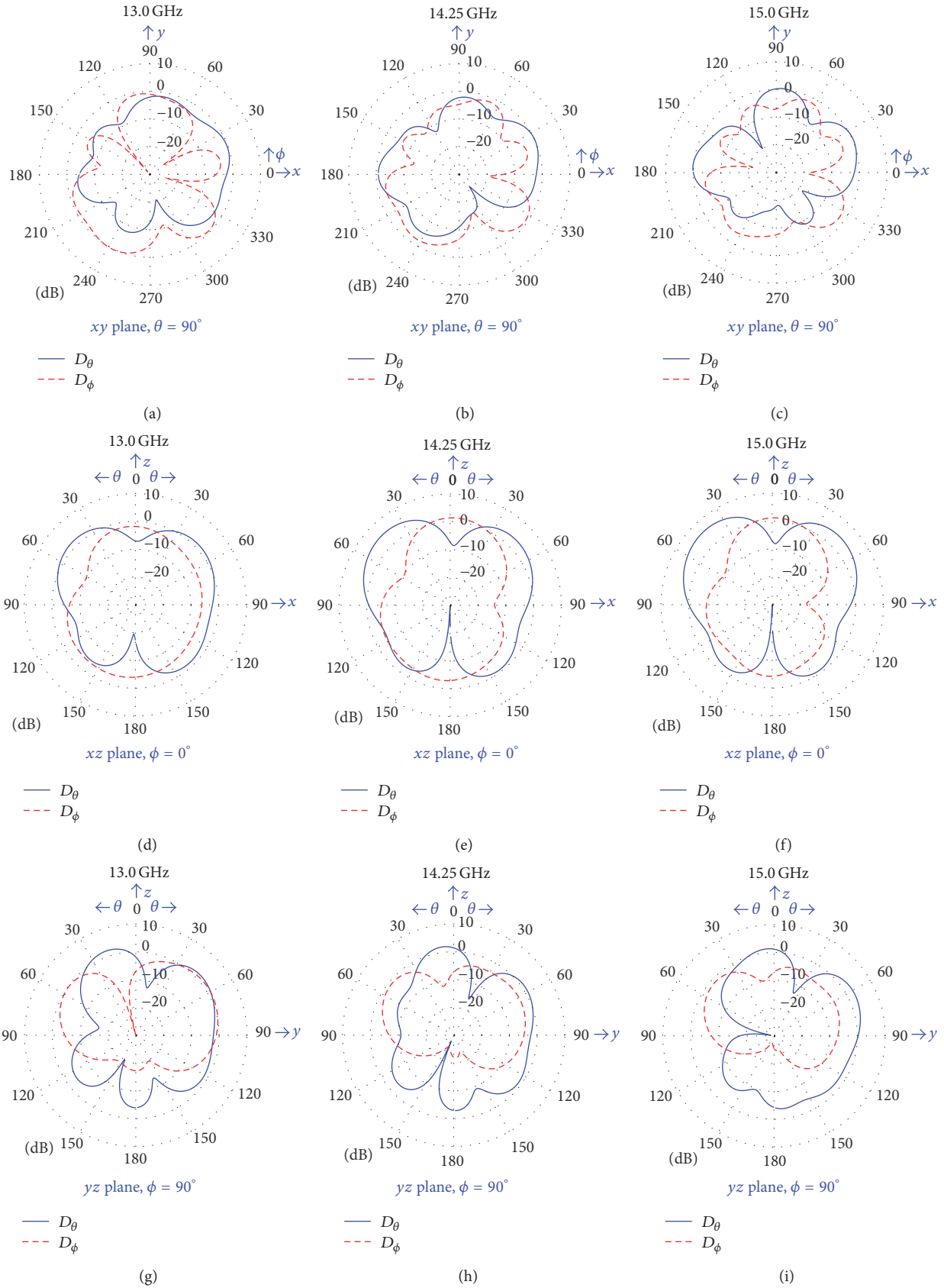


FIGURE 11: Radiation patterns of the antenna of Figure 10(d) for 13, 14.25, and 15 GHz.

to the design of other microstrip antennas. This is currently under investigation.

Conflicts of Interest

The authors declare that there are no conflicts of interest regarding the publication of this paper.

Acknowledgments

This work was supported by CAPES PNPD Scholarship 20131064.

References

- [1] S. R. Saunders, *Antennas and Propagation for Wireless Communication Systems*, John Wiley & Sons, 2003.
- [2] G. A. Deschamps and W. Sichak, "Microstrip microwave antennas," in *Proceedings of the 3rd Symposium on the USAF Antennas Research and Development Program*, pp. 18–22, October 1953.
- [3] I. J. Bahl and P. Bhartia, *Microstrip Antennas*, Artech House, Dedham, Mass, USA, 1980.
- [4] J. R. James and P. S. Hall, *Handbook of Microstrip Antennas*, Peter Peregrinus, London, UK, 1989.
- [5] D. M. Pozar and D. H. Schaubert, *Microstrip Antennas*, IEEE Press, New York, NY, USA, 1995.
- [6] J. F. Zurcher and F. E. Gardiol, *Broadband Patch Antennas*, Artech House, Boston, Mass, USA, 1995.
- [7] K. F. Lee and W. Chen, *Advances in Microstrip and Printed Antennas*, John Wiley & Sons, New York, NY, USA, 1997.
- [8] R. Garg, P. Bhartia, I. Bahl, and A. Ittipiboon, *Microstrip Antenna Design Handbook*, Artech House, Boston, Mass, USA, 2001.
- [9] R. B. Waterhouse, *Microstrip Patch Antennas: A Designer's Guide*, Springer, Berlin, Germany, 2003.
- [10] R. Bancroft, *Microstrip and Printed Antenna Design*, Noble Publishing, 2004.
- [11] K. Wong, *Compact and Broadband Microstrip Antennas*, John Wiley & Sons, New York, NY, USA, 2002.
- [12] G. Kumar and K. P. Ray, *Broadband Microstrip Antennas*, Artech House, Boston, Mass, USA, 2002.
- [13] Z. N. Chen and M. Y. W. Chia, *Broadband Planar Antennas: Design and Applications*, John Wiley & Sons, New York, NY, USA, 2006.
- [14] P. S. Hall and Y. Hao, *Antennas and Propagation for Body-Centric Wireless Communications*, Artech House, Boston, Mass, USA, 2006.
- [15] D. Guha and Y. M. M. Antar, *Microstrip and Printed Antennas New Trends, Techniques and Applications*, John Wiley & Sons, 2011.
- [16] S. Narayan, B. Sangeetha, and R. M. Jha, *Frequency Selective Surfaces Based High Performance Microstrip Antenna*, Springer, Singapore, 2016.
- [17] J. Michael Johnson and Y. Rahmat-Samii, "Genetic algorithms and method of moments (GA/MOM) for the design of integrated antennas," *IEEE Transactions on Antennas and Propagation*, vol. 47, no. 10, pp. 1606–1614, 1999.
- [18] H. Choo, A. Hutani, L. C. Trintinalia, and H. Ling, "Shape optimization of broadband microstrip antennas using genetic algorithm," *Electronics Letters*, vol. 36, no. 25, pp. 2057–2058, 2000.
- [19] C. A. Balanis, *Modern Antenna Handbook*, John Wiley & Sons, 2011.
- [20] L. A. Griffiths, C. Furse, and Y. C. Chung, "Broadband and multiband antenna design using the genetic algorithm to create amorphous shapes using ellipses," *IEEE Transactions on Antennas and Propagation*, vol. 54, no. 10, pp. 2776–2782, 2006.
- [21] J. Geng, R. Jin, X. Liang, H. Wu, Y. Sheng, and B. Zhou, "The study on the antenna optimization," in *Proceedings of the Progress in Electromagnetics Research Symposium (PIERS '10)*, pp. 22–26, Xi'an, China, February 2010.
- [22] A. Modiri and K. Kiasaleh, "Efficient design of microstrip antennas for SDR applications using modified PSO algorithm," *IEEE Transactions on Magnetics*, vol. 47, no. 5, pp. 1278–1281, 2011.
- [23] D. Minoli, *Innovations in Satellite Communications and Satellite Technology*, John Wiley & Sons, Hoboken, NJ, USA, 2015.
- [24] M. Kowalke, "New Air-to-Ground 4G LTE System Could Put Ultra-Broadband in the Skies," Next Generation Communications, July 2015, <http://next-generation-communications.tmcnet.com/topics/industries/articles/407374-new-air-to-ground-4g-lte-system-could.htm>.
- [25] L. Afonso, N. Souto, P. Sebastiao, M. Ribeiro, T. Tavares, and R. Marinheiro, "Cellular for the skies: exploiting mobile network infrastructure for low altitude air-to-ground communications," *IEEE Aerospace and Electronic Systems Magazine*, vol. 31, no. 8, pp. 4–11, 2016.
- [26] L. A. R. Ramirez, *Aplicação do Método das Diferenças Finitas no Domínio do Tempo na Análise de Cobertura em Ambientes Interiores [Ph.D. thesis]*, Pontifical Catholic University of Rio de Janeiro, 2008 (Portuguese).
- [27] S. D. Gedney, "An anisotropic perfectly matched layer-absorbing medium for the truncation of FDTD lattices," *IEEE Transactions on Antennas and Propagation*, vol. 44, no. 12, pp. 1630–1639, 1996.
- [28] W. Pedrycz, *Handbook of Computational Intelligence*, Springer, 2015.
- [29] C. A. Balanis, *Antenna Theory Analysis and Design*, John Wiley & Sons, 1997.
- [30] J. Kim, T. Yoon, J. Kim, and J. Choi, "Design of an ultra wide-band printed monopole antenna using FDTD and genetic algorithm," *IEEE Microwave and Wireless Components Letters*, vol. 15, no. 6, pp. 395–397, 2005.
- [31] S. Sun, L. V. Yinghua, and J. Zhang, "The application of genetic algorithm optimization in broadband microstrip antenna design," in *Proceedings of the IEEE 5th Asia-Pacific Conference on Environmental Electromagnetics*, pp. 192–195, September 2010.